Search for Electroweak Single Top Quark Production in 1.96 TeV Proton-Antiproton Collisions

by

Bernd Stelzer

A thesis submitted in conformity with the requirements
for the degree of Doctor of Philosophy
Graduate Department of Physics
University of Toronto

Abstract

Search for Electroweak Single Top Quark Production
in 1.96 TeV Proton-Antiproton Collisions

Bernd Stelzer
Doctor of Philosophy
Graduate Department of Physics
University of Toronto
2005

This thesis describes the first search for electroweak single top quark production in proton-antiproton collisions at a center of mass energy of 1.96 TeV. The data sample used for this analysis corresponds to 162 pb^{-1} recorded by the upgraded Collider Detector at Fermilab. The search is performed by doing a classic maximum likelihood fit to the H_T distribution in data. The kinematic variable H_T is the scalar sum of transverse energies of all final state particles in the event. This variable has the advantage that its distribution looks very similar for both contributing (s-channel and t-channel) single top processes, but is different for background processes. The combination of both channels to one signal improves the sensitivity of the search. No significant evidence for electroweak single top quark production is found and we set an upper limit at the 95% confidence level on the combined single top quark production cross section of 17.8 pb.

Acknowledgements

I would like to thank my supervisors Pierre Savard and William Trischuk for giving me the opportunity to work on this interesting topic at CDF for my Ph.D. thesis. I am especially thankfully to Pierre for giving me a lot of guidance and providing me with his extraordinary expertise throughout the program. I also would like to thank William for giving me the important insights into the functioning and understanding of the CDF detector and the silicon detector in particular. A special thank also to Pekka Sinervo for helping me resolving several statistical issues of the analysis. My gratitude also to my Ph.D committee members Bob Orr and Mike Luke.

I am extremely thankful to my immediate colleagues and friends in Toronto. My office mate, Stan Lai, who had always an open ear and good ideas towards many questions; my brother Oliver Stelzer-Chilton, who I could bug day and night; Shabnaz Pashapour, Jean-Francois Arguin, Ian Vollrath, Simon Sabik, Teresa Spreitzer, Dan McQueen and Kalen Martens, for many occasions of immediate support.

It is my pleasure to thank the people in the CDF single top group directly involved in this analysis: Florencia Canelli, Catalin Ciobanu, Tom Junk, Thomas Müller, Wolfgang Wagner and Thorsten Walter. I am very grateful for the team work we have established in the past and will continue in the future. I would also like to thank the entire CDF Collaboration - without its combined effort no analysis would be possible. In particular I would like to express my gratitude to the members of the CDF top and lepton + jets, as well as the electroweak working group.

I also thank the people who have inspired, supported and helped me towards this work in many different ways: Sharon Relova, Ashleigh Stelzer-Chilton, Erline Wong-Sing and my friends and family here and abroad.

I gratefully acknowledge the financial support of the Natural Science and Engineering Research Council of Canada and the University of Toronto.

Contents

List of Tables

List of Figures

Chapter 1

Introduction

Our present knowledge of the fundamental building blocks of matter and their interactions is summarised in the Standard Model of particle physics. The Standard Model distinguishes between fermions (quarks and leptons), which form observable matter, and bosons (photons, gluons, $W^{\pm}$, Z bosons), which are responsible for their interactions (forces). The Standard Model contains six quarks, where the sixth quark, the top quark, had escaped detection for quite a long time. As we know today, this was due to its large mass ($\simeq$ 175 GeV/c^2). The top quark was discovered in 1995 by the CDF and DØ Collaborations in its top-antitop quark pair production mode ($t\bar{t}$), mediated through the strong force [1, 2]. Data taking ended in 1996 for Run I of the Tevatron. CDF and the Tevatron have undergone major upgrades between 1996 and 2000 to increase the centre-of-mass energy from 1.8 to 1.96 TeV, and to increase the luminosity by about a factor of five. The upgraded Tevatron resumed operation in 2001, the beginning of Run II. Until data-taking starts at the LHC[1] in 2007, the Tevatron will be the only place to produce and analyze top quarks. The properties of the top quark have only been studied with small statistical samples, and are poorly constrained by Run I data. Precision measurements of top quark properties in Run II are therefore very important.

[1]Large Hadron Collider at CERN

The Standard Model of particle physics also predicts single top quarks to be produced at Fermilab's Tevatron Collider through the electroweak interaction. Due to formidable experimental challenges, single top production has so far eluded direct observation. The search for this process is one of the highest priorities of Run II because it offers some unique possibilities in studying the weak interactions of top quarks in both production and decay. The single top quark process is difficult to measure because the production rate has been calculated to be about two times smaller than that of top-antitop quark pair production, and especially because other background processes have much larger production rates than the signal.

This thesis presents the first search for single top quark production in 162 pb^{-1} of data from the Tevatron in Run II collected with the upgraded Collider Detector at Fermilab (CDF II). In this chapter, a short summary of the Standard Model is given together with a summary of the Standard Model top quark properties. Chapter 2 describes the electroweak production of single top quarks and the kinematics of its decay products. Chapter 3 provides an introduction to the Fermilab Tevatron accelerator facility and the upgraded CDF II detector. In Chapter 4 the event selection is described. Chapter 5 summarizes background processes which enter the data sample. In Chapter 6 the maximum likelihood method is described used in this analysis, and Chapter 7 provides the result from data. Chapter 8 provides an outlook and introduces a new analysis technique, which will be used in the next iteration of the single top search. Chapter 9 provides the conclusions.

1.1 The Standard Model of Particle Physics

The Standard Model is a theoretical framework that describes our current understanding of the physical world at the most fundamental level. To this day, it is a very successful theory and is consistent with all experimental observations [3]. Fundamental particles[2] and their interactions are quantitatively described by the use of Quantum Field Theory (QFT) [4].

Fundamental Particles and Interactions

The Standard Model describes the world in terms of interacting quantum fields. Different fields represent different particles and are grouped into two categories according to the value of their intrinsic angular momentum (spin) [5]. Particles with spin-1/2 are called fermions (quarks and leptons) and are the building blocks of observable matter. Atomic matter is composed of particles from the first generation (see Table 1.1). Within atoms, electrons are orbiting up and down quarks which make up nucleons inside atomic nuclei. Particles from the second or third generation are more massive duplicates of the particles from the first generation and only existed at an early stage of the universe. These particles are not stable and decay into particles from the first generation, but they can be produced and studied in high energy particle accelerators today. The u, d and s quarks are much lighter (all three < 160 MeV/c^2) than the c, b and t quarks ($\sim$ 1200, 4400 and 175000 MeV/c^2 respectively). This hierarchy is not understood. The down-type quarks (d, s, b) carry electric charge $-\frac{1}{3}e$ and the up-type quarks (u, c, t) carry electric charge $+\frac{2}{3}e$, where e is the charge of the electron.

Each lepton generation consists of a charged particle (electron, muon or tau) and an associated neutrino. The charged leptons carry electric charge $-1e$ while the neutrinos have zero electric charge. The three charged leptons also have increasing mass for higher

[2] A fundamental particle is one with no internal structure.

	Fundamental Fermions (Spin-1/2)					
	Quarks			**Leptons**		
Gen.	Flavor	Charge	Mass [MeV]	Flavor	Charge	Mass [MeV]
I	Up (u)	$+2/3$	1.5 to 4.5	Electron neutrino (ν_e)	0	$< 1.5 \times 10^{-6}$
	Down (d)	$-1/3$	5 to 8.5	Electron (e^-)	-1	0.511
II	Charm (c)	$+2/3$	1.0 to 1.4×10^3	Muon neutrino (ν_μ)	0	$< 1.9 \times 10^{-4}$
	Strange (s)	$-1/3$	80 to 155	Muon (μ^-)	-1	105.7
III	Top (t)	$+2/3$	170 to 179×10^3	Tau neutrino (ν_τ)	0	< 18.2
	Bottom (b)	$-1/3$	4.1 to 4.4×10^3	Tau (τ^-)	-1	< 1777.1

Table 1.1: Fundamental fermions (quarks and leptons) of the Standard Model [6].

generations. Recent results provide evidence that neutrinos have masses that are small but non-zero in absolute value [7]. Neutrinos interact only through the weak force while the charged leptons interact in addition through the electromagnetic force.

Particles with integral spin are called bosons and are quanta of the quantum fields responsible for interactions between particles. The Standard Model describes three types of interactions among quarks and leptons: the electromagnetic, the weak, and the strong force. Table 1.2 summarizes all fundamental interactions and their associated boson. Gravity is currently not described by the Standard Model, but since it dominates only for large masses and has little effect on the scale of quarks and leptons, it can usually be ignored in fundamental particle interactions. The most basic interaction between two particles can be represented as a process in which two particles exchange a boson. The Lagrangian of each interaction obeys gauge invariance under a transformation that corresponds to a symmetry group. The Standard Model is based on the symmetry group $SU(3) \times SU(2) \times U(1)$ [8].

Quantum Electrodynamics is based on the $U(1)$ symmetry group and describes the electromagnetic interaction among quarks and leptons through the exchange of massless

Fundamental Bosons (Spin-1)				
Interaction	Name	Gauge Group	Charge	Mass [GeV/c^2]
Electromagnetic	Photon (γ)	U(1)	0	0
Weak	W boson (W)	SU(2)	1	80.4
Weak	Z boson (Z)	SU(2)	0	91.2
Strong	Gluon (g)	SU(3)	0	0

Table 1.2: Fundamental bosons of the Standard Model.

spin-1 photons [9].

The weak interaction is mediated by the W and Z bosons. Since these particles are very massive, they can only act over small distances. One of the greatest achievements in the development of the Standard Model was the unification of the electromagnetic and weak interaction which was combined to the electroweak theory [10]. This unification was achieved by introducing a scalar field, known as the Higgs field, whose presence breaks the symmetry of the SU(2)×U(1) gauge group. The electroweak unification explains the existence of the W and Z bosons and the photon and the process of symmetry breaking allows the W and Z to acquire mass [11]. The predictions made on the basis of the electroweak theory have been verified by experiments with very high precision [12].

The weak interaction allows transitions between quarks of different flavors; transitions within the same generation are favored over those across generations. The mass eigenstates of the down-type quarks (d', s', b') do not match the eigenstates of the weak interaction (d, s, b). This phenomenon is known as the the Cabibbo-Kobayshi-Maskawa (CKM) mixing and the 3×3 CKM unitary matrix, shown in Equation 1.1, links the mass-eigenstates with the eigenstates of the weak interaction. The matrix elements, $|V_{ij}|$, characterize the strength of the transition of quarks into other flavor quarks ($|V_{ij}| \leq 1$)

when interacting through the charged weak interaction (exchange of a $W^{\pm}$ boson).

$$\begin{pmatrix} d' \\ s' \\ b' \end{pmatrix} = \begin{pmatrix} V_{ud} & V_{us} & V_{ub} \\ V_{cd} & V_{cs} & V_{cb} \\ V_{td} & V_{ts} & V_{tb} \end{pmatrix} \begin{pmatrix} d \\ s \\ b \end{pmatrix} \tag{1.1}$$

The parameters of the matrix can be found in Reference [6].

Quantum Chromodynamics is based on the $SU(3)$ symmetry group and describes the strong interaction among quarks, mediated by the exchange of eight massless spin-1 gluons [13]. Quarks and gluons carry color charges (R, G, B) which are analogous to the electric charge in Quantum Electrodynamics. The eight gluons represent the following color combinations:

$$R\bar{B},\ R\bar{G},\ B\bar{R},\ B\bar{G},\ G\bar{R},\ G\bar{B},\ (R\bar{R}-G\bar{G})/\sqrt{2},\ (R\bar{R}+G\bar{G}-2B\bar{B})/\sqrt{6}$$

Quarks are bound together through the strong interaction to form colorless states. The $q\bar{q}$ bound states are called mesons (e.g. pion) and qqq bound state are called baryons (e.g. proton). The residual color field outside the nucleons (protons and neutrons) then forms nuclei (just like the residual electric field outside neutral atoms forms molecules). Big differences between QCD and QED arise due to the fact that gluons carry color charge, while the photon is electrically neutral. This gives rise to an effect called self-coupling of gluons. At short distances (or large momentum transfers) the strong force gets weaker. This property is known as asymptotic freedom [14]. At large distances, however, the strong force has the property that the potential energy of two colored particles increases with distance between them. This property is called confinement and implies that colored particles (quarks and gluons) appear as jets in high energy particle collisions where a lot of energy is transferred to a quark inside the proton. The quark moves off relative to the other quarks with which it was bound and the color field grows until enough energy is present to create a particle-antiparticle pair out of the vacuum. This process repeats until the original energy is dissipated, producing several hadrons (a process referred to as

hadronization). In effect, instead of observing a single quark or gluon, we detect color-neutral combinations of quarks and gluons that form physical hadrons which move in the same direction as the original particle (i.e. a jet) [8]. An exception is the heavy top quark, which decays before it can hadronize [15].

1.2 The Top Quark

Within the Standard Model framework, the top quark is the SU(2) partner of the bottom quark in the third generation of fundamental fermions. Because the top quark was found to be so much more massive than all other fermions, it has been speculated that it may play a special role in nature [16].

1.2.1 Top Quark Properties

The top quark was first observed in Run I of the Tevatron and most of its properties are still inferred indirectly. If the top quark indeed plays a special role in nature, it is likely that some of these inferred properties will in fact differ from their direct measurements. Thus it is important to study the top quark properties in a direct way through all possible production and decay channels.

Production

In proton-antiproton ($p\bar{p}$) collisions, the four-momentum of the p and $\bar{p}$ is divided among the quarks and gluons inside the proton, collectively called partons. In inelastic collisions with high momentum transfer, an individual parton inside the proton/antiproton undergoes the interaction which breaks the initial proton and antiproton. The energy available in the collision to produce new particles, like the top quark, is only a fraction of the total center-of-mass energy of the $p\bar{p}$ system. If P_1 is the four-momentum of the proton and P_2 is the four momentum of the antiproton and x_1 and x_2 are the fractions

of momentum carried by the partons which undergo the interaction then:

$$s = (x_1 P_1 + x_2 P_2)^2 \simeq 2 x_1 x_2 P_1 P_2 \simeq x_1 x_2 (P_1 + P_2)^2 = x_1 x_2 \hat{s}$$

where $\hat{s}$ is the square of the invariant mass of the proton-antiproton system and s is the square of the invariant mass of the parton system, which is a fraction $x_1 x_2$ smaller. The mass of the proton/antiproton is considered to be negligible in this calculation.

The fraction of momentum (x) carried by the individual partons inside the proton is characterized by the parton distribution functions (PDFs). The probability of finding a certain parton with momentum fraction between x and $x + dx$ is $f(x)dx$. Figure 1.1 shows the PDFs for u, d, s and b-quarks. The PDFs have been measured in deep inelastic

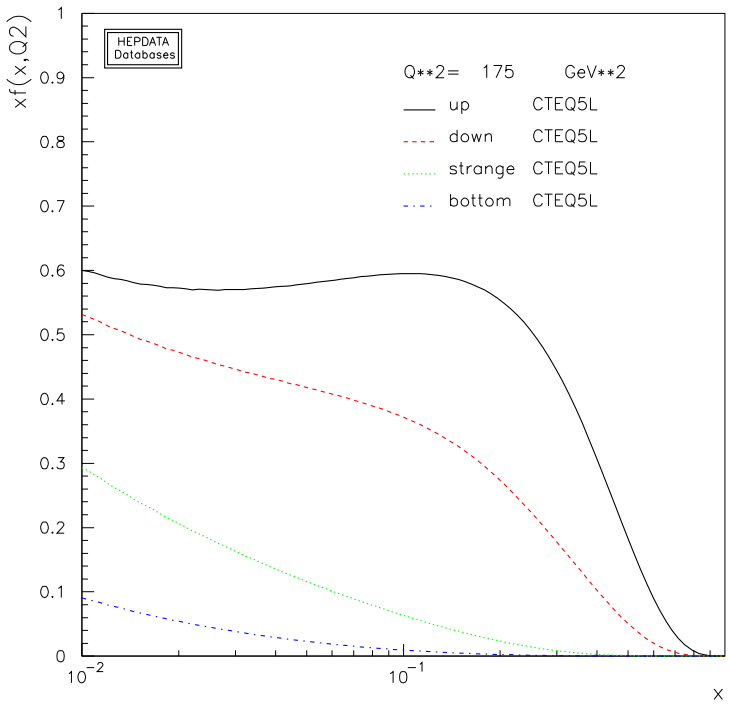

Figure 1.1: Parton distribution functions (CTEQ5L) for u, d, s and b-quarks inside the proton [17].

electron-proton scattering mainly by the H1 and ZEUS Collaborations at DESY[3]. Two sets of PDFs are currently available, prepared by the CTEQ [18] and MRS [19] analysis

[3]Deutsches Elektronen-Synchrotron

groups.

At the Tevatron, top quarks may be produced in $t\bar{t}$ pairs through the strong force, or singly through the electroweak force. The top pair production mode is the dominant channel and proceeds mostly through a quark-antiquark annihilation process, $q\bar{q} \rightarrow t\bar{t}$ and to a lesser extent ($\approx$13%) through gluon-gluon fusion, $gg \rightarrow t\bar{t}$. Single top quarks are produced through the exchange of a virtual W boson of the colliding partons. Two channels contribute at the Tevatron, the s-channel process, $q\bar{q'} \rightarrow t\bar{b}$ and the t-channel process $qb \rightarrow tq'$.

Mass

The mass of the top quark has been measured by the CDF and DØ Collaborations at the Tevatron during Run I. All Run II analyses are still preliminary and not published. The 2004 particle data group best value of the top mass is: 174.3 $\pm$ 3.2 $\pm$ 4.0 GeV [6].

Lifetime

The width of the top quark is predicted by the Standard Model to be:

$$\Gamma(t \rightarrow Wb) = \frac{G_F m_t^3 |V_{tb}|^2}{8\pi\sqrt{2}}(1 - \frac{m_W^2}{m_t^2})^2(1 + 2\frac{m_W^2}{m_t^2})[1 - \frac{2\alpha_s(4\pi^2 - 15)}{18\pi}]$$

where G_F is the Fermi coupling constant, V_{tb} is the CKM matrix element, m_t is the top quark mass, m_W is the mass of the W boson and α_s is the coupling constant of the strong interaction. Since the top mass is very large, the width is large, too. At a top mass of 175 GeV/c^2 it has a value of $\Gamma_t \simeq 1.53$ GeV. This corresponds to a lifetime of $\tau = \hbar/\Gamma_t$ of 0.4 $\times 10^{-24}$ s. The shortness of this lifetime has a profound implication. A top quark decays before the strong force can bind it into a hadron. In QCD, the formation of bound states takes a certain time, the inverse of Λ_{QCD}, about 10^{-23} s. The top quark decays within about 10^{-24} s after its formation, so that bound states cannot be formed. It's important to point out that the top quark does interact with gluons, but these interactions, at time scales less than 10^{-24} s, are so weak that the top quark basically exists as a free quark.

Decay

The top quark decays through the electroweak interaction. While the decay width of the top quark is large by standards of other quarks, it is still quite small compared to experimental resolution. Thus it is very difficult to measure the width directly. Assuming

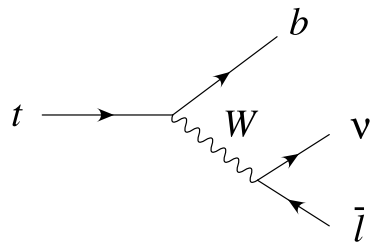

Figure 1.2: Top quark decay with leptonic W boson decay.

only three generations of quarks, the CKM matrix element V_{tb} can be inferred from the unitarity of the CKM matrix to be close to unity ($|V_{tb}| = 0.9991$ to 0.9994). As a result, the Standard Model predicts that the top quark decays almost always to a b quark and a W boson with a branching ratio (BR) close to 1. Top decays are therefore labeled by the W boson decay mode. The W boson can either decay into a lepton and its associated neutrino (BR=1/9), or into a quark-antiquark pair (BR=3/9). The branching ratio is larger for the decay into quarks because of three possible color combinations.

Polarization

The left-handed nature of the SM weak interaction determines the polarization of the W boson in top decays. This, together with the fact that the top quark decays before it can hadronize makes it possible to reconstruct the polarization of the top in the laboratory. In $t\bar{t}$ events, the spins of the two top quarks are correlated and the multi particle final state causes ambiguities which make it hard to reconstruct the top quark rest frame. Single top quark production however offers an optimal spin basis to measure the top polarization since it proceeds through the electroweak interaction in the production and the decay [20]. The spin basis exploits the fact that the W boson couples only to fermions

with left-handed chirality which leads to a 100% polarization of the produced top quark in the direction of the d-type quark. A small ambiguity arises from identifying the d-type quark. For single top production through the s-channel, 98% of the top quarks have their spins in the antiproton direction. For single top production through the t-channel, 96% of the top quarks have their spins in the direction of the light flavor quark, recoiling against the virtual W boson. The polarization of the top quark is then reflected in the angular correlation of its decay products and is best visible in the top rest-frame (see Figure 2.4 and Figure 2.5) by plotting the cosine of the azimuthal angle between the direction of the final state lepton (from the W decay) and the direction of the d-type quark (which is most likely the beam axis in case of s-channel and the light flavor quark in the final state in case of t-channel single top).

Chapter 2

Electroweak Single Top Quark Production

The Standard Model of particle physics predicts top quark production through the electroweak interaction [21, 22]. This process is referred to as 'single top', since the top quark is produced singly, either in association with a b-quark (s-channel), in association with a light flavor quark (t-channel) or in association with a W boson (associated production). Feynman diagrams of the production channels are shown in Figure 2.1. The cross sec-

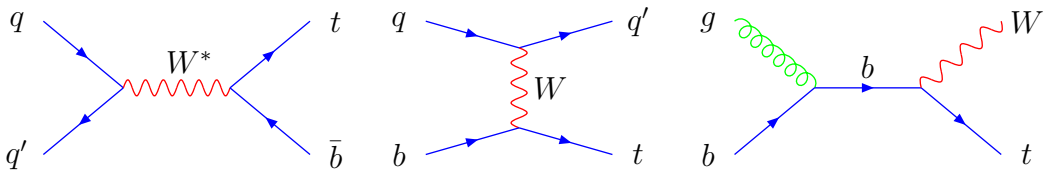

Figure 2.1: Leading order Feynman diagrams for s-channel (left), t-channel (middle) and associated tW (right) single top quark production.

tion of the associated production is kinematically suppressed at the Tevatron ($\sigma_{tW} < 0.1$ pb) due to the initial state b quark and the heavy top quark and W boson in the final state. Only the s-channel and t-channel production modes are therefore considered in this analysis.

Electroweak single top quark production offers some unique possibilities. The measurement of the production cross section is proportional to the Cabibbo-Kobayashi-Maskawa matrix element $|V_{tb}|^2$ and allows therefore the direct extraction of this quantity. $|V_{tb}|$ characterizes the strength of transition of a top quark into a bottom quark when the two particles interact through the (charged) electroweak interaction. The quantity is currently not well measured and all previous results were made under the assumption that the CKM matrix is unitary [23]. Three generations of quarks are described in the Standard Model and the unitarity of the CKM matrix implies that $|V_{ub}|^2 + |V_{cb}|^2 + |V_{tb}|^2 = 1$. The elements $|V_{ub}|$ and $|V_{cb}|$ have been measured to be small and one finds [24]:

$$|V_{tb}| = 0.9991 \text{ to } 0.9994 \text{ (three generations of quarks)}$$

If we assume more than three generations of quarks, then the unitarity of the CKM matrix implies almost nothing about $|V_{tb}|$ [24]:.

$$|V_{tb}| = 0.06 \text{ to } 0.9994 \text{ (} > \text{ three generations of quarks)}$$

Measuring the single top quark production cross section allows us to avoid the assumption of unitarity, to measure $|V_{tb}|$ precisely, and to draw conclusions about a hypothetical fourth generation of quarks. Moreover, electroweak single top quark production provides an extraordinary source of polarized top quarks with a very large net polarization ($\geq 96\%$) [20]. Studying the polarization in single top events will be a very important test of the weak interaction of the top quark. Finally, measuring the single top process tests exotic models beyond the Standard Model, which predict anomalously altered single top production rates like heavy right handed W' bosons, flavor changing neutral currents or large extra dimensions [25]. Two searches for single top quark production have been performed during Run I of the Tevatron at a center of mass energy of 1.8 TeV. The CDF Collaboration reported upper limits on the single top quark production cross section at the 95 % Confidence Level of 13 pb for the t-channel process, 18 pb for the s-channel process and 14 pb for the combined (s-channel + t-channel) search [26]. The limits

obtained by the DØ Collaborations were 22 pb for the t-channel process and 17 pb for the s-channel process [27].

2.1 Theoretical predictions

2.1.1 The Leading-Order Matrix Element

The leading order Feynman diagrams for s-channel and t-channel single top quark production are shown in Figure 2.1. For each channel, the Born differential cross section can be written as:

$$d\sigma = \frac{1}{2s}|M|^2 d\Phi_2, \quad d\Phi_2 = \frac{(|p_{CM}|d(cos\theta))}{8\pi\sqrt{s}}, \quad |p_{CM}| = \frac{s-m_t^2}{2\sqrt{s}}$$

Where s is the partonic center-of-momentum energy squared and $d\Phi_2$ is the two body phase space. Using the Feynman rules [4], the matrix element for the s-channel is given by:

$$iM = (\bar{v_{\bar{d}}}(-i\frac{g}{\sqrt{2}}\gamma^\mu\frac{1}{2}(1-\gamma_5)V_{ud})u_u)(\frac{-ig_{\mu\nu}}{s-m_W^2})(\bar{u_t}(-i\frac{g}{\sqrt{2}}\gamma^\nu\frac{1}{2}(1-\gamma_5)V_{tb})\bar{v_b})$$

where v and u are the Dirac spinors for the quark fields, γ^μ and γ_5 are the Dirac matrices, $g_{\mu\nu}$ is the metric tensor, $s = (p_u + p_{\bar{d}})^2$, m_W is the mass of the W boson and g is the weak coupling constant.

Since the intrinsic spin of particles is not measured at CDF directly, we can take the sum over initial state spin directions and sum over final state spin direction. The square of the matrix element becomes then:

$$|M|^2 = g^4\frac{|V_{ud}|^2|V_{tb}|^2}{(s-m_W^2)^2}(p_u \cdot p_{\bar{b}})(p_{\bar{d}} \cdot p_t)$$

A similar expression is obtained for the t-channel.

2.1.2 Next-to-Leading-Order Corrections

At next-to-leading order perturbation theory (NLO), virtual QCD corrections and real emission of partons are included in the calculation [4].

s-channel

For the s-channel some NLO virtual and real emission Feynman diagrams are shown in Figure 2.2. The energy scale of the process is characterized by the top mass ($\simeq 175$ GeV)

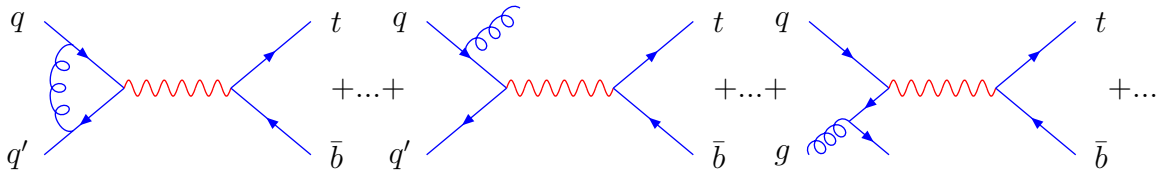

Figure 2.2: Some representative Feynman diagrams of the virtual and real emission NLO corrections to s-channel single top quark production.

and is far away from the scale at which QCD becomes non-perturbative ($\Lambda_{QCD} \approx 250$ MeV). The calculation is therefore in a regime where QCD is very reliable. The process is similar to the Drell-Yan type process $q\bar{q}' \rightarrow l\nu$ which has been very well studied. The initial state QCD corrections for the s-channel single top process are identical to that for Drell-Yan. This leaves only the final-state QCD corrections to be done, which are relatively straightforward since the initial and final-state corrections do not interfere at NLO for electroweak single top production [21]. Furthermore, Drell-Yan data can be used to reduce systematic uncertainties on PDF's and QCD corrections to the initial state. A fully differential NLO cross section calculation has been performed recently [28]. The prediction for the cross section and uncertainties for the s-channel have been updated and found to be:

$$\sigma_s = 0.88 \pm 0.05\ pb$$

t-channel

For the t-channel some representative NLO diagrams are shown in Figure 2.3. The energy scale of the process is characterized by the virtuality of the W boson in case of the light flavor quark line and is characterized by the virtuality of W boson plus the mass of the top quark in the case of the top quark line. The prediction for the inclusive cross section

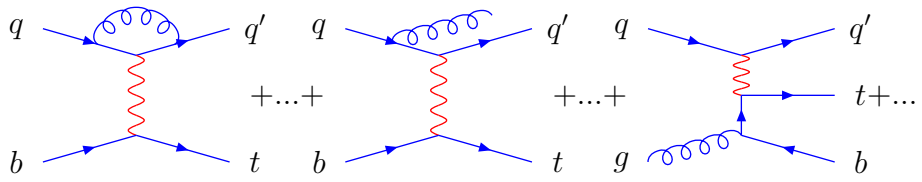

Figure 2.3: Some representative Feynman diagrams of virtual and real emission NLO corrections to t-channel single top quark production.

at NLO has been calculated using a phase space slicing method and found to be [28]:

$$\sigma_t = 1.98 \pm 0.08\ pb$$

For both channels the main sources of systematic uncertainties arise from the top quark mass uncertainty and PDF uncertainties. The result for the leading order calculation only are σ_s^{LO} =0.57 pb and σ_t^{LO} =1.99 pb for the s-channel and t-channel respectively.

2.2 Single Top Event Kinematics

To simulate the kinematic distributions of the final state particles in single top events, the MadEvent Monte Carlo program has been used [29]. MadEvent is a leading-order matrix element event generator. This program has the advantage that it includes both production and decay of the top quark and passes the correct spin information to the decay products. MadEvent can decay the W boson from the top decay into all possible final states. However, we choose to select only the leptonic decay of the W boson ($W \rightarrow l\nu_l$). This choice is motivated in Chapter 4. Figure 2.4 shows the kinematic distributions

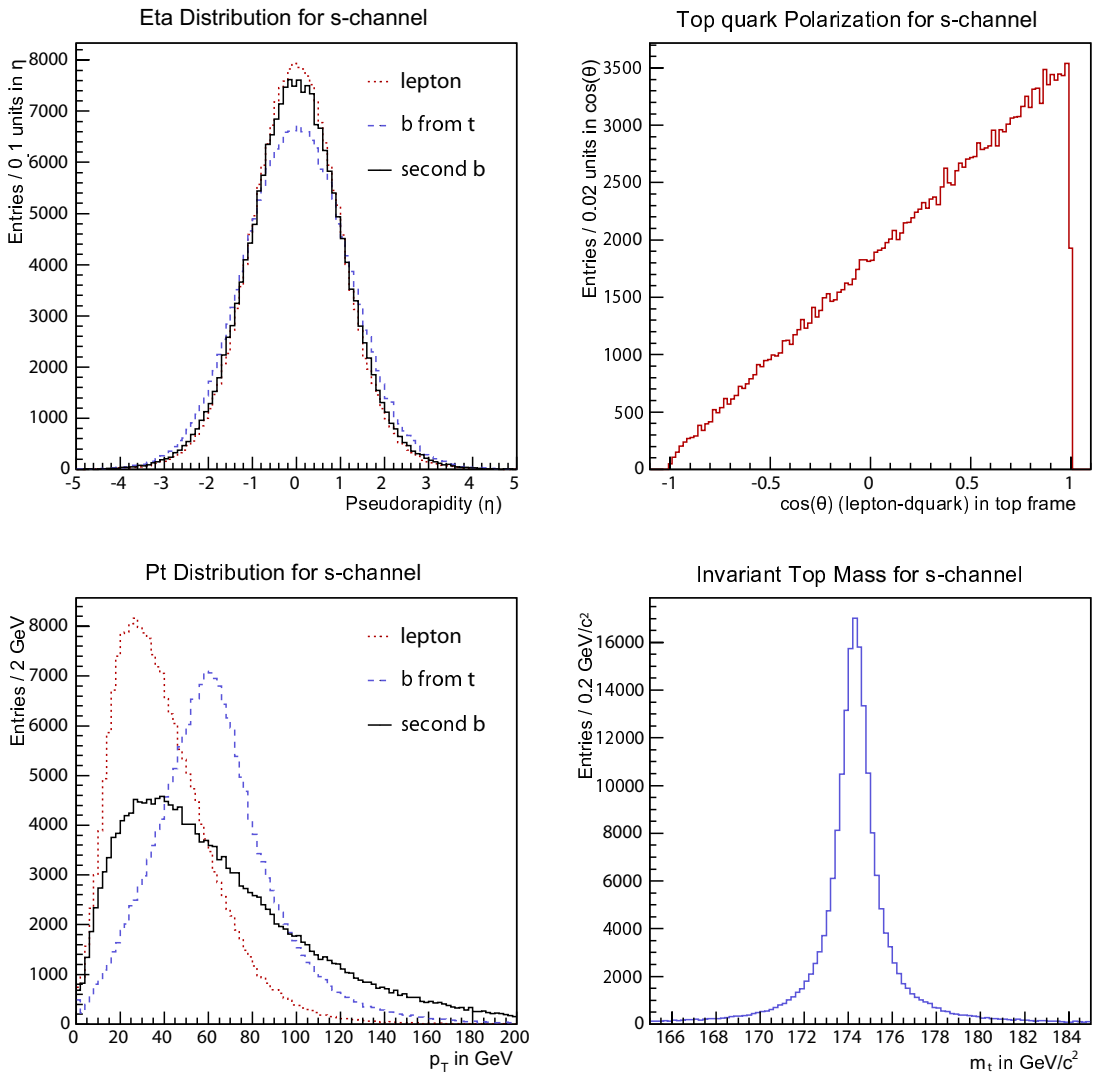

Figure 2.4: Kinematic distributions of final state particles for s-channel single top quark production.

of the observable final state particles of s-channel single top. The Pythia program is used to include the presence of higher order QCD and QED effects [30]. This is done in the so-called shower approximation. Figure 2.5 shows the kinematic distributions for the t-channel final state particles. For the t-channel process we employed a merging of events generated with the LO matrix element and events generated with the NLO matrix elements (diagram where the initial state gluon splits into two b quarks) [31]. The reason for that is that the shower approximation employed by Pythia works very

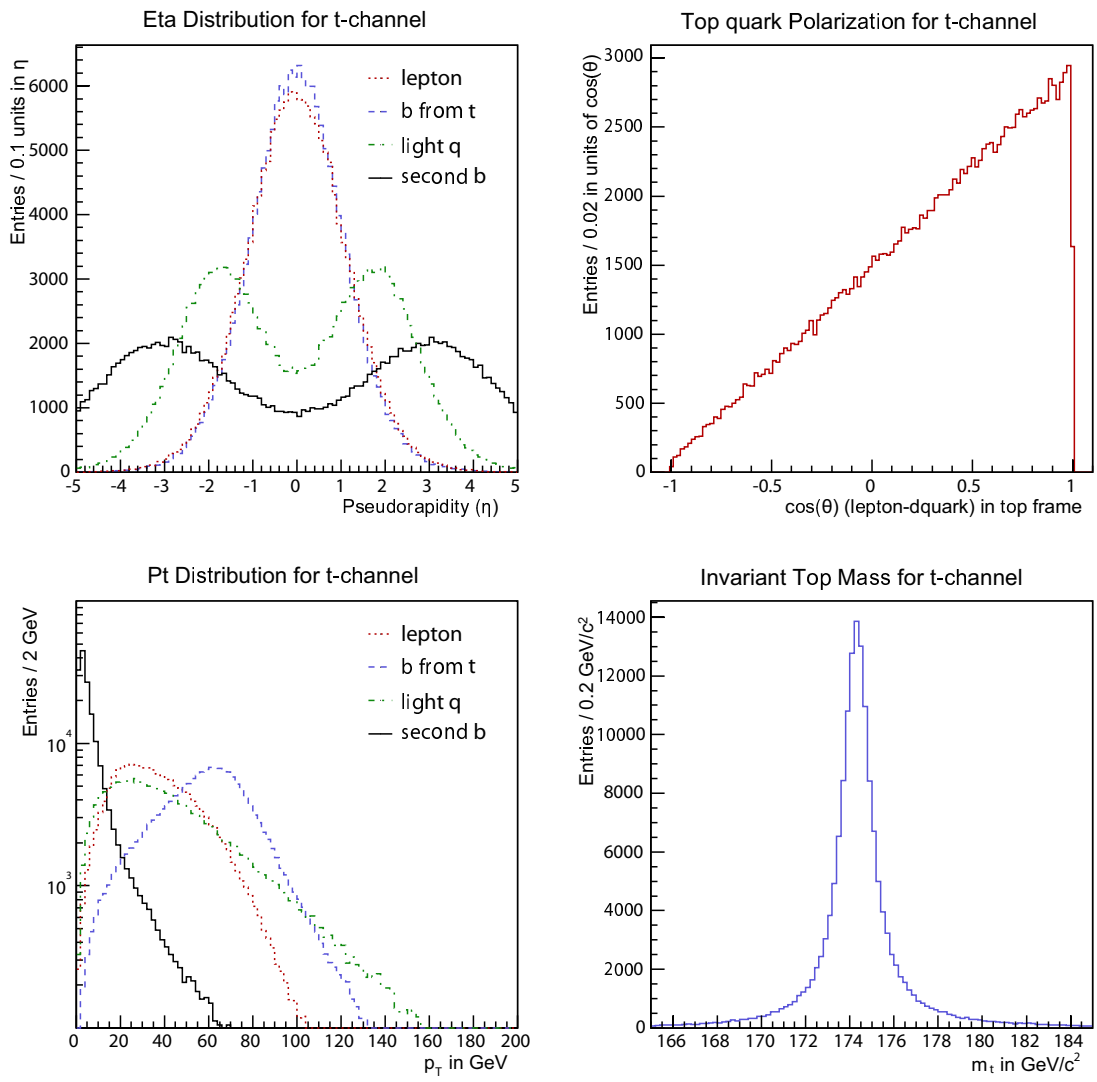

Figure 2.5: Kinematic distributions of final state particles for t-channel single top quark production.

well for processes which are dominated by initial and final state radiation like the s-channel. The problem in the t-channel comes from the b-quark in the initial state. Since b-quarks exist only as 'sea quarks' in the proton, programs like Pythia calculate an initial state through backward evolution where the b-quark originates from gluon splitting while the b-quark momentum was estimated using the proton PDF. The collinear singularity problem is naturally taken care of in this case, but this approach misses the cases where the initial state contains a hard gluon (W-gluon fusion type diagrams). The hard gluon

also splits into two b-quarks but gives the b-quarks higher momentum. In this case the process is of the type $gq \rightarrow tbq'$. To cover the full spectrum, we generate both event scenarios and merge the samples to obtain a smooth transverse momentum spectrum of the b-quark (which originates from the gluon splitting). This approach is outlined in Reference [32].

The final state particles for the s-channel process consist of the W decay products and two energetic b quarks which are emitted over a similar range in pseudo-rapidity. One b-quark comes from the top decay while the second one is emitted from the primary tWb vertex and recoils against the top quark. For t-channel events, the second b-quark originates from the initial-state gluon splitting and tends to reside at small transverse momentum (p_T) and is emitted at higher pseudo-rapidities. In addition, a third (light flavor) quark is produced. This quark is recoiling from the virtual W-emission and has a distinct peak at higher pseudo-rapidities. The final states of both single-top channels feature a similar high-p_T and low-$|\eta|$ b quark in the final state together with the decay products of a real W. The kinematic properties of the second b quark in the event, however, differ significantly between the two processes. In addition, the final state of the t-channel process is accompanied by a light flavor quark.

In both channels, the polarization of the top quark is clearly visible in the angular correlation of its decay products. The cosine azimuthal angle between the final state lepton (from the W decay) and the initial state d-type quark forms a monotonically (linear) rising distribution, following $\sim [1 + cos(\theta)]$. In case of the s-channel, the d-type quark is the proton-beam axis, while in the t-channel the d-type quark is the direction of the light flavor quark [20].

Chapter 3

The Experimental Apparatus

Due to their large mass, top quarks can only be produced at today's most energetic particle accelerator, the Tevatron at Fermilab[1].

3.1 The Tevatron

The Tevatron has undergone major upgrades between 1996 and 2000 to increase the centre of mass energy from 1.80 to 1.96 TeV and to increase the luminosity by a factor of $\simeq 5$ [33]. The increased luminosities have been achieved by adding a new ring, the Main Injector, which greatly increases the rate of antiproton production and hence the number of antiprotons available for collisions. The increase in proton-antiproton ($p\bar{p}$) centre of mass energy was obtained by operating the superconducting magnets of the Tevatron at a colder temperature. In order to keep the number of interactions per bunch crossing low, while raising the instantaneous luminosity, it was also necessary to increase the number of proton and antiproton bunches simultaneously in the ring from 6 to 36 bunches which reduces the time between bunch crossings to 396 ns. The upgraded Tevatron resumed operation in 2001, the beginning of Run II. The most important accelerator parameters

[1] and starting from 2007, at the Large Hadron Collider at CERN

are summarized in Table 3.1.

Accelerator Parameter	Run I	Run II
$p \times \bar{p}$ bunches	6×6	36×36
Number of p per bunch	2.3×10^{11}	2.6×10^{11}
Number of $\bar{p}$ per bunch	5.5×10^{10}	3.5×10^{10}
Beam energy [GeV]	900	980
Luminosity [$\mathrm{cm}^{-2}\mathrm{s}^{-1}$]	1.6×10^{31}	8×10^{31}
Bunch crossing time [ns]	3564	396
Number of interactions per crossing	2.5	2.3

Table 3.1: Accelerator parameters of the Tevatron.

The acceleration of protons and antiprotons to a final energy of 980 GeV per beam is performed in several steps. A schematic diagram of the Tevatron accelerator complex is shown in Figure 3.1 and a brief explanation of each step is provided below.

Cockroft-Walton

The Cockcroft-Walton pre-accelerator provides the first stage of acceleration. H^- ions are produced in a magnetron surface plasma source, located inside the Cockroft-Walton, and accelerated inside an electrostatic field to an energy of 750 keV.

Linac

The Linac is a 150 m long linear accelerator that uses RF cavities to accelerate the H^- ions, coming from the Cockroft-Walton, to a final energy of 400 MeV. At the end of this step, the ions are passed through a carbon foil, which serves the purpose of stripping off the electrons from the ions, leaving bare protons.

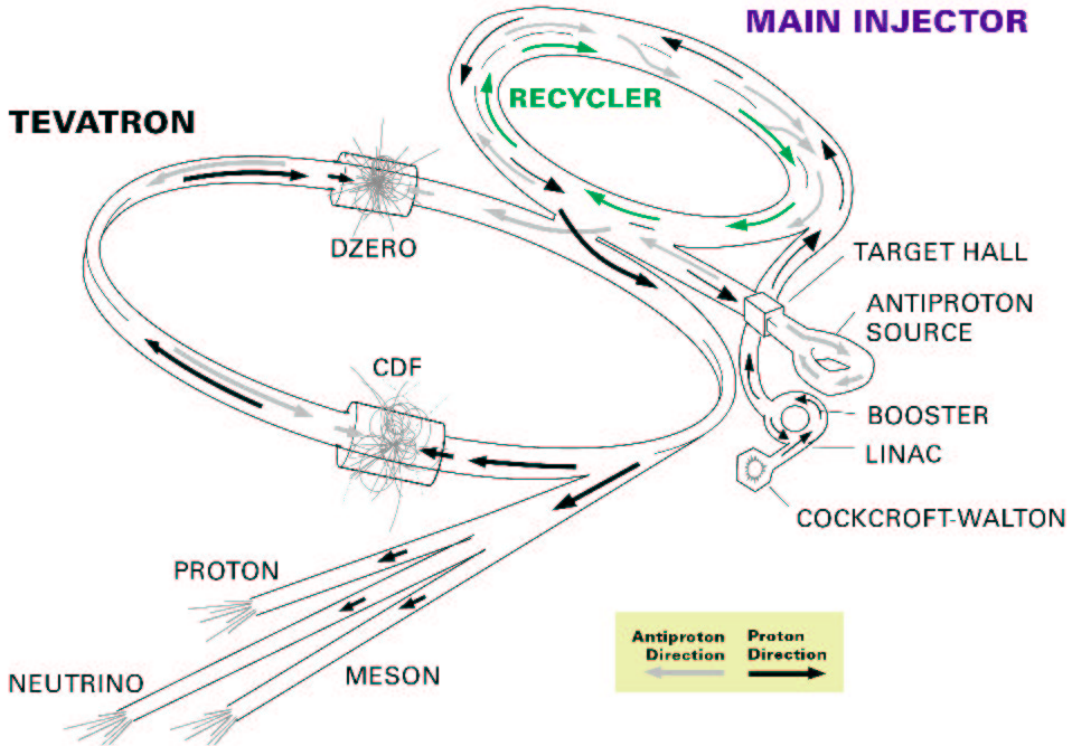

Figure 3.1: Schematic drawing of the Tevatron accelerator chain.

Booster Ring

The protons are passed to the booster ring which is a standard synchrotron accelerator. Here, the protons reach an energy of 8 GeV.

Main Injector

The Main Injector, which is also a synchrotron, accepts the protons from the booster and continues the acceleration process up to an energy of 150 GeV. A fraction of these protons are aimed at a nickel target inside the target hall to produce antiprotons.

Tevatron

The 150 GeV protons from the Main Injector are delivered to the Tevatron ring. The Tevatron is a superconducting synchrotron and accelerates the protons to their final

energy of 980 GeV.

Accumulator

The antiprotons produced in the target hall have a large momentum spread that leads to a large emittance of the antiproton beam. To reduce the emittance, antiprotons undergo a process called 'stochastic cooling' [34]. This effectively reduces their momentum spread and is performed inside the Accumulator (not shown in Figure 3.1). When the emittance and intensity of the antiprotons meet certain quality requirements, they are sent back to the Main Injector, for acceleration and injection into the Tevatron.

Collision Points

The Tevatron has two dedicated collision points in the accelerator ring. One is used by the CDF experiment and the other is used by the DØ experiment. At the collision points, the Tevatron contains special focusing magnets to reduce the beam size to less than 30 μm. A typical colliding beam, called a 'store', lasts for about 15 hours. Because the yield of producing antiprotons in the target hall is rather low, protons are always kept in the Main Injector to produce antiprotons, even though collisions are taking place in the Tevatron. The produced antiprotons are continuously transfered to the Accumulator for use in the next store. At the end of each store, the beams are aborted with a special beam dump and the Tevatron is filled with new protons as well as the accumulated antiprotons to start a new store.

3.2 The CDF Detector

The data used for the measurement reported in this thesis were collected with the upgraded Collider Detector at Fermilab (CDF II) [35]. Detector upgrades were made to accommodate the higher luminosities and new beam conditions resulting from the upgrades

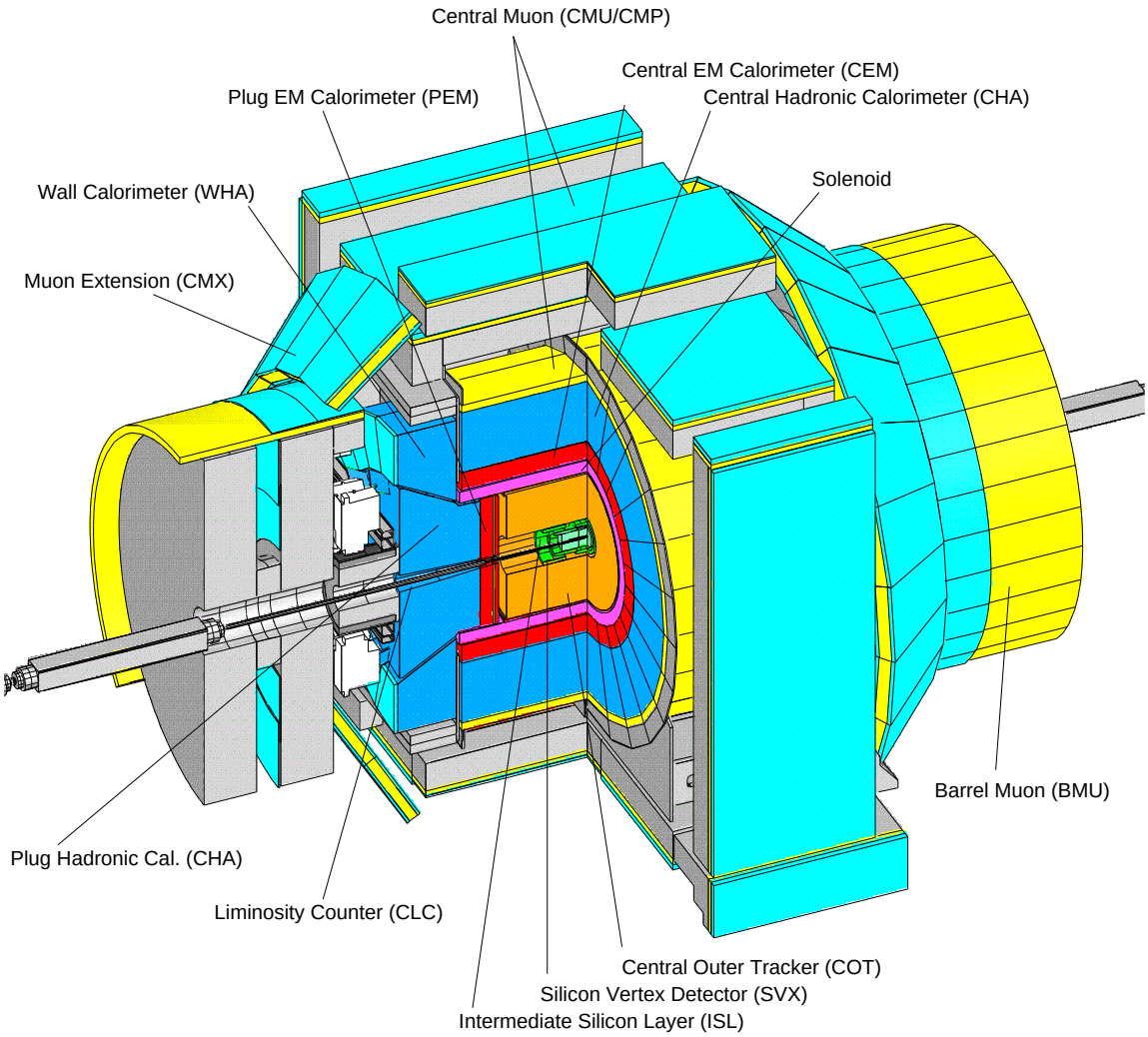

Figure 3.2: Schematic drawing of the CDF detector.

to the Tevatron accelerator complex. CDF is an azimuthally and forward-backward symmetric apparatus designed to study $p\bar{p}$ collisions at the Tevatron. It is a general-purpose solenoidal detector that combines precision charged particle tracking with fast projective calorimetry and fine grained muon detection. A schematic view of the detector is shown in Figure 3.2. CDF has a cylindrical layout centered on the accelerator beam-line. Tracking detectors are installed in the region directly around the interaction point to measure charged particle trajectories inside a uniform magnetic field. The field is produced by a 5m long superconducting solenoid located at the outer radius of the tracking region. It is aligned along the proton beam direction and has a strength of 1.4 Tesla. Calorimeter

modules are arranged in a projective tower geometry around the outside of the solenoid to provide energy measurements for both charged and neutral particles. The outermost part of the detector consists of drift chambers used to detect muons which typically pass through the calorimeter.

CDF uses a cylindrical coordinate system shown in Figure 3.3. The positive z-axis is defined along the direction of the protons. A trajectory of a particle is then described by the polar angle θ measured relative to the incoming proton beam, and the azimuthal angle ϕ around the beam axis. It is usually convenient to replace θ by the pseudo-rapidity,

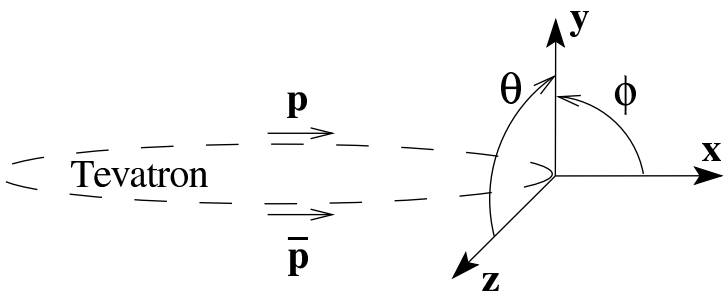

Figure 3.3: Definition of CDF coordinate system.

defined as $\eta = -ln\ tan(\theta/2)$ since it transforms linearly under boosts in the z-direction[2]. Perpendicular to the beam, $|\eta|$ becomes 0 and extends to approximately 3.6 at the most forward part of the detector.

3.2.1 The Tracking System

The tracking system consists of a silicon micro-strip detector and an open-cell wire drift chamber that surrounds the silicon detector. When a charged particle passes through the tracking system it ionizes the material/gas around it. A dedicated tracking algorithm searches for a continuous pattern of localized charge depositions (hits) and reconstructs the path of the charged particle, called the particle's 'track'.

[2]This is exactly true for the rapidity, defined as $y = \frac{1}{2} ln \frac{E+p_z}{E-p_z}$, but also for the pseudo-rapidity in the limit of massless particles.

The silicon micro-strip detector consists of three sub-detectors shown in Figure 3.4. The first is the Layer00 detector. This is a layer of radiation hard silicon wafers which

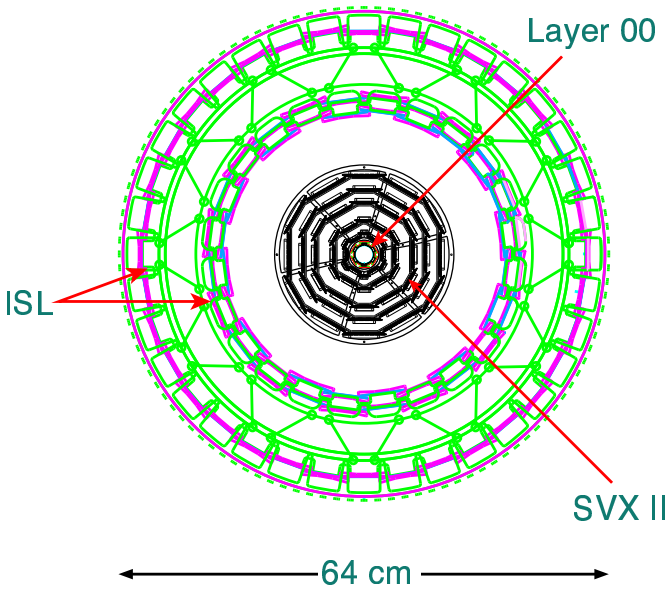

Figure 3.4: Frontal view of the silicon detector sub-systems.

is directly mounted around the beam pipe. The second sub-system is the Silicon VerteX detector (SVX II), which consists of 5 layers of double sided silicon wafers extending from a radius of 2.4 to 10.7 cm from the beam. One side of the wafer has silicon strips aligned in the r-ϕ plane (axial), while the other side has strips that are either parallel to the beam (stereo) or at a 2 degree angle (small angle stereo). The Intermediate Silicon Layer provides 2 more layers of double sided silicon wafers and extends from radii 20 to 28 cm. The entire system allows track reconstruction in three dimensions with precision track information at the smallest possible radii. The impact parameter resolution of the silicon detector is on the order of 40 μm. Information recorded by the SVX II is used in this analysis to reconstruct secondary vertices that originate from heavy-flavor particle decays such as bottom and charm hadrons. This is crucial for b-quark-tagging algorithms to work which is explained in Section 4.4.2 in more detail. The silicon detector provides tracking information out to a pseudo-rapidity region of $|\eta| < 2.0$.

The new open-cell drift chamber, referred to as Central Outer Tracker (COT), is

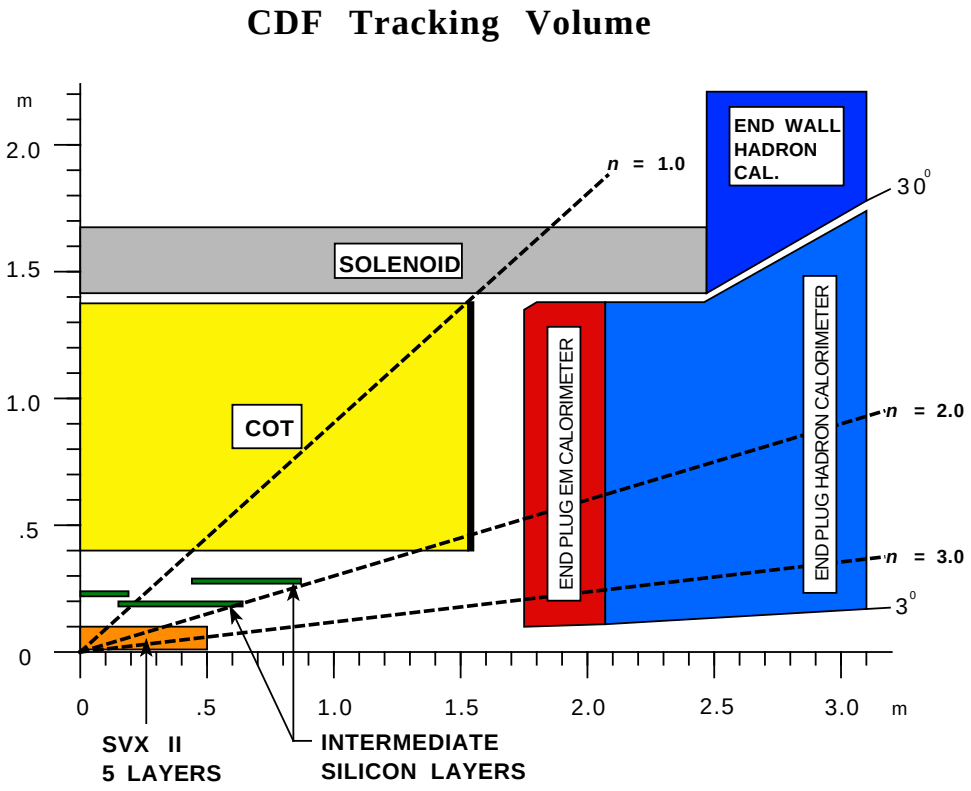

Figure 3.5: Schematic drawing of the CDF tracking volume.

located directly outside of the silicon tracking detectors in the radial direction. The chamber consists of eight super-layers (SL) of 310 cm length cells and radii between 40 and 132 cm from the beam axis. Each super-layer contains 12 layers of sense wires strung between alternated layers of potential wires. The wires in four of the super-layers are taut parallel to the beam axis to provide particle track reconstruction in the transverse plane (axial layers). The other 4 super-layers are taut at a $\pm$ 2 degree angle with respect to the beam axis to allow for track reconstruction in the z-direction (stereo layers). The two types of super-layers are alternated in the chamber starting with a stereo layer at the innermost radius. The COT is filled with a gas mixture of about 60% argon and 40% ethane. The mixture was chosen to ensure a fast drift velocity on the order of 100 μm/ns. Since the maximum drift distance in the chamber is 0.88 cm, it is compatible with the shorter interval between beam bunch crossings in Run II.

The charge and momentum of a particle-track are determined by measuring the cur-

vature of the track in the magnetic field. The solenoid produces a 1.4 T magnetic field inside the tracking volume that is uniform to 0.1 % in the acceptance region. The transverse momentum of a reconstructed track is determined from $p_T = Bqr$, where B is the strength of the magnetic field, q is the charge of the particle and r is the measured radius of curvature. The momentum resolution of the COT is given by $\sigma_{p_T}/p_T^2 = 1.7 \times 10^{-3}$ $[\mathrm{GeV/c}]^{-1}$.

3.2.2 The Calorimeter System

The CDF calorimeter is a sampling scintillator calorimeter and measures the energy of particles produced in the $p\bar{p}$ collision. The calorimeter is located behind the tracking volume and consists of layers of active (scintillator) material sandwiched between sheets of absorbing material such as lead and steel. As particles pass through the calorimeter, they interact with the layers of material and produce 'showers' of secondary particles. Light guides collect photons produced in the scintillator layers and direct them to the photomultiplier-tubes. Due to the specific nature of the interactions of particle with the material, electrons and photons shower over short distances, depositing the majority of their associated energy in the electromagnetic section of the calorimeter. Hadrons (strongly interacting particles), on the other hand, shower over longer distances in the calorimeter and deposit the most significant fraction of their associated energy in the hadronic section of the calorimeter. In the CDF detector, the electromagnetic sections of the calorimeter are immediately followed by the hadronic sections. The calorimeter is divided into a central calorimeter (and endwall part) covering $0 < |\eta| < 1.1$ (1.3), and a forward plug calorimeter covering $1.1 < |\eta| < 3.6$.

The central calorimeter is unchanged from Run I and consists of 48 azimuthal wedges of 15° in ϕ. Each wedge is grouped into 10 readout towers (often called calorimeter towers) with a projective geometry, as shown in Figure 3.6. The calorimeter contains an inner electromagnetic section (CEM) and an outer hadronic (CHA/WHA) section. The CEM

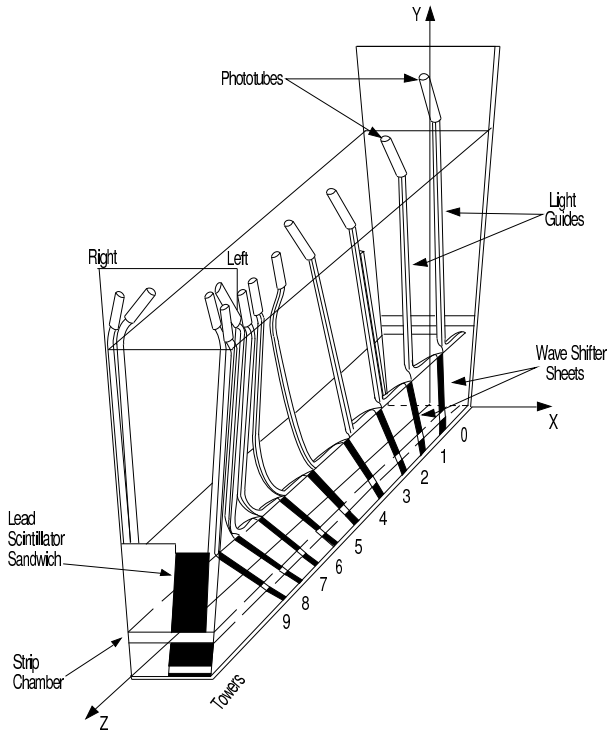

Figure 3.6: Schematic drawing of a wedge in the central calorimeter.

contains 31 layers of 0.125 cm of lead interleaved with 5.0 mm of polystyrene scintillator. The CHA is made of 32 layers of 2.5 cm steel interleaved with 1.0 cm scintillator. The WHA was constructed with 15 layers of 5.0 cm of steel and 1.0 cm of scintillator.

The forward plug calorimeter has been upgraded for Run II. The original gas calorimeter was replaced with scintillator plate calorimetry using scintillator tiles readout by wavelength shifting fibers embedded in the scintillator. Both the new plug electromagnetic calorimeter (PEM) and the new plug hadronic calorimeter (PHA) use the same polystyrene based scintillator and photomultiplier tubes used in the CEM. The PEM contains 23 layers of 0.45 cm of lead interleaved with 4.0 mm of scintillator while the PHA is made of 23 layers of 2.5 cm steel interleaved with 1.0 cm of scintillator.

The energy deposited in all layers of the calorimeter is summed together for each calorimeter tower separately. The central calorimeter provides about 480 readout towers each covering $0.1 \times 15^\circ$ in $\eta \times \phi$ space. The plug calorimeter, shown in Figure 3.7,

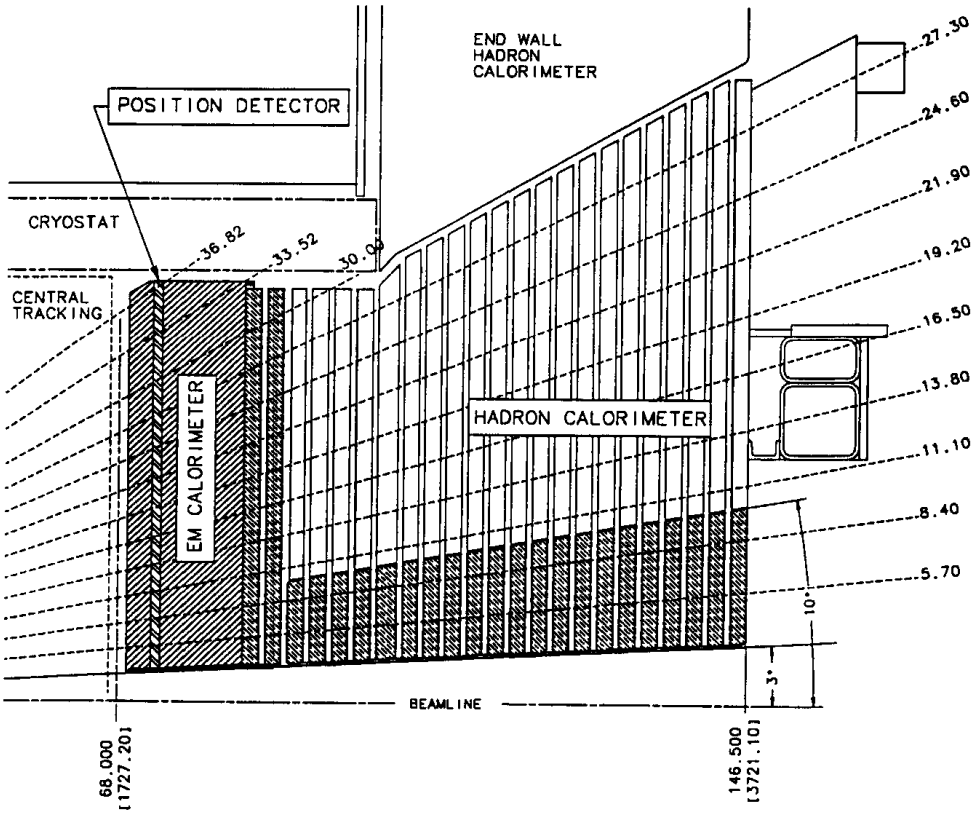

Figure 3.7: Schematic drawing of the CDF plug calorimeter.

provides another 480 readout towers, each covering either 7.5° or 15° in ϕ and a variable range in η.

The calorimeter energy resolution was measured using test-beam data. The measured energy resolution for electrons in the electromagnetic calorimeters was found to be $14\%/\sqrt{E_T}$ for the CEM and $16\%/\sqrt{E}$ for the PEM where the units of energy are GeV. The energy resolution for single pions in the hadronic calorimeter was found to be $75\%/\sqrt{E}$ for the CHA, $80\%/\sqrt{E}$ for the WHA, and $80\%/\sqrt{E} + 5\%$ for the PHA.

Proportional chambers are embedded in the region of the electromagnetic calorimeter where electrons produce the maximum shower intensity. These shower maximum detectors (CES in the central part and PES in the plug) are used to measure the profile of a shower and to extract the location of the incident particle within a given tower. The

increased shower position resolution provides additional selection criteria for electron identification.

A very common measure in high energy physics is the transverse component of momentum and energy which we define as $p_T = psin(\theta)$ and $E_T = Esin(\theta)$, respectively. In addition, the missing transverse energy, $\not\!\!E_T$ in an event is nominally defined as $\not\!\!E_T = -|\sum_i E_T^i \hat{n}_i|$, where the $\hat{n}_i$ are unit vectors in the azimuthal plane pointing from the reconstructed event vertex to the ith calorimeter tower. The missing transverse energy in the calorimeter is corrected to account for muons which deposit some fraction of their energy in the calorimeter (typically 1 - 2 GeV).

3.2.3 The Muon System

The muon detectors are located behind the calorimeter modules. Muons typically pass completely through the calorimeter modules leaving only a small fraction of their energy in the calorimeter (minimum ionizing). As a result, a muon must have a minimum p_T of 1.4-2.2 GeV/c (depending on the amount of material along its path) to reach the muon detectors. The CDF muon system consist of four independent systems of proportional wire chambers and scintillators: The Central Muon detector (CMU) and the Central Muon Upgrade (CMP) both cover $0 < |\eta| < 0.6$; the Central Muon extension (CMX) which covers $0.6 < |\eta| < 1.0$; and the Barrel Muon Upgrade Detector (BMU) which covers $1.0 < |\eta| < 1.5$. The BMU is a new detector system commissioned in the initial part of Run II and is not used in this measurement.

The CMU sub-detector consists of four layers of drift chambers as shown in Figure 3.8. The rectangular chambers have a 50 μm sense wire taut parallel to the z-axis through the center. The chambers are filled with a mixture of argon/ethane gas. As a muon candidate passes through the muon chambers, it ionizes the gas in the drift chambers. The hit position in the drift cells are determined from the drift time of the ions to the wire.

The CMP sub-detector consists of four layers of wire drift chambers of identical design to the CMU, but they are staggered by half cell per layer. The chambers are located behind 60 cm of steel and form a rectangular box around the detector. The CMP is mainly used in combination with the CMU detector to further improve the purity in muon identification and the combined system is referred to as the CMUP sub-detector. Located on top of the outermost layer of the CMP is the Central Scintillator Upgrade (CSP). The CSP system consists of a single layer of scintillator plates to provide additional timing information.

The CMX sub-detector is a conical arrangement of drift chambers similar to those of the CMP. Different to the CMU/CMP, the system consists of eight layers of rectangular chambers which are grouped in pairs to form four continuous layers. A matching layer of scintillator plates (CSX) are mounted on both sides of the CMX system which is used in coincidence with the wire chambers to further improve the timing of the system and reduce the fake rate (due to beam splashes for example).

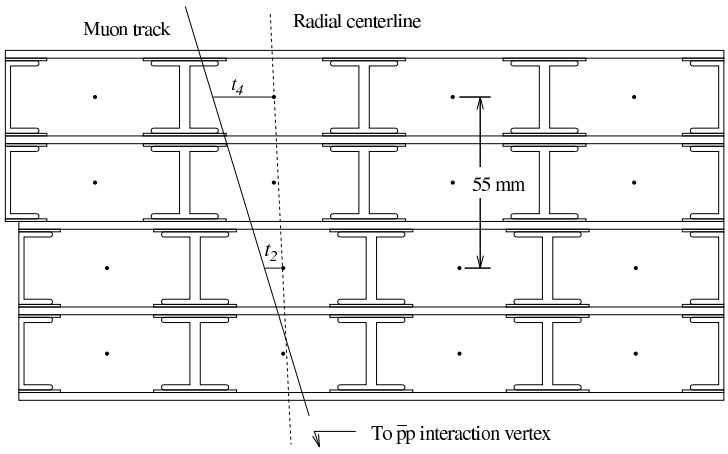

Figure 3.8: Schematic drawing of the CDF muon drift chambers (CMU).

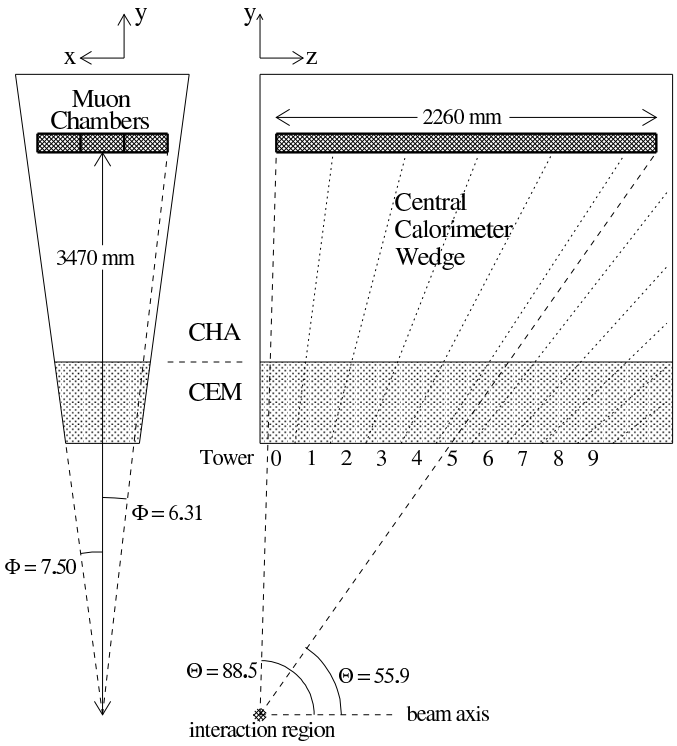

Figure 3.9: Schematic drawing of muon system behind the calorimeter.

3.2.4 Cherenkov Luminosity Counter

The total integrated luminosity recorded by the CDF experiment is measured by the Cherenkov Luminosity Counter (CLC) [36]. It consists of two modules at each end of the beam-pipe and measures the average number of inelastic $p\bar{p}$ collisions at CDF. Each module is made of 48 individual conical counters filled with isobutane. Each counter is 1-2m long and several cm in diameter. The counters are arranged around the beam-pipe in three concentric layers pointing to the center of the interaction region. The luminosity $\mathcal{L}$ is evaluated as:

$$\mathcal{L} = \frac{R_{p\bar{p}}}{\epsilon_{CLC} \cdot \sigma_{inelastic}} \tag{3.1}$$

where $R_{p\bar{p}}$ is the measured rate of inelastic $p\bar{p}$ collisions, ϵ_{CLC} is the CLC detector acceptance and $\sigma_{inelastic}$ is the total inelastic cross-section.

3.2.5 The Data Acquisition System

Currently, collisions in the Tevatron occur at a rate of 2.5 MHz and the average event size, representing information from all detector channels, is about 250 KBytes/event. If each event were to be read out, we would need to write 630 GBytes/s to disk - clearly a very challenging task. Luckily not each event contains physics of interest and CDF utilizes a 'trigger system' to select events for future analysis. The upgraded trigger system accept events at a rate of 80 Hz and writes them to disk. This corresponds to an event rejection factor of roughly 3×10^4 and is obtained by using a three-level system where each level is designed to provide sufficient rejection to allow for a processing with a minimal dead-time at each subsequent level. The first level of the trigger (Level-1) has to be the fastest and utilizes custom hardware to select events based on preliminary information from the calorimeters, tracking chamber and muon detectors. All detector data are fed into a 6 μs pipeline to provide time for processing required at Level-1. The global Level-1 decision must be made before the corresponding collision data reach the end of the pipeline. The Level-1 trigger reduces the data rate from 2.5 MHz to less than 20 kHz. The Level-2 system is a set of programmable logic devices which has access to more refined information including the silicon tracking system. The decision time is 20 μs and dedicated hardware is used to reconstruct clusters in the calorimeter for electron and jet reconstruction as well as simple track reconstruction. Level-2 provides a factor of 100 reduction over Level-1 passing a 300 Hz data rate to Level-3. Events which pass Level-2 are analyzed by a farm of approximately 300 computers, each fully analyzing and reconstructing events. Events which pass this last level of the trigger are delivered to the data-logger system which transfers the data to the storage as well as to the monitoring system. Monitoring ensures that the entire detector and trigger system were working properly during data taking. A maximum rate of 20 MBytes/s can be written to mass storage which corresponds to an event rate of about 80 Hz that can pass Level-3. Recent developments aim for an event-size reduction to increase the Level-3 accept rate to about

100 Hz.

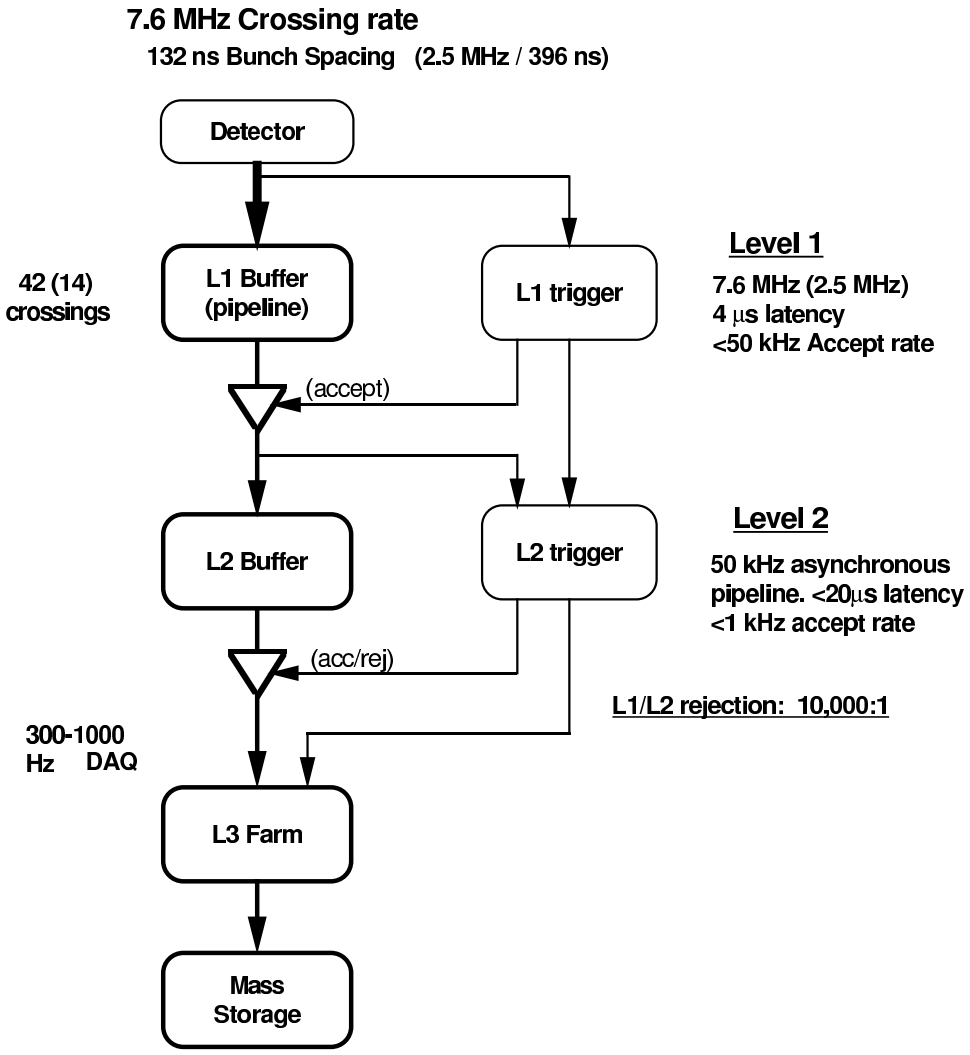

Figure 3.10: Diagram of the CDF dataflow.

3.2.6 Detector Operation

The CDF detector is operated by a shift crew of 5 dedicated people plus several detector experts available on request. The crew operates in 3×8 hour shift cycles and consists of the detector operations manager; two ACES, responsible for the smooth running of the detector and familiar with common problems of the detector; one Consumer Operator who is trained to monitor and ensure data quality; and one scientific coordinator (Sci-

Co). At the end of each store, the shift crew labels the data good or bad and documents any special circumstances during data taking. This information is later used by the Data Quality and Monitoring group (DQM) to prepare a list of good runs usable for physics analyses (Good Run List).

3.2.7 Offline Data Reconstruction

All data are reprocessed with the latest offline data analysis software before it is used by the physics groups of the CDF Collaboration. The best information about detector alignment, calibration and reconstruction algorithm is used to prepare a common set of 'high level objects' like electron, muon or track candidates.

3.2.8 Monte Carlo Simulation

The data collected by the CDF detector from interactions of the colliding proton and antiprotons are labeled 'events', which correspond to the data of individual collisions. The physics of a particular interaction is entirely random and the Standard Model predicts the rate (cross sections) at which we can expect certain processes to occur.

Using Monte Carlo techniques, we can simulate the production of particles as well as their interaction with the CDF detector. This is useful to understand the detection efficiencies of different processes and the dependence on selection requirements. The production of simulated events is performed by the event generator. The response of the detector (i.e. how the produced particles traverse the detector, bend in the magnetic fields, shower in the calorimeter) is performed by the detector simulation program. The output of the simulation program (referred to as 'Monte Carlo samples' in the text) has exactly the same format as the data, and can therefore be processed by the same reconstruction and analysis programs.

Event Generators

Monte Carlo event generators have a numerical expression of the QFT derived squared matrix element coded into the program. The program generates random events in phase space, each corresponding to a particular configuration of four-vectors of initial and final state particles. For each event, the total differential cross section is computed by evaluating the squared matrix element for the event and multiplying it with the phase space factor. The value of the differential cross section is treated as a 'weight', representing the relative probability for the event to occur. To convert these weighted events to unweighted (unit-weight) events, so that the denser regions of phase space are proportionally better represented (just like in data), the Acceptance Rejection de-weighing method is applied [37]. In this method, the phase space is scanned over the full kinematic range and the maximum weight w_{max} is determined. For subsequent events, the acceptance probability, R_i=$\mathrm{w}_i/\mathrm{w}_{max}$ is computed. A random number $y_i \in [0,1]$ is generated and the event is retained only if $y_i < R_i$. The resulting un-weighted events will show the same average behaviour and same fluctuations as data. The difference is that the fluctuations arise from the random sampling of the phase space rather than from the quantum mechanics of the underlying theory. The output of the event generators are four-vectors of the final state particles for a given process, commonly referred to as 'particle level' events since no particle shower or interaction with detector material is taken into account at this point.

Particle Shower and Hadronization

To model initial/final state radiation and the hadronization effects arising from color confinement of the particle level events, we use the PYTHIA [30] or HERWIG [38] programs. The Monte Carlo program QQ v9.1 is used to model B hadrons and TAUOLA [39] is used to model tau leptons. The event format after this step of the simulation is a long list (known as 'HEPG bank') of particle identities and four-vectors arising from the

initial interaction, showering and fragmentation of the event.

Detector Simulation

The GEANT program is used to describe the passage of the simulated particles through the CDF detector [40]. It provides a full simulation of the detector response as particles pass through matter. The GEANT model of the CDF detector contains detailed information on the shape, spatial extent and different material composition of every section of the detectors, from silicon layers to calorimeter towers and muon chambers.

Chapter 4

Event Selection

4.1 Selection Strategy

As outlined in Section 2.2, the final state of single top events consists of the W decay products plus two high momentum jets. If the W decays into quarks ($W \rightarrow q\bar{q}'$), the final state consists of four energetic jets. This final state suffers from an overwhelming background from pure QCD multi-jet events and is extremely hard to distinguish. We do not consider this final state in this analysis. Instead, we demand evidence for a leptonic W boson decay ($W \rightarrow e\nu_e, \mu\nu_\mu, \tau\nu_\tau \rightarrow e\nu_e\nu_\tau/\mu\nu_\mu\nu_\tau$) which is hard for QCD multi-jet background to mimic.

The CDF top analysis group has established a dedicated 'lepton plus jets' working group to study leptonic decays of the W plus jets production relevant for $t\bar{t}$ production. Since the kinematics of W decay daughters from top decays are naturally very similar for the single top and $t\bar{t}$ process, we apply mainly the same event selection.

In Figure 4.1 a cartoon of single top quark production and its decay is shown. While the leptonic W decay requirement greatly reduces background from pure QCD multi-jet processes, a large background still remains from mixed QCD/electroweak processes, which produce a real W boson along with jets. Since single top events feature at least

one high p_T b-jet in the final state, we can reduce this QCD/electroweak W+jets background by demanding evidence for at least one b-jet in the final state. The relatively long lifetime of b quarks permit the use of 'b-tagging' algorithms which can distinguish b-jets from light quark jets. The algorithm used in this analysis is described in Section 4.4.2. It relies on the reconstruction of a displaced secondary vertex, originated from the decay of the long lived b-quark, using the silicon micro-strip detector.

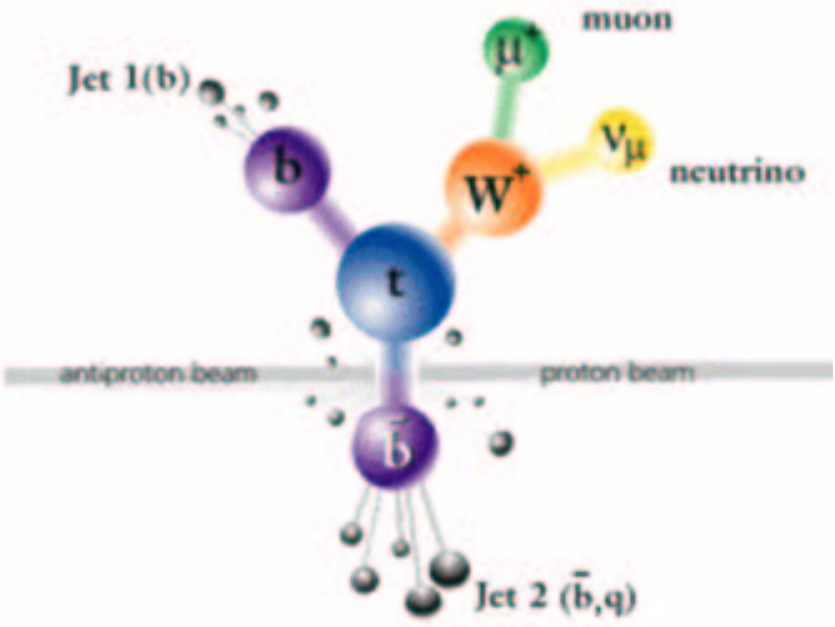

Figure 4.1: Cartoon of single top quark production.

An important requirement to establish the production of single top quarks, is to reconstruct one of its most distinct features, the top quark mass. We require candidate events to be reconstructed close to the top quark mass because it is a powerful requirement to further reduce the number of background events entering the event selection.

In summary, our event selection strategy requires a W + 2 jets signature where at least one jet has to be identified to likely contain a b-quark (b-tag). Furthermore, we require the invariant mass of the lepton, neutrino and the b-quark ($M_{l\nu b}$) to be close to

the top quark mass. Figure 4.2 shows the jet multiplicity for single top Monte Carlo events after all event selection requirements. We count jets with $E_T > 15$ GeV and $\eta < 2.8$. The large coverage in pseudo-rapidity improves especially the acceptance of t-channel single top which features a forward jet coming from the light quark recoiling against the virtual W-boson. Both single top processes are concentrated in the $W + 2$ jets bin[1].

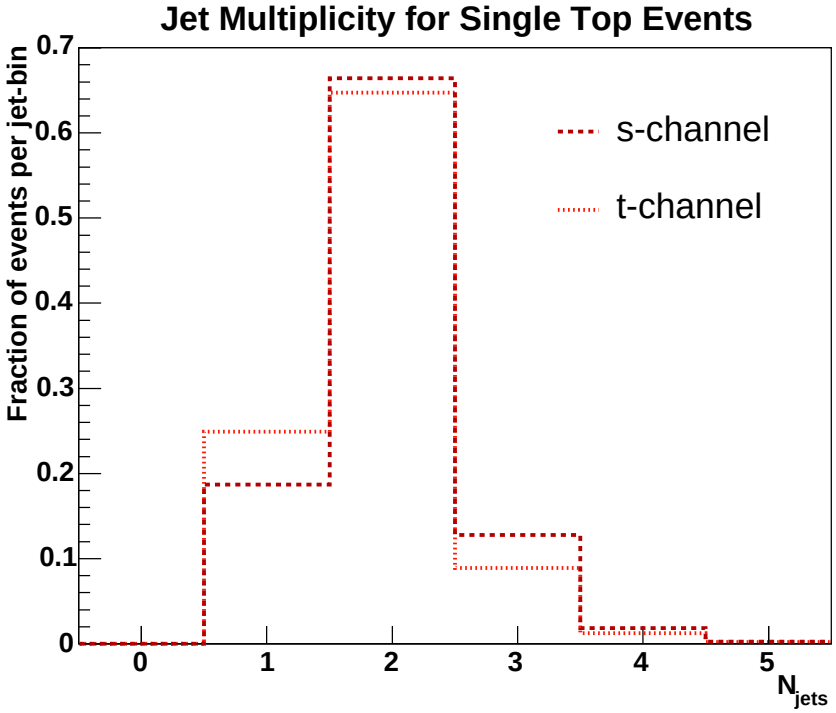

Figure 4.2: Jet multiplicity distribution for single top Monte Carlo events which pass all event selection requirements.

In the next Section, the trigger is described. The trigger pre-selects events with a high p_T muon or electron candidate. This pre-selection is performed 'online' during data taking and accepted events are transfered to mass storage devices. The collected dataset is then subject to the more detailed single top specific event selection described in Section

[1]The $W + 1$ jet bin suffers from a very large QCD/electroweak background and the $W + \geq 3$ jets bin is dominated by $t\bar{t}$ background so we don't include these jet bins in our event selection.

4.3 which is performed offline.

4.2 Trigger

The data sample used for this analysis was triggered by an inclusive central lepton trigger. It consists of the central electron trigger, which triggers on electron candidates in the CEM and two central muon triggers which trigger on muon candidates in the CMU/CMP and the CMX detectors. In Section 4.2.1 and Section 4.2.2, the specific trigger requirements are summarized.

4.2.1 Central Electron Trigger

At Level-1, energies from calorimeter towers are summed into $0.2\times15^\circ$ trigger towers in $\eta-\phi$ space. At least one trigger tower is required to have $E_T > 8$ GeV and a ratio of hadronic to electromagnetic energy in the tower $E_{had}/E_{em} < 0.125$ (which will serve as a 'seed tower' for the Level-2 trigger) is required. In addition, at least one COT track, found by the XFT hardware, with $p_T > 8$ GeV has to be reconstructed. At Level-2, a calorimeter cluster algorithm is run which adds adjacent towers to the seed tower identified at Level-1. The total E_T of the refined cluster is required to be above 16 GeV. At Level-3, an electromagnetic cluster with $E_T > 18$ GeV and $E_{had}/E_{em} < 0.125$ must be found by the offline algorithm and a fully reconstructed 3-dimensional COT track with $p_T > 9$ GeV has to be identified pointing to the cluster.

4.2.2 Central Muon Trigger

The central muon trigger requires, at Level-1, matched hits in at least 3 layers of either the CMU or CMX sub-detectors. In case of the CMU hits, a pattern of CMP hits in three of the four layers, consistent in ϕ with the observed CMU hits, has to be found. In case of the CMX trigger, a matching hit pattern in the CSX scintillator counters is

required. The matched hit pattern requirements are referred to as 'stubs'. In each case, a COT track, found by the XFT with $p_T > 4$ GeV/c has to be identified. At Level-2, the track requirement is increased to satisfy $p_T > 8$ GeV/c. The track has to be matched to the hits in the muon chambers. Finally, at Level-3, a fully reconstructed 3-dimensional COT track with $p_T > 18$ GeV/c has to be matched with reconstructed stubs in the CMU/CMP chambers or CMX sub-detector.

4.3 W Selection

Two major requirements have to be satisfied to identify events with a leptonic W decay in the data triggered by the inclusive lepton trigger described above. The first is the presence of an energetic isolated electron or muon candidate, and the second is large missing transverse energy, providing evidence for a neutrino that passed through the detector.

4.3.1 Electron Candidate Selection

An electron candidate is defined as a cluster of calorimeter towers with a COT track pointing to the cluster. The cluster algorithm starts with a seed tower containing transverse energy of $E_T > 3$ GeV in the electromagnetic calorimeter. The E_T of a tower is defined as $Esin(\theta)$, where E is the energy measured in the tower and θ is the polar angle measured from the $p\bar{p}$ interaction point to the center of the tower. Towers adjacent to the seed tower are added to the cluster up to a maximum of three towers in pseudorapidity. Table 4.1 lists the electron candidate identification requirements applied in this analysis. Several distributions of these selection variables are shown in the Appendix A. An explanation of the selection criteria is listed below.

- Geometric

  Only electron candidates which shower in the CEM are considered

Electron Candidate	
Geometric	Fiducial in CEM
E_T	$\geq$ 20 GeV
P_T	$\geq$ 10 GeV/c
E/p if $P_T \leq$ 50 GeV/c	$\leq$ 2
E_{had}/E_{em}	$\leq$ 0.055+0.00045*E
L_{shr}	$\leq$ 0.2
$\lvert\Delta z\rvert$	$\leq$ 3 cm
$Q \times \Delta x$	$>$ -1.5 and $<$ 3.0 cm
χ^2_{Strip}	$<$ 10
$\lvert\Delta z_0\rvert$	$<$ 60 cm
# axial SL	$\geq$ 3
# stereo SL	$\geq$ 3
Isolation	$<$ 0.1

Table 4.1: Electron identification requirements.

- E_T

  Total transverse energy of towers in the cluster.

- p_T

  Transverse momentum of the COT track pointing to the cluster.

- E/p

  Ratio of the cluster energy to the magnitude of the momentum of the COT track.

- E_{had}/E_{em}

  Ratio of energies measured in the hadronic and the EM towers of the cluster.

- L_{shr}

  A measure of the difference in lateral development of an electron candidate's shower

profile compared to the expected profile as measured in test beam data.

- $|\Delta z|$

  Distance in the $r - z$ plane between the extrapolated COT and the best matching shower maximum (CES) strip cluster.

- $Q \times \Delta x$

  The charge of the track, Q multiplied by the distance in the $r - \phi$ plane between the extrapolated COT and the best matching shower maximum (CES) wire cluster.

- χ^2_{Strip}

  χ^2 of the fit to the shower profile in the shower maximum detector.

- $|\Delta z_0|$

  z position of the primary vertex relative to the nominal collision point.

- # axial/stereo SL

  Number of axial/stereo super layers with hits associated to the COT track, pointing to the EM cluster.

- Isolation

  A measure of calorimeter activity in the immediate surrounding of the electron candidate. Isolation is the ratio of excess E_T in the cone over the E_T in the cluster

$$Isolation = \frac{E_T^{cone} - E_T^{cluster}}{E_T^{cluster}}$$

  where E_T^{cone} is the E_T of all towers in a cone of $\Delta R = \sqrt{\Delta_\eta^2 + \Delta_\Phi^2} = 0.4$ centered on the electron cluster (typically contained within $\Delta R \simeq 0.13$) and $E_T^{cluster}$ is the total E_T of towers included in the cluster.

4.3.2 Muon Candidate Selection

A muon candidate is defined to have a track segment (stub) in a muon chamber associated with a COT track pointing to the stub. Table 4.2 lists the muon identification requirements applied in this analysis for muon candidates. A few distributions of these selection variables are shown in the Appendix A.

Muon Candidate	
Geometric	Fiducial in CMUP or CMX
P_T	$\geq$ 20 GeV/c
E_{em}	$<$ max(2.2+0.0115*(p-100))
E_{had}	$<$ max(6.6+0.0280*(p-100))
$\|\Delta x\|_{CMU}$	$<$ 3.0 cm
$\|\Delta x\|_{CMP}$	$<$ 5.0 cm
$\|\Delta x\|_{CMX}$	$<$ 6.0 cm
$\|\Delta z_0\|$	$<$ 60 cm
# axial SL	$\geq$ 3
# stereo SL	$\geq$ 3
Isolation	$<$ 0.1

Table 4.2: Muon identification requirements.

- Geometric

  Only muon candidates fiducial to the CMU, CMP and CMX are considered.

- P_T

  The COT measured transverse momentum pointing to the muon candidate stub.

- E_{em}

  Energy deposited in the CEM tower traversed by the muon track.

- E_{had}

  Energy deposited in the CHA tower traversed by the muon track.

- $|\Delta x|$

  Distance between the muon stub and the extrapolated COT track in the $r - \phi$ plane.

- # axial/stereo SL

  Number of axial/stereo super layers with hits associated to the COT track pointing to the muon stub.

- $|\Delta z_0|$

  z position of the primary vertex relative to the nominal collision point

- Isolation

  E_T deposited in a cone of $\Delta R = 0.4$ centered on the muon track minus the E_T of the tower traversed by the muon candidate, divided by the p_T of the track.

4.3.3 Evidence for a Neutrino (missing transverse Energy)

Missing transverse energy ($\not\!\!E_T$), measured in the calorimeter, provides evidence for a neutrino that passed through the CDF detector without undergoing an interaction. $\not\!\!E_T$ is defined as the negative of the vector sum of the transverse energy over all calorimeter towers, $-\sum_i E_i sin\theta_i \hat{n}_i$, where E_i is the energy deposited in the ith calorimeter tower, θ_i is the polar angle of the ith tower, and $\hat{n}_i$ is the unit vector in the azimuthal plane pointing from the interaction point to the ith tower. The sum is computed over all calorimeter towers.

Since muons leave only a minimum amount of energy in the calorimeter, their energy does not get accounted for in the $\not\!\!E_T$ sum. For events which feature a muon candidate, the $\not\!\!E_T$ calculation is corrected for the presence of the muon in the following way:

$$(\not\!\!E_T{}^{corr})_x = (\not\!\!E_T{}^{raw})_x - (p_\mu)_x + (E_{T_\mu}^{depos})_x \quad (4.1)$$

$$(\not\!\!E_T{}^{corr})_y = (\not\!\!E_T{}^{raw})_y - (p_\mu)_x + (E_{T_\mu}^{depos})_y \quad (4.2)$$

The COT measured muon p_T is set equal to the muon E_T (this is a good approximation, since the muon mass is negligible compared to its kinetic energy) and vectorially added to $\not\!\!E_T$. The small amount of energy deposited in the calorimeter by the muon is vectorially subtracted.

4.4 Jet Selection

In this analysis, jets are identified using a cone-clustering algorithm that sums the energy of calorimeter towers which fall inside a cone of $\Delta R = \sqrt{\Delta_\eta^2 + \Delta_\Phi^2}$. The summed energy is referred to as 'raw' energy and is known to underestimate the energy of the original parton giving rise to the jet. Corrections to the jet energy measurement have therefore to be performed.

4.4.1 Jet Corrections

CDF categorizes jet corrections from several different sources into seven different 'levels'. Each correction level has the correction of lower levels included.

- **Level 1: Relative Energy Correction:**

  Corrects for inhomogeneous detector response and makes calorimeter response uniform over the full pseudo-rapidity range.

- **Level 2: Time Dependence:**

  Corrects for aging effects taking place in the calorimeter photo tubes.

- **Level 3: Raw Energy Scale:**

  The raw jet energy is scaled to the Run I energy calibration [41].

- **Level 4: Multiple Interactions:**

  The energy from different $p\bar{p}$ interactions during the same bunch crossing may fall inside the jet cluster which increases the energy of the measured jet and has to be subtracted. On average the number of interactions at the Tevatron per bunch crossing is $\approx$ 0.8 - 1.3 depending on the instantaneous luminosity.

- **Level 5: Absolute Energy Scale:**

  The jet energy measured in the calorimeter needs to be corrected for any non-linearity and energy loss in the un-instrumented regions of the calorimeter.

- **Level 6: Underlying Event Energy:**

  The underlying event energy is the energy associated with the recoil of the spectator partons in the hard $p\bar{p}$ collision.

- **Level 7: Out of Cone Corrections:**

  The out of cone corrections correct the particle-level energy for leakage of radiation outside the clustering cone used in the jet definition.

In this analysis, we count jets corrected with jet corrections level 4 and require the corrected $E_T > 15$ GeV and $|\eta| < 2.8$. To reconstruct kinematic event quantities, we correct the jets with all available corrections (level 7). Figure 4.3 shows the correction factors (level 4-7) as a function of (raw) jet p_T for (s-channel) single top Monte Carlo events.

4.4.2 b-quark Tagging

The b-quark has a relatively long lifetime of $\tau \approx 1.5 \times 10^{-12}$ s. Moreover, b-quarks from top quark decays have an average $p_T \approx 65$ GeV and therefore experience a significant Lorentz boost of $\gamma_T \approx 15$. This means that the B hadrons formed during the hadronization of the initial b-quark can travel a significant distance before decaying into a collection of

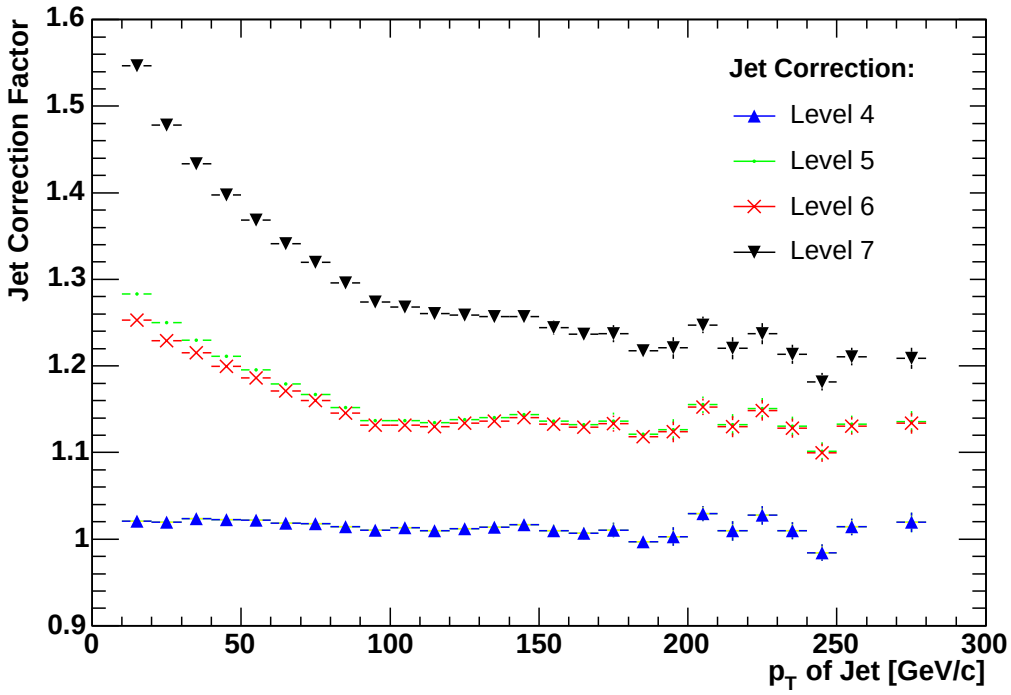

Figure 4.3: Correction factor for jet correction levels 4-7 as a function of (raw) jet p_T for (s-channel) single top Monte Carlo events.

lighter hadrons. This distance is given by $L = \beta c\tau'$, where β is the velocity of the particle in units of the speed of light $\beta \approx 1$ and τ' is the proper life time ($\tau' = \tau\gamma$). The average transverse distance traveled by the B hadron is therefore $L_T \approx 6.8$ mm. The spot where the decay happens can be reconstructed in the micro-strip silicon detector by identifying tracks which form a secondary vertex significantly displaced from the primary $p\bar{p}$ interaction point (primary vertex).

The b-tagging algorithm used in this analysis is SecVtx [42]. A loose set of quality requirements is applied to all tracks found in a cone of ΔR= 0.4 around the candidate's jet axis. The algorithm searches the set of accepted tracks for a set of three or more tracks that form a secondary vertex. If this attempt fails, a set of tighter selection requirements is applied to see if the jet contains at least two higher quality tracks that could form a secondary vertex. If either attempt is successful, the transverse distance L_{xy} from the

primary vertex of the event is calculated along with the associated uncertainty on L_{xy}, which we denote $\sigma_{L_{xy}}$. If the L_{xy} significance satisfies the condition:

$$L_{xy}/\sigma_{L_{xy}} \geq 3$$

the jet is considered 'tagged'.

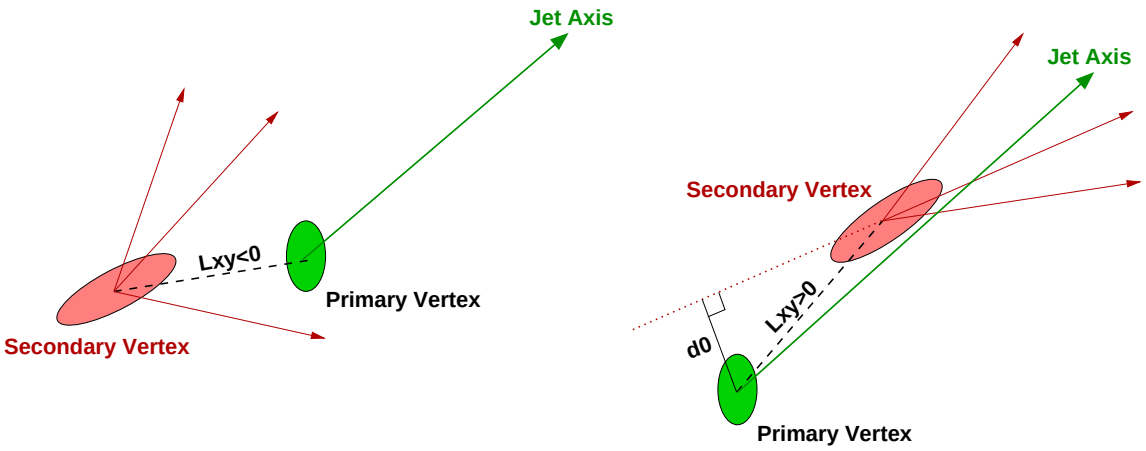

Figure 4.4: Cartoon showing fake ($L_{xy} < 0$) and true ($L_{xy} > 0$) reconstructed secondary vertices.

The sign of L_{xy} indicates the position of the secondary vertex with respect to the primary vertex along the direction of the jet as illustrated in Figure 4.4. If L_{xy} is positive, the secondary vertex points towards the direction of the jet. This is consistent with a B hadron traveling from the primary vertex in the direction of the jet. For negative L_{xy} the secondary vertex points away from the jet which may only happen by coincidence or as a result of mis-measured tracks. Jets tagged with a negative L_{xy} are labeled mis-tagged jets.

4.5 Event Vetoes

Several event vetoes (EV) are employed in this analysis to remove event topologies inconsistent with the signal event selection:

- **Z-Boson Veto**

  A Z + jets event, with the Z boson decaying into a pair of leptons, can mimic a W + jets event when one lepton, from the Z decay, is not reconstructed and mismeasured jets lead to a significant amount of missing energy. The Z veto removes events in which the primary lepton candidate forms an invariant mass with another loosely identified lepton of the same flavor but opposite charge within a window of $\pm$ 15 GeV around the Z mass (i.e. 76 to 106 GeV).

- **Dilepton Veto**

  Single top events feature only one high p_T isolated lepton. We therefore require exactly one such lepton to be reconstructed in either the CEM, CMUP or CMX. Events with more than one isolated lepton are rejected. The rejection requirement also searches for additional electron candidates reconstructed in the plug calorimeter (PEM) even though this part of the detector was not included in the trigger requirement. The dilepton veto is aimed to reduce $t\bar{t}$ background from events with two leptonic W decays.

- **Conversion Veto**

  Photon conversions into an electron/positron pair can occur in the detector material and are a source of electron backgrounds which have to be removed. A conversion is defined as a pair of oppositely charged tracks (one of which is the electron candidate) with a small separation in the $r - \phi$ plane ($|\Delta(xy)| < 2$ mm) at the point where both tracks are parallel and have a small difference in polar angle ($\Delta(cot\theta) < 0.04$).

- **Cosmic Ray Veto**

  Cosmic ray muons, produced from pion decays in the earth's upper atmosphere, pass through the CDF detector all the time. They are removed by rejecting events with a muon candidate which does not coincide with the beam crossing.

4.6 Reconstruction of $M_{l\nu b}$

The top quark decays almost always to a real W boson and a b quark. In this analysis we select events with evidence for a leptonic W decay. The invariant mass of the top quark can therefore be reconstructed through its decay products, the lepton, neutrino and the b-quark. The invariant mass, $M_{l\nu b}$, corresponds to the top quark mass.

$$M_{l\nu b} = \sqrt{(E_l + E_\nu + E_b)^2 - (\vec{p}_l + \vec{p}_\nu + \vec{p}_b)^2}$$

4.6.1 b-jet assignment:

The first step in the $M_{l\nu b}$ calculation is the identification of the b-quark four vector, $p_b = (E_b, \vec{p}_b)$, coming from the top quark decay. Our event selection criteria requires at least one b-tagged jet to be present. If there is exactly one b-tagged jet in the event, this jet is used for the $M_{l\nu b}$ calculation. If there are more b-tagged jets, we pick the one which has maximum $Q \cdot \eta$, where Q is the charge of the lepton and η is the pseudo-rapidity of the b-jet. The b-jet 3-momentum vector $\vec{p_b}$ is corrected by a scale factor obtained from the jet corrections (see Section 4.4.1). We use jet corrections level 7, which includes all available corrections. We set the b-jet mass to $m_b = 5$ GeV, and calculate its energy: $E_b = \sqrt{m_b^2 + \vec{p_b}^2}$.

Lepton assignment:

Our event selection requires exactly one charged lepton (e or μ) candidate in the event, which is assigned to the lepton four-vector

Neutrino assignment:

The neutrino remains undetected and we can only reconstruct the missing transverse energy $\not\!\!E_T$ which provides information for the p_x and p_y of the neutrino.

4.6.2 Calculating the neutrino p_z component:

The z-component of the neutrino momentum is unknown. However, under the assumption that we are dealing with a real leptonic W boson event the neutrino $p_{\nu,z}$ can be calculated up to a two-fold ambiguity using the following kinematic constraint:

$$p_W = p_l + p_\nu \quad \Rightarrow \quad m_W = \sqrt{(p_l + p_\nu)^2}$$

Squaring both sides (of the Equation on the left) provides us with the identity that the invariant mass of the lepton and the neutrino equals the mass of the W boson. Since the W mass is known very precisely, we can solve this Equation for the neutrino $p_{\nu,z}$ component:

$$p_{\nu,z} = \frac{-b \pm \sqrt{b^2 - 4ac}}{2a} \tag{4.3}$$

$$\begin{aligned} a &= p_{l,x}^2 + p_{l,y}^2 \\ b &= -(m_W^2 p_{l,z} + 2p_{l,x}p_{l,z}\,\not\!\!E_{Tx} + 2p_{l,y}p_{l,z}\,\not\!\!E_{Tx}) \\ c &= \not\!\!E_{Ty}(p_{l,x}^2 + p_{l,z}^2) + \not\!\!E_{T}{}_x^2(p_{l,y}^2 + p_{l,z}^2) - \frac{1}{4}m_W^4 \\ &\quad -m_W^2 p_{l,x}\,\not\!\!E_{Tx} - m_W^2 p_{l,y}\,\not\!\!E_{Ty} - 2p_{l,x}p_{l,y}\,\not\!\!E_{Tx}\,\not\!\!E_{Ty} \\ m_W &= 80.45 \pm 0.04 \text{ GeV/c}^2 \end{aligned}$$

Out of the two solutions, we choose the one which has the smallest absolute value. Complex solutions are obtained in about 30% of all cases due to detector resolution effects. In these cases, we use only the real part of the solution ($p_{\nu,z} = -b/2a$). The neutrino energy is assigned to $E(\nu) = \sqrt{\not\!\!E_T{}^2 + p_z^2}$.

The $M_{l\nu b}$ mass window has been chosen to be 35 GeV around the top quark mass such that only events with a $M_{l\nu b}$ value within $140 \leq M_{l\nu b} \leq 210$ GeV/c^2 are accepted. The specific choice of this event selection window is motivated in Section 5.3 in the context of background event rejection.

4.7 Event Detection Efficiency

Having established a set of specific selection requirements to implement our analysis strategy, we can now determine how many single top events pass on average these selection requirements. To do this, we apply the event selection requirements to fully simulated single top Monte Carlo samples. The fraction of events that passes all selection requirements is defined as ϵ_{evt}^{MC}, the event detection efficiency in Monte Carlo[2].

To calculate the number of predicted events (yield) in a certain dataset, we have to multiply the event detection efficiency with the predicted cross section and the integrated luminosity, $\mathcal{L}_{\mathsf{int}} = \int \mathcal{L} dt$, of the accumulated dataset.

$$\mathsf{N}_{\mathsf{evt}}^{\mathsf{predict}} = \sigma_{st}^{\mathsf{theo}} \cdot \epsilon_{\mathrm{evt}} \cdot \mathcal{L}_{\mathsf{int}} \tag{4.4}$$

It is known that Monte Carlo samples do not perfectly model every aspect of the CDF detector. The event detection efficiency measured in Monte Carlo needs to be corrected for these differences (ϵ_{corr}). Moreover, since our Monte Carlo dataset included only leptonic W decays, $W \to e\nu_e/\mu\nu_\mu/\tau\nu_\tau$, while the theoretical cross section is inclusive, we have to correct ϵ_{evt} with the branching ratio into leptons, $\epsilon_{\mathsf{BR}} = 0.3204$ [6]. We have no trigger requirement on our simulated samples, thus we make trigger efficiency corrections. All four correction factors are shown in equation 4.5. This completes the corrections to ϵ_{evt}^{MC} and defines the proper ϵ_{evt} to be used in Equation 4.4 to make a prediction on the expected event yield in data.

$$\epsilon_{\mathsf{evt}} = \epsilon_{\mathsf{evt}}^{\mathsf{MC}} \cdot \epsilon_{\mathsf{corr}} \cdot \epsilon_{\mathsf{BR}} \cdot \epsilon_{\mathsf{trig}} \tag{4.5}$$

The correction factor ϵ_{corr} in Equation 4.5 has contributions from different sources. Each source is described below:

$$\epsilon_{\mathsf{corr}} = \frac{\epsilon_{\mathsf{z0}}^{\mathsf{data}}}{\epsilon_{\mathsf{z0}}^{\mathsf{MC}}} \cdot \frac{\epsilon_{\mathsf{tag}}^{\mathsf{data}}}{\epsilon_{\mathsf{tag}}^{\mathsf{MC}}} \cdot \frac{\epsilon_{id}^{data}}{\epsilon_{id}^{MC}} \cdot \frac{\epsilon_{rec}^{data}}{\epsilon_{rec}^{MC}} \tag{4.6}$$

[2]sometimes also referred to as 'acceptance'

- $\epsilon_{\mathrm{z0}}^{\mathrm{data}}/\epsilon_{\mathrm{z0}}^{\mathrm{MC}}$

  The z vertex-cut efficiency differs in Monte Carlo compared to data. The numerical value is $\epsilon_{z0}^{data} = 0.951 \pm 0.005$ for data [44] and $\epsilon_{z0}^{MC} = 0.965 \pm 0.003$ for single top Monte Carlo.

- $\epsilon_{\mathrm{tag-jet}}^{\mathrm{data}}/\epsilon_{\mathrm{tag-jet}}^{\mathrm{MC}}$

  The Monte Carlo sample overestimates the b-tagging efficiency and therefore needs to be corrected. $\epsilon_{tag-jet}^{data}/\epsilon_{tag-jet}^{MC} = 0.82 \pm 0.06$ is the correction factor for the b-tagging efficiency [42]. This correction factor is defined per tagged b-jet. If our Monte Carlo sample would contain only events with exactly one b-jet per event, the factor would be applicable globally. However, since we also have events with two tagged b-jets the global correction factor has to be determined. One method is the counting method [45]. In this method, each b-tagged jet is considered individually and $1 - \epsilon_{\mathsf{tag}}^{\mathsf{data}}/\epsilon_{\mathsf{tag}}^{\mathsf{MC}} = 18\%$ of the jets are disregarded randomly and the remaining events with at least one b-jet are counted. The result for the global correction factor $\epsilon_{tag,global}^{data}/\epsilon_{tag,global}^{MC}$ is 0.826 for t-channel and 0.849 for s-channel single top.

- $\epsilon_{\mathrm{id}}^{\mathrm{data}}/\epsilon_{\mathrm{id}}^{\mathrm{MC}}$

  The lepton candidate selection requirements were summarized in Sections 4.3.1 and 4.3.2. The efficiency associated with this identification differs between Monte Carlo samples and data. The correction factor also varies for different sub-detectors and is summarized in Table 4.3 [46, 47, 48].

- $\epsilon_{\mathrm{rec}}^{\mathrm{data}}/\epsilon_{\mathrm{rec}}^{\mathrm{MC}}$

  This factor only applies to muon candidates and accounts for differences in the muon reconstruction in the Monte Carlo samples compared to data, see Table 4.3.

Since trigger, lepton-identification and muon-reconstruction efficiencies vary for different sub-detectors, equation 4.4 becomes a sum over all three detector regions:

$$\mathsf{N}_{\mathsf{evt}}^{\mathsf{predict}} = \sigma_{st}^{\mathsf{theo}}(\epsilon_{\mathrm{evt}}^{\mathrm{CME}} \cdot \mathcal{L}_{\mathsf{int}}^{\mathsf{CME}} + \epsilon_{\mathrm{evt}}^{\mathrm{CMUP}} \cdot \mathcal{L}_{\mathsf{int}}^{\mathsf{CMUP}} + \epsilon_{\mathrm{evt}}^{\mathrm{CMX}} \cdot \mathcal{L}_{\mathsf{int}}^{\mathsf{CMX}}) \tag{4.7}$$

Efficiencies	CEM	CMUP	CMX
Trigger	$\epsilon_{trig}^{\mathrm{CEM}} = 0.966 \pm 0.001$	$\epsilon_{trig}^{\mathrm{CMUP}} = 0.887 \pm 0.007$	$\epsilon_{trig}^{\mathrm{CMX}} = 0.954 \pm 0.006$
ID s.f.	$\epsilon_{id}^{data}/\epsilon_{id}^{MC} = 0.965 \pm 0.006$	$\epsilon_{id}^{data}/\epsilon_{id}^{MC} = 0.939 \pm 0.007$	$\epsilon_{id}^{data}/\epsilon_{id}^{MC} = 1.014 \pm 0.007$
Rec s.f.	-	$\epsilon_{rec}^{data}/\epsilon_{rec}^{MC} = 0.945 \pm 0.006$	$\epsilon_{rec}^{data}/\epsilon_{rec}^{MC} = 0.992 \pm 0.003$

Table 4.3: Trigger efficiencies and (data/Monte Carlo) lepton identification and muon-reconstruction efficiency scale factors (s.f.) for the various sub-detectors used in this analysis.

The accumulated data (integrated luminosity) is also slightly different for each sub-detector. Table 4.4 lists the integrated luminosity collected in each sub-detector used for this analysis.

Sub-detector	CEM	CMUP	CMX
$\mathcal{L}_{\mathsf{int}}$	162 ± 10 pb^{-1}	162 ± 10 pb^{-1}	150 ± 9 pb^{-1}

Table 4.4: Integrated luminosity collected in each sub-detector used for this analysis.

The number of predicted single top events which is expected to pass our event selection for this data sample is listed in Table 4.5 for the s-channel and in Table 4.6 for the

s-channel (σ_s=0.88 pb)	ϵ_{evt}	$\mathsf{N}_{\mathsf{evt}}^{\mathsf{predict}}$
Produced	-	142
Lepton+$\not\!\!E_T$+Vetoes	3.22% ± 0.25%	4.6 ± 0.7
Lepton+$\not\!\!E_T$+Vetoes+b-tag	1.62% ± 0.12%	2.3 ± 0.4
...+ $M_{l\nu b}$ window cut	1.06% ± 0.08%	1.5 ± 0.2

Table 4.5: Event detection efficiency and predicted number of events for s-channel single top after event selection requirements.

t-channel. The effective event-detection efficiency, ϵ_{evt}, weighted according to the integrated luminosity, and summed over all sub-detectors is also listed. The uncertainties on

the number of predicted events also include sources of systematic uncertainties on the single top yield which will be discussed in Section 6.5.1.

t-channel (σ_t=1.980 pb)	ϵ_{evt}	$\mathsf{N}_{\mathsf{evt}}^{\mathsf{predict}}$
Produced	-	317
Lepton+$\not\!\!E_T$+Vetoes	3.09% ± 0.24%	9.8 ± 1.6
Lepton+$\not\!\!E_T$+Vetoes+b-tag	1.06% ± 0.08%	3.4 ± 0.6
...+ $M_{l\nu b}$ window cut	0.89% ± 0.07%	2.8 ± 0.5

Table 4.6: Event detection efficiency and predicted number of events for t-channel single top after event selection requirements.

In summary, we expect 1.5 ± 0.2 s-channel single top events and 2.8 ± 0.5 t-channel single top events to pass the event selection requirements in 162 pb^{-1} of data.

Chapter 5

Background Composition

Several Standard Model processes are expected to pass the single top event selection described in Chapter 4 [42]. It is convenient to group these background processes into $t\bar{t}$ and non-top contributions. The first one refers to the $t\bar{t}$ pair production process and the second refers to all other QCD/electroweak processes with a W + jets final state. Since we require at least one b-tagged jet, the primary source (62%) of the non-top background is the W + heavy flavor jets processes $\bar{q}q' \to Wg$, with $g \to b\bar{b}$ or $g \to c\bar{c}$ and $gq \to Wc$. Additional sources are mistags (25%), where a light flavor quark jet in a $Wq\bar{q}'$ process is erroneously identified as a b-jet. QCD multi-jet production, where one jet fakes a lepton and mismeasured jets lead to significant $\not\!\!E_T$, is referred to as non-W and also contributes to the non-top background (10%). A smaller contribution (3%) is expected from direct diboson (WW, WZ, ZZ) production where one boson decays leptonically and the other into two jets.

5.1 Top-Antitop Background

Top pair production, shown in Figure 5.1, can mimic single top events in two ways: the first way is in the dilepton mode, where both W bosons from the top quark decays, decay leptonically and one lepton escapes detection. The other way is $t\bar{t}$ production in

the lepton plus jets mode in which one W decays leptonically and the other decays into two jets.

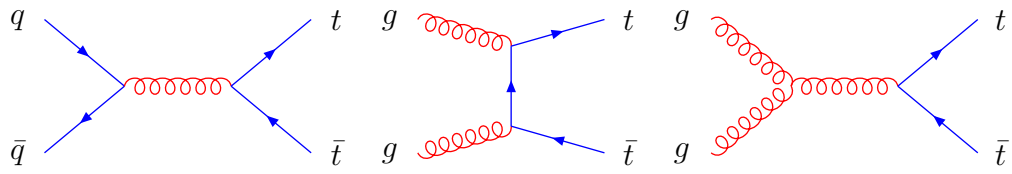

Figure 5.1: Some representative diagrams for $t\bar{t}$ production.

We calculate the predicted yield of this background by normalizing the Monte Carlo to the theoretical cross section (similar to the method used for the single top signal). To derive the event detection efficiency, we use a Pythia Monte Carlo sample. All correction factors are identical to the single top case, except for the global correction factor of the b-tagging efficiency: For $t\bar{t}$ $\epsilon^{data}_{tag-jet}/\epsilon^{MC}_{tag-jet} = 0.857$. The theoretical cross section has been calculated at NLO and is $\sigma_{t\bar{t}} = 6.7^{+0.71}_{-0.88}$ pb [49]. Table 5.1 summarizes the predicted $t\bar{t}$ yield in our data sample. The uncertainty on the predicted number of events includes the theoretical cross-section uncertainty (13.1%), the uncertainty on the event detection efficiency (8.4%) and the uncertainty on the top mass (7.6%) as well as a general uncertainty from effects like the PDFs, integrated luminosity, event generator and initial and final state radiation (15%).

$t\bar{t}$ (σ_t=6.7 pb)	ϵ_{evt}	$\mathsf{N}^{\mathsf{predict}}_{\mathsf{evt}}$
Produced	-	1179
Lepton+$\not\!\!E_T$+Vetoes	1.67% ± 0.13%	19.6 ± 4.0
Lepton+$\not\!\!E_T$+Vetoes+b-tag	0.75% ± 0.06%	8.8 ± 1.8
...+ $M_{l\nu b}$ window cut	0.36% ± 0.03%	3.8 ± 0.9

Table 5.1: Event detection efficiency and number of predicted $t\bar{t}$ events after event selection requirements.

5.2 Non-top Background

For most non-top processes, the theoretical cross section has only been calculated at leading order in perturbation theory and the production rates are therefore not well known (e.g. $Wb\bar{b}$, Wc, $Wq\bar{q}$). The CDF top analysis group has developed a method to calculate the yield of the non-top processes from data with the help of Monte Carlo samples [42]. This approach is summarized in Section 5.2.1. We have adjusted the method and the results obtained with it for use in the single top analysis [43].

5.2.1 Non-top Background Calculation

The strategy is to measure the number of direct W+jets events, $N_{W+jets}^{N_{jet}}$, using the data sample before the b-tagging requirement is applied (pre-tagged data). The superscript, N_{jet}, accounts for the jet multiplicity in the event. Direct W+jets production is not the only source of W candidate events in data. To calculate $N_{W+jets}^{N_{jet}}$, we count the total number $N_{data}^{N_{jet}}$ of W+jets candidates in data and subtract the contributions from all sources other than direct W+jets production. These sources include non-W, diboson and $Z \to \tau\bar{\tau}$.

$$N_{W+jets}^{N_{jet}} = N_{data}^{N_{jet}}(1 - F_{non-W}^{N_{jet}}) - N_{diboson}^{N_{jet}} - N_{Z\to\tau\bar{\tau}}^{N_{jet}} \tag{5.1}$$

The next step is then to estimate the number of W+jets events with heavy flavor jets. For this, we need to know the ratio of W+HFjets/W+jets. This ratio is obtained from Monte Carlo samples, but the normalization, N_{W+jets}, is from the data.

- $Wb\bar{b}$

  In the case of $Wb\bar{b}$ production, shown in Figure 5.2, a Monte Carlo sample is used to derive two ratios, $F1_{Wb\bar{b}}^{N_{jet}}$ and $F2_{Wb\bar{b}}^{N_{jet}}$, which represent the fraction of W+jets events in the N_{jet} bin, containing respectively, exactly one or two final state jets with a b-parton matched to that jet within a cone of $\Delta R < 0.4$ about the jet axis. Tagging efficiencies $\epsilon 1_{Wb\bar{b}}^{N_{jet}}$ and $\epsilon 2_{Wb\bar{b}}^{N_{jet}}$ are derived for both classes of events from Monte Carlo

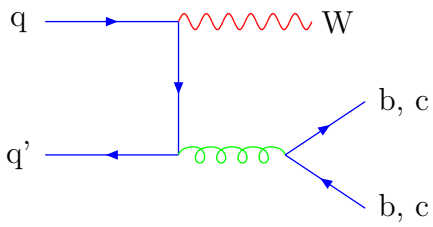

Figure 5.2: Diagram for $Wb\bar{b}$ or $Wc\bar{c}$ production.

samples and corrected with a data/Monte Carlo scale factor. The ratios are then normalized to the number of $W + N_{jet}$ events observed in the pre-tagged data to obtain the predicted number of $Wb\bar{b}$ events in each jet-multiplicity bin N_{jet} with at least one b-tagged jet:

$$N_{Wb\bar{b}}^{N_{jet}} = N_{W+N_{jet}}^{N_{jet}} \cdot (F1_{Wb\bar{b}}^{N_{jet}} \cdot \epsilon 1_{Wb\bar{b}}^{N_{jet}} + \epsilon 2_{Wb\bar{b}}^{N_{jet}} \cdot F2_{Wb\bar{b}}^{N_{jet}})$$

- $Wc\bar{c}$

  The calculation of the $Wc\bar{c}$ background is analogous to the $Wb\bar{b}$ background. To derive $N_{Wc\bar{c}}^{N_{jet}}$, we can use a similar formula as above:

$$N_{Wc\bar{c}}^{N_{jet}} = N_{W+N_{jet}}^{N_{jet}} \cdot (F1_{Wc\bar{c}}^{N_{jet}} \cdot \epsilon 1_{Wc\bar{c}}^{N_{jet}} + \epsilon 2_{Wc\bar{c}}^{N_{jet}} \cdot F2_{Wc\bar{c}}^{N_{jet}})$$

- Wc

  The calculation of the Wc background is also similar to the $Wb\bar{b}$ background, the normalization to data simplifies, because the process involves only one heavy flavor jet:

$$N_{Wc}^{N_{jet}} = N_{W+N_{jet}}^{N_{jet}} \cdot (F_{Wc}^{N_{jet}} \cdot \epsilon_{Wc}^{N_{jet}})$$

- Mistags

  The contribution from mistags is derived from a parametrization of the probability that a light quark jet will be misidentified as a b jet. This parametrization, known as

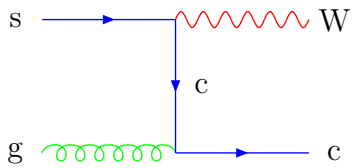

Figure 5.3: Diagram for Wc production.

the mistag matrix, depends on 5 jet parameters, the jet E_T, η, ϕ, sum of transverse energy in the event and track multiplicity. The mistag matrix is derived from the tagging rate with negative L_{xy} significance in generic QCD jet events. This parametrization is motivated by the fact that light quark jets are equally likely to have negative L_{xy} as positive L_{xy} tags. Therefore, the negative L_{xy} rate in generic jets is an approximation of the $+L_{xy}$ of light quark jets (i.e. mistag rate). To obtain the mistag contribution of a sample of $W + N_{jet}$ events, the mistag probability is computed for each jet in the event which is then summed over all events in the sample.

- Diboson

  The predicted number of diboson events in our data sample is calculated the same way as single top and the $t\bar{t}$ background. The theoretical cross section has been calculated for the Tevatron [50].

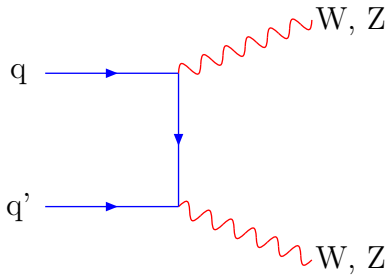

Figure 5.4: Diagram for Diboson production WW, WZ, ZZ.

- non-W

  The non-W contribution is derived from data. The method is based on the cor-

	WW	WZ	ZZ
σ at 1.96 TeV	13.30 pb	3.96 pb	1.57 pb

Table 5.2: Diboson cross sections.

relation of two quantities, the lepton isolation and $\not\!\!E_T$. We assume that in the pre-tagged sample, events containing a real W are confined in a region with large $\not\!\!E_T$ and low lepton isolation, while non-W events are evenly distributed in $\not\!\!E_T$ versus lepton isolation space, with no correlation. Four regions are defined to make quantitative prediction:

- Region A: $\not\!\!E_T \leq 15$ GeV, iso ≤ 0.1
- Region B: $\not\!\!E_T \leq 15$ GeV, iso ≥ 0.2
- Region C: $\not\!\!E_T \geq 20$ GeV, iso ≥ 0.2
- Region D: $\not\!\!E_T \geq 20$ GeV, iso ≤ 0.1 (W signal region)

Based on the assumptions made, the number of pre-tagged events in region D is: $(N_A \cdot N_C)/N_B$. The tagging efficiency is estimated from region B and D to calculate the number of events expected in the b-tagged sample.

The result of the background calculation for the various non-top background sources in the tagged W+2 jets sample is listed in Table 5.3. The efficiency of the $M_{l\nu b}$-window cut is obtained from Monte Carlo samples except for the non-W background which was obtained from QCD enriched data where the lepton isolation requirement was inverted (see Section 5.3).

In summary, we expect 30.0 ± 5.8 non-top events to pass the event selection requirements in 162 pb^{-1} of data. The uncertainties on the W+HF processes are correlated and therefore added linearly, the uncertainties on *Mistags*, non-W and dibosons are uncorrelated and were added in quadrature [42].

	$N_{Wb\bar{b}}$	$N_{Wc\bar{c}}$	N_{Wc}	$N_{Mistags}$	N_{non-W}	$N_{diboson}$
W+2jets+EV+b-tag	23.7±6.8	8.5±2.3	8.5±2.2	18.5±2.6	10.3±1.7	2.3±0.3
...+ $M_{l\nu b}$ window cut	11.0±3.4	3.6±1.1	3.8±1.1	7.5±1.6	3.0±0.7	1.0±0.1

Table 5.3: Number of predicted non-top background events after event selection requirements.

5.3 $M_{l\nu b}$ Mass Window

To further reject background events from entering our single top event selection and to improve our overall signal purity we require the invariant mass of the lepton, neutrino and the b-tagged jet, $M_{l\nu b}$ to be close to the top quark mass. We require all candidate events to fall within a $M_{l\nu b}$ window in order to be accepted. The method we use to calculate $M_{l\nu b}$ is outlined in Section 4.6.

By varying the size of the window around the top quark mass of $\simeq 175$ GeV/c^2 we can find the window which provides the optimal statistical signal significance, $S/\sqrt{(}B)$. Table 5.4 shows several mass window scenarios and their corresponding window efficiency for signal and background events together with the resulting signal significance. Three mass windows show similar good signal significance and we choose the one with the largest kinematic coverage, $140 \leq M_{l\nu b} \leq 210$ GeV/c^2.

Figure 5.5 shows the $M_{l\nu b}$ distribution for signal and background processes. The non-top background distribution is composed of $M_{l\nu b}$ distributions obtained from Monte Carlo samples of all sources listed in Table 5.3. The shape of the non-W distribution is taken from QCD enriched data which was obtained by selecting events where the isolation requirement was inverted. The relative contribution of each process is normalized to the expected yield for each process.

The single top signal is most likely to fall inside the mass window. The $t\bar{t}$ distribution is expected to be broader since it suffers from combinatorial ambiguity to assign the

$M_{l\nu b}$ window:	s-channel	t-channel	$t\bar{t}$	non-top	$S/\sqrt{(B)}$
100-250 GeV/c^2	0.93%	0.99%	0.78%	0.92%	0.65
105-245 GeV/c^2	0.92%	0.99%	0.75%	0.90%	0.65
110-240 GeV/c^2	0.90%	0.98%	0.72%	0.87%	0.66
115-235 GeV/c^2	0.87%	0.97%	0.70%	0.81%	0.67
120-230 GeV/c^2	0.84%	0.96%	0.66%	0.74%	0.68
125-225 GeV/c^2	0.81%	0.94%	0.63%	0.66%	0.70
130-220 GeV/c^2	0.77%	0.91%	0.58%	0.59%	0.71
135-215 GeV/c^2	0.72%	0.88%	0.53%	0.51%	0.73
140-210 GeV/c^2	**0.66%**	**0.84%**	**0.48%**	**0.45%**	**0.74**
145-205 GeV/c^2	0.60%	0.79%	0.43%	0.38%	0.74
150-200 GeV/c^2	0.54%	0.72%	0.37%	0.31%	0.74
155-195 GeV/c^2	0.46%	0.64%	0.31%	0.25%	0.72
160-190 GeV/c^2	0.36%	0.52%	0.24%	0.19%	0.67
165-185 GeV/c^2	0.26%	0.38%	0.17%	0.12%	0.59

Table 5.4: Efficiency of $M_{l\nu b}$ mass window cut for signal and background.

correct final state particles to the correct top quark, since the top quark is produced in pairs. The s-channel distribution has a longer tail at high masses than the t-channel for similar reasons. The b-jet recoiling against the top quark can sometimes be incorrectly assigned to be the b-jet from the top quark decay. The non-top distribution is expected to 'peak' at low $M_{l\nu b}$, which is an artifact of the minimum E_T threshold applied to the final state objects (i.e. jets, leptons, $\not\!\!E_T$). The distribution then falls all the way from there to the highest masses in the analysis.

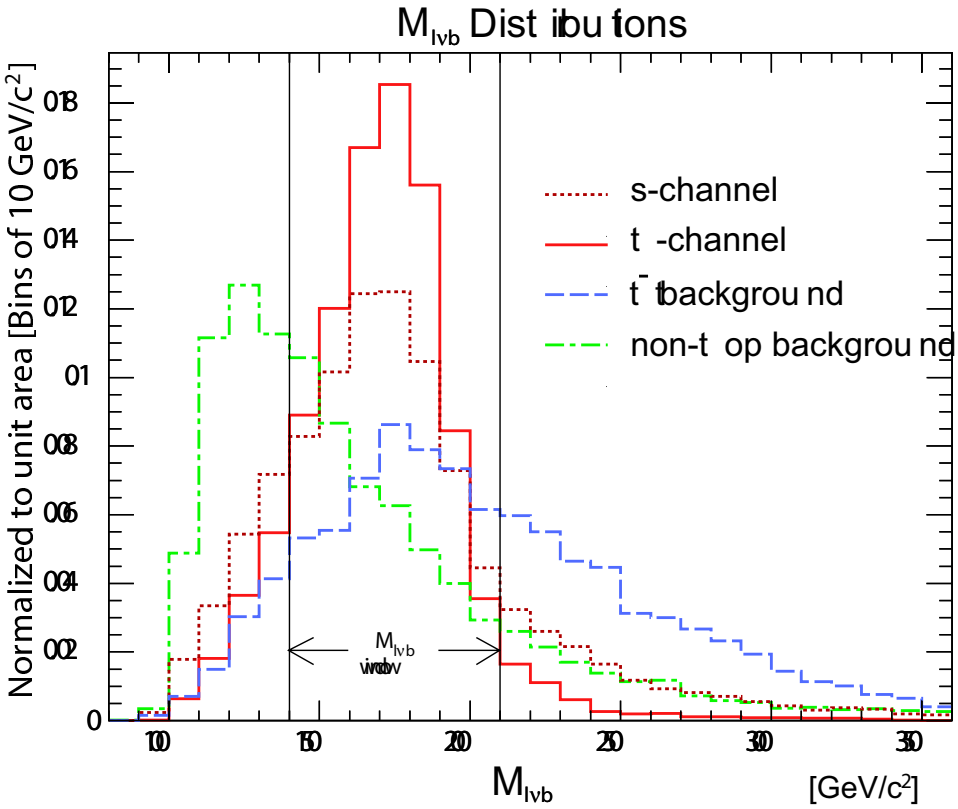

Figure 5.5: $M_{l\nu b}$ distributions for signal and background events. Only events which fall inside the $M_{l\nu b}$-window will be accepted in the analysis. The distributions are normalized to unit area.

5.4 Signal to Background Ratio

Extracting a single top signal is a challenging task because of the large number of background processes. We employ several powerful tools in this analysis to improve the signal to background ratio. Table 5.5 summarizes the signal to background ratio at various stages of the event selection. By selecting events which feature a W boson candidate plus two jets and pass the event veto rejections, the S/B is still as low as 1/201[1]. Requiring at least one b-tagged jet improves this by a factor of $\simeq$ 14. Adding the $M_{l\nu b}$ mass-window improves the S/B again by almost a factor of two. The next chapter will

[1]This is also the reason why the signal contribution in equation 5.1 was ignored.

Event selection	Signal (S)	Background (B)	S/B
W+2 jets + EV	14.4	2894	$\simeq 1/201$
W+2 jets + EV + b-tag	5.7	78.1	$\simeq 1/14$
W+2 jets + EV + b-tag + $M_{l\nu b}$ window	4.3	33.8	$\simeq 1/8$

Table 5.5: Signal to Background ratio after event selection requirements.

discuss the likelihood method we use to further improve our sensitivity to a single top signal and to better discriminate between signal and background.

Chapter 6

Maximum Likelihood Method

To quantify the single top content in the data, a maximum likelihood method is used [6]. We include the Poisson behaviour of the expected event yield, the independent background calculation and the shape information of the distribution of the kinematic variable H_T into the model.

6.1 Introduction

In this chapter, the maximum likelihood method is described used in this analysis. The data will be in the form of measured values of the kinematic variable H_T for N observed events[1]. We assume that each event is either from signal or background, i.e. $N = N_s + N_b$. Because of the small number of predicted signal and background events, we have to assume they are distributed according to a Poisson distribution with unknown means n_s and n_b. The likelihood function, $\mathcal{L}$, is a function of the unknown Poisson means n_s, n_b and is defined such that it expresses the joint probability of observing the N data events at their respective values of the kinematic variable H_T. The values n_s, n_b at which $\mathcal{L}$ achieves its maximum, corresponds to the most probable estimate for the true

[1]Data events which pass the event selection requirements described in Chapter 4.

signal and background content N_s, N_b in the data sample. In Section 6.2, the kinematic variable H_T is introduced. The shapes of the H_T distributions for single top, $t\bar{t}$ and non-top background are used as signal and background 'templates' in the definition of the likelihood function. The explicit expression of the likelihood function is explained in Section 6.3, and sources of systematic uncertainties that are incorporated into the analysis are discussed in Section 6.5.

6.2 Kinematic Variable H_T

Since two channels contribute to single top quark production, we can expect, *a-priori*, the highest sensitivity to a single top signal by combining both processes in the search. It is therefore best to identify a kinematic variable with a distribution that looks similar for s-channel and t-channel single top quark production and different for the backgrounds. The scalar sum of transverse energies of all final state particles in the event (H_T) is such a variable. We define it as:

$$H_T \equiv E_T^{lepton} + \not\!\!E_T + \sum E_T^{jets} \tag{6.1}$$

where all jets with raw $E_T > 8$ GeV and $|\eta| < 2.8$ in the event are included [2]. We apply jet corrections level 7 (defined in Section 4.4.1) to the identified jets. Figure 6.1 shows the distribution for s- and t-channel single top obtained from our single top MC samples. The shapes are very similar for both processes, which makes it a good variable for a combined (s-channel + t-channel) single top search.

We model the H_T distribution of the $t\bar{t}$ and the non-top background separately. The $t\bar{t}$ distribution is obtained from the $t\bar{t}$ Monte Carlo sample. The non-top distribution has contributions from all non-top processes and the relative contributions are taken from the *a-priori* event yield prediction summarized in Table 5.3. Figure 6.2 shows the super-

[2] The lower jet-E_T requirement, compared to the jet counting threshold, is motivated to better discriminate against $t\bar{t}$ events which have more final state particles in the event and therefore higher H_T.

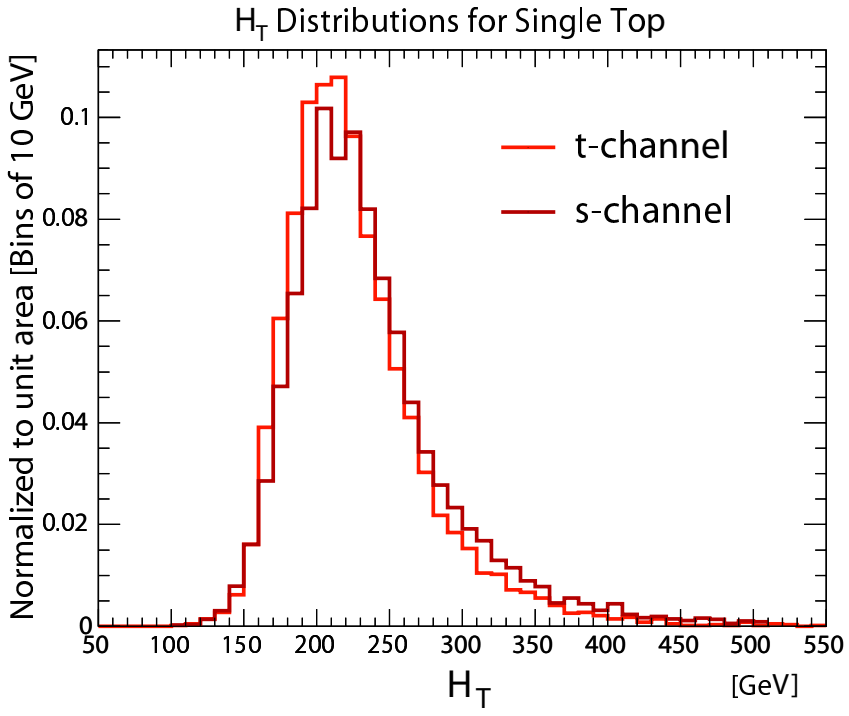

Figure 6.1: H_T distribution for both single top processes for events which pass all event selection requirements.

position of H_T distributions of all non-top processes. The distributions for $Wb\bar{b}$, $Wc\bar{c}$ and Wc are obtained from Monte Carlo samples generated with the ALPGEN program [51]. The distribution for the *Mistags* is obtained from a generic $Wq\bar{q}$ (ALPGEN) Monte Carlo sample weighted by the summed mistag probability of each jet in the event [42]. We obtain the non-W H_T-distribution from a QCD enriched sample where the isolation requirement of the lepton was inverted.

To remove statistical fluctuations from the binned histograms, the distributions are smoothed. To perform the smoothing, the H_T histograms are binned with a fine granularity of 1000 bins and each bin-content is averaged with the bin content of 20 bins on either side. The smoothed H_T templates for single top, $t\bar{t}$ and non-top background are shown in Figure 6.3. The non-top distribution is the smoothed version of Figure 6.2. All histograms are normalized to unit-area.

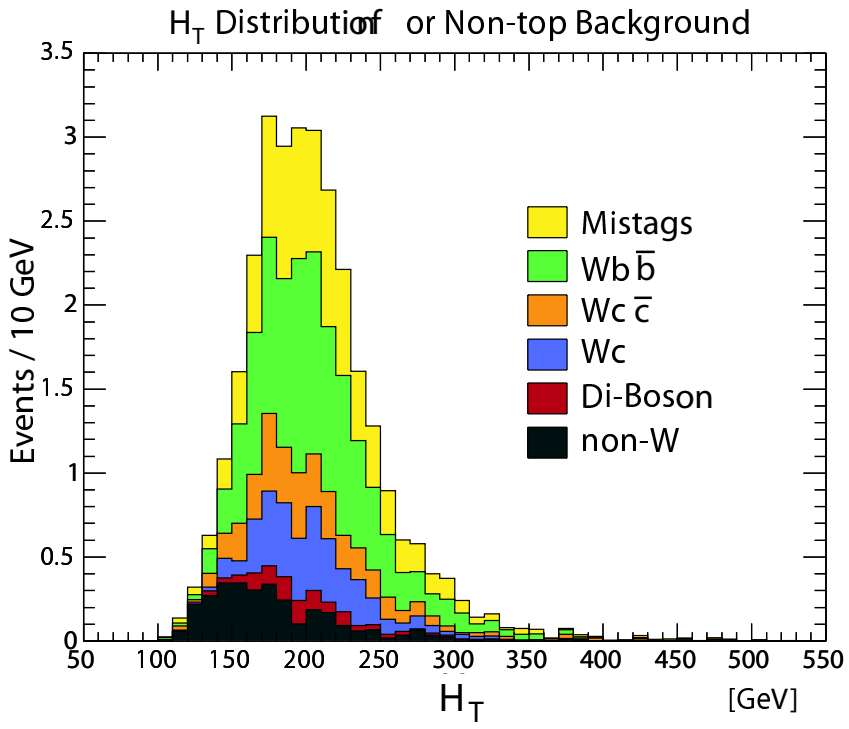

Figure 6.2: Total H_T distribution for the non-top background processes (for events which pass all event selection requirements). The relative contribution from each process is normalized to the predicted event yield summarized in Table 5.3.

6.3 Likelihood Function

The H_T distribution of the data is assumed to be a superposition of the single top, $t\bar{t}$ and non-top H_T distributions. The information we obtain from data is only the total number of events N, which pass our selection requirements and their individual values of H_T. Both the arrangement of signal and background events as well as the individual number of signal and background events are unknown. Using the likelihood method, we measure the single top and background normalizations, such that if N events observed in data were chosen from respective single-top and background Poisson distributions having those means, the likelihood of observing the data is maximized. The Poisson means for signal and background are parameters in the likelihood function shown in Equation 6.2. Three free parameters were chosen to represent the combined (s-channel + t-channel) single

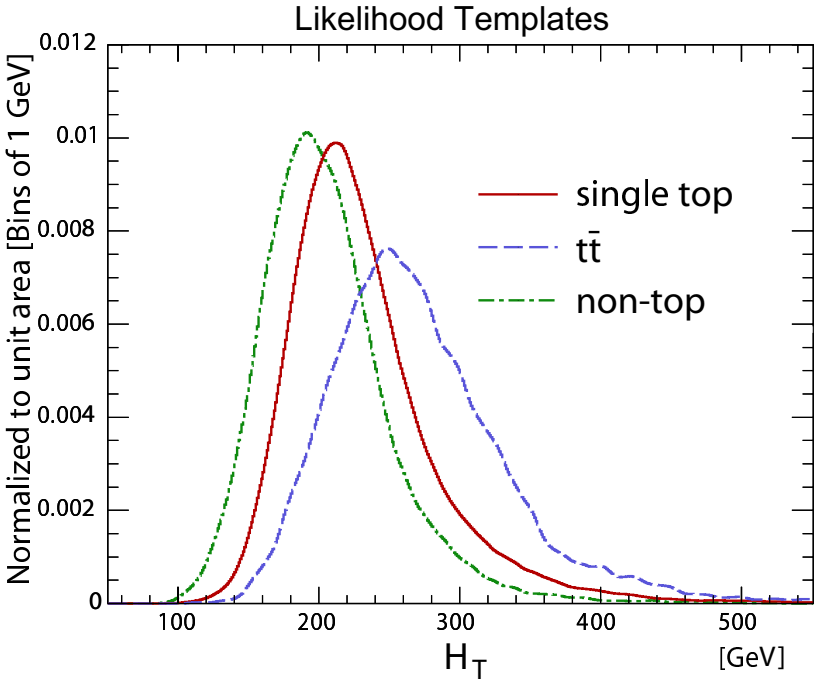

Figure 6.3: Smoothed H_T templates for signal and background normalized to unit area (only bins 50-550 are shown).

top (β_1), $t\bar{t}$ (β_2) and non-top (β_3) normalizations, where $\beta_j = n_j/\mathrm{N_j^{pred}} = \sigma_j/\sigma_{SM_j}$. The likelihood function can be expressed in three terms [52]. The first term takes the Poisson behaviour of the respective amounts of signal and background about Poisson means n_i into account (with $n = \sum_{i=0}^{3} n_i$). The second term embodies the event-by-event shape probability for signal and background, given the particular value of H_T of each event. The third term includes the information of our background estimate into the likelihood, particularly the uncertainty on the predicted yield of background events. We do this by including a factor which Gaussian constrains the free parameters for the background β_2 and β_3. The width of the Gaussian function is given by the predicted relative uncertainty of the $t\bar{t}$ ($\Delta_2 = 24\%$) and non-top background ($\Delta_3 = 19.5\%$).

$$\mathcal{L}(\beta_1,\beta_2,\beta_3) = \underbrace{\frac{e^{-n}n^N}{N!}}_{Poisson\ term} \underbrace{\prod_{k=1}^{N} \frac{\beta_1 F_1(H_{T_i}) + \beta_2 F_2(H_{T_i}) + \beta_3 F_3(H_{T_i})}{n}}_{Shape\ Probability} \underbrace{\prod_{j=2}^{3} G(\beta_j|1,\Delta_j)}_{Gauss\ constraints} \quad (6.2)$$

- $\beta_j = n_j/\mathrm{N_j^{pred}} = \sigma_j/\sigma_{SM_j}$: Free parameter for process j;
  j=1 for single top, j=2 for $t\bar{t}$, j=3 for non-top

- $\mathrm{N_j^{pred}}$: Predicted number of events for process j

- $n = \sum_{j=1}^{3} \beta_j n_j$: Most likely sum of signal and background Poisson means

- $F_j(H_T)$: Template for process j, normalized to the total number of events predicted for process j, i.e. $\int F_j(H_T) dH_T = \mathrm{N_j^{pred}}$

- $G(\beta_j|1,\Delta_j) = \frac{1}{2\pi\Delta_j^2} e^{-(\beta_j-1)^2/2\Delta_j^2}$: Imposes Gaussian constraints on the background parameters that deviate too much from the independent background prediction

6.4 Testing the Maximum Likelihood Method

To test the maximum likelihood method, we apply it to many pseudo-experiments. Each pseudo-experiment consists of a sample of fake data we would expect to obtain from repeated CDF II experiments. The distribution of fit parameters can then be statistically examined.

6.4.1 Generation of Pseudo-Experiments

Each pseudo-experiment consists of an ensemble of H_T values randomly generated according to the expected H_T distribution (template) for signal and background. Each pseudo-experiment is composed of $N_{single\ top}$, $N_{t\bar{t}}$ and $N_{non-top}$ Monte Carlo events, respectively. We compute the particular values of $N_{single\ top}$, $N_{t\bar{t}}$ and $N_{non-top}$ by numerically Poisson fluctuating the signal and background predictions summarized in Table 7.1. I.e. $N_{single\ top} = Poisson(\mathrm{N^{pred}_{single\ top}})$; $N_{t\bar{t}} = Poisson(\mathrm{N^{pred}_{t\bar{t}}})$; $N_{non-top} = Poisson(\mathrm{N^{pred}_{non-top}})$. We then randomly draw $N_{single\ top}$, $N_{t\bar{t}}$ and $N_{non-top}$ events from the Monte Carlo templates of Figure 6.3. The obtained dataset represents one pseudo-experiment. The ensemble of H_T values are, of course, different for each pseudo-experiment.

6.4.2 Result of Pseudo-Experiments

We apply the maximum likelihood method to each pseudo-experiment. To perform the task of maximizing $\mathcal{L}$ with respect to the parameters β_1, β_2 and β_3, we use the MINUIT software package [53]. MINUIT maximizes $\mathcal{L}$ most effectively by minimizing $-log\mathcal{L}$. MINUIT performs a gradient search for the minimum value of the user-supplied multi-parameter function using the Davidon-Fletcher-Powell algorithm [53]. In addition to finding the parameter values which minimize $-log\mathcal{L}$, MINUIT finds the uncertainty associated with the parameters. The statistical uncertainty reported by MINUIT corresponds to the amount by which the parameter would need to change in order to increase $-log\mathcal{L}$ by 0.5 units.

The distribution of parameter β_1, β_2 and β_3 which maximized the likelihood function in 10,000 pseudo-experiments is shown in Figure 6.4 (first column of graphs) together with the uncertainty on the fit parameter (second column of graphs) and the 'pull' distributions (third column of graphs). The pull is defined as the difference between the parameter value that maximized the likelihood function (reported by MINUIT) and the predicted value ($\beta = 1$ by definition) divided by the uncertainty on the parameter.

$$\text{pull}(\beta_i) = \frac{(\beta_i - 1.0)}{\sigma_{\beta_i}}$$

If the maximum likelihood method is performing correctly, we expect a pull distribution centered around zero and a width of unity (which is the case for all three parameters).

6.5 Incorporating Systematic Uncertainties

Sources of systematic uncertainty are incorporated in this analysis as nuisance parameters in the likelihood function, conform with a fully Bayesian treatment [54]. Most systematic uncertainties, such as the uncertainty on the jet-energy-scale, can affect the analysis in two ways: first, since we require the jets to have $E_T > 15$ GeV, a change in the

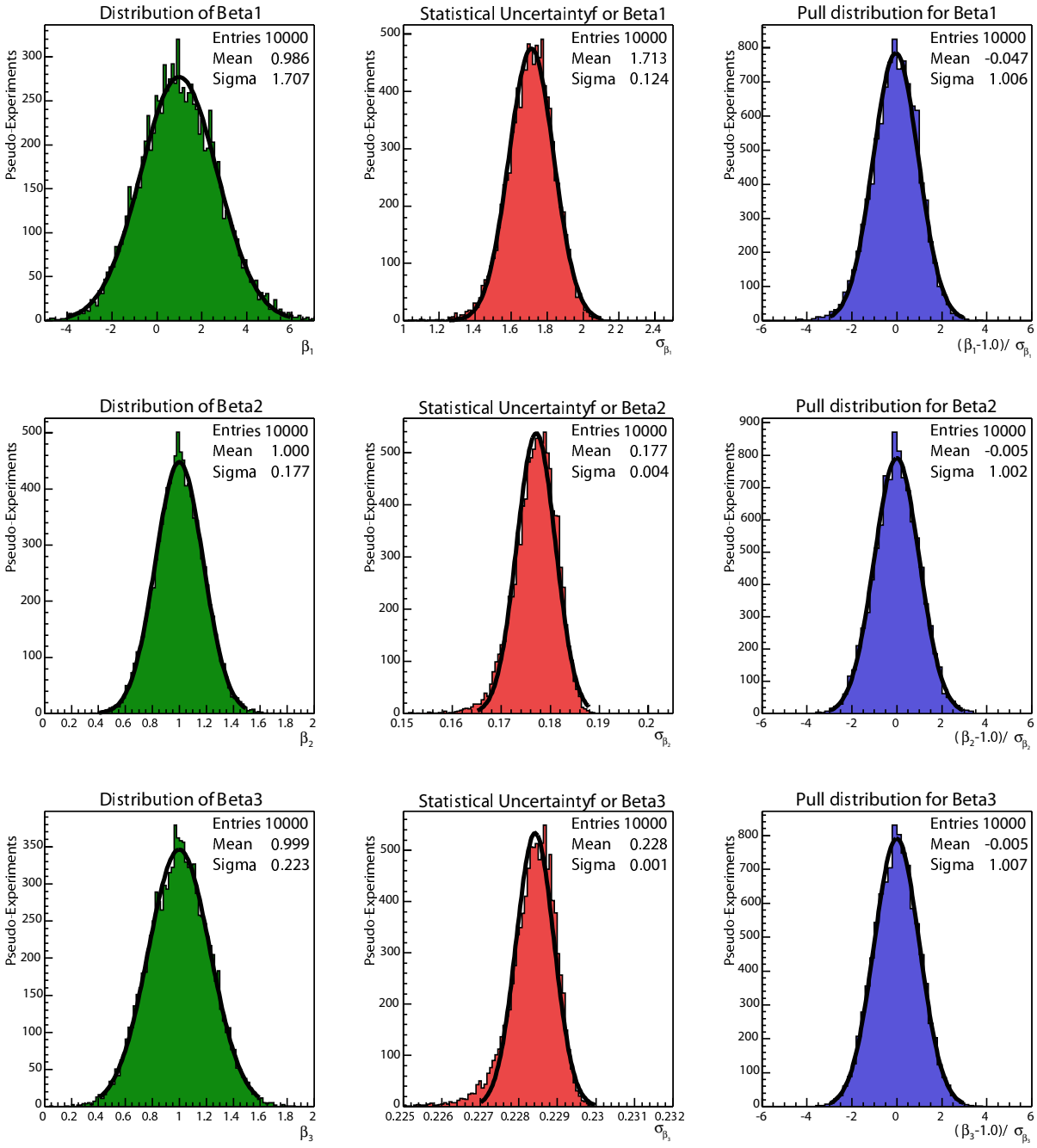

Figure 6.4: Distribution of maximum likelihood fit parameters, statistical uncertainty on the parameter and pulls for 10,000 pseudo-experiments using predicted amounts of signal and background from Table 7.1.

jet-energy-scale affects the event detection efficiency derived in Chapter 4 (we call this the 'normalization uncertainty'). Meanwhile, the shape of the H_T distribution, which depends also on jet energies, will also change (we call this the 'shape uncertainty'). We include all sources of systematic uncertainty into the likelihood and take the correlation between normalization and shape uncertainties for a given source into account [55]. To do this, we re-write Equation 6.2 as a binned likelihood function, as shown in Equation 6.3. This has the advantage that one can express the dependency of the likelihood on systematic effects (both shape and normalization) in finite intervals, given by the bin size. We choose 1000 bins[3] for H_T values ranging from k=0 to k=1000 GeV (i.e. the bin size is 1 GeV). In the binned likelihood, the Poisson term is applied to the expected number of events in bin k, μ_k, and the shape information is given by α_{jk}, which gives the content of the H_T template of process j in bin k. The H_T templates are normalized to the predicted number of events (i.e. $\sum_{k=0}^{1000} \alpha_{jk} = N_j$).

$$\mathcal{L}(\beta_1, \beta_2, \beta_3; \delta_1, ..., \delta_7) = \underbrace{\prod_{k=1}^{B} \frac{e^{-\mu_k} \cdot \mu_k^{n_k}}{n_k!}}_{Poisson\ term} \cdot \underbrace{\prod_{j=2}^{3} G(\beta_j|1, \Delta_j)}_{Gauss\ constraints} \cdot \underbrace{\prod_{i=1}^{7} G(\delta_i, 0, 1)}_{Systematics} \tag{6.3}$$

$$where,\ \mu_k = \sum_{j=1}^{3} \beta_j \quad \cdot \quad \underbrace{\left\{ \prod_{i=1}^{7} [1 + |\delta_i| \cdot (\epsilon_{ji+} H(\delta_i) + \epsilon_{ji-} H(-\delta_i))] \right\}}_{Normalization\ Uncertainty} \tag{6.4}$$

$$\underbrace{\cdot\ \alpha_{jk}}_{Shape\ P.} \quad \cdot \quad \underbrace{\left\{ \prod_{i=1}^{7} (1 + |\delta_i| \cdot (\kappa_{jik+} H(\delta_i) + \kappa_{jik-} H(-\delta_i))) \right\}}_{Shape\ Uncertainty} \tag{6.5}$$

Seven categories of systematic uncertainties, labeled by the index i, are considered in the likelihood: (1) the jet-energy-scale, (2) modeling of initial state radiation (ISR), (3) modeling of final state radiation (FSR), (4) choice of parton distribution function, (5) choice of Monte Carlo event generator, (6) the top quark mass uncertainty, (7) event detection efficiency combined with the uncertainty on the integrated luminosity. The

[3]This makes the binned likelihood function effectively an un-binned one since resolution effects are about 10 times larger than the bin size.

relative strength of a systematic effect due to the source i is parameterized by the variable δ_i in the likelihood function, constrained to a unit-width Gaussian (last term in Equation 6.3). The $\pm 1\sigma$ changes in the normalization of process j due to the i^{th} source of systematic uncertainty are denoted by $\epsilon_{ji}+$ and $\epsilon_{ji}-$ (see Equation part 6.4). The $\pm 1\sigma$ changes in bin k of the H_T templates for process j due to the i^{th} source of systematic uncertainty are quantified by κ_{jik+} and κ_{jik-} (see Equation part 6.5). $H(\delta_i)$ represents the Heaviside function, defined as $H(\delta_i) = 1$ for $\delta_i > 0$ and $H(\delta_i) = 0$ for $\delta_i < 0$. The Heaviside function is used to separate positive and negative systematic shifts (for which we have different normalization and shape uncertainties). The variable δ_i appears in both the term for the normalization (Equation 6.4) and the shape uncertainty (Equation 6.5), which is how correlations between both effects are taken into account.

6.5.1 Normalization uncertainties

Normalization uncertainties are estimated by recalculating the event detection efficiency using Monte Carlo samples altered due to a specific systematic effect. The normalization uncertainty is the difference between the systematically shifted event detection efficiency and the default event detection efficiency given in Tables 4.5 and 4.6. Table 6.1 summarizes the values obtained for all seven sources of systematic uncertainty. The effect of the uncertainty in the jet energy scale is evaluated by applying jet-energy corrections that describe $\pm 1\sigma$ variations to the default correction factor. For the s-channel, both variations show a lower event detection efficiency (both relative changes are negative). This is an artifact of the $M_{l\nu b}$-window cut. Increasing (decreasing) the jet energy scale factor by the $+1\sigma$ (-1σ) variation, shifts the $M_{l\nu b}$ distribution (shown in Figure 5.5) to higher (lower) values. In both cases, the number of events which fall inside the $M_{l\nu b}$-window is smaller than in the default Monte Carlo sample (for which it was optimized). Systematic uncertainties due to the modeling of ISR and FSR are obtained from dedicated Monte Carlo samples where the strength of ISR/FSR was increased and decreased in the parton

No.	Source	s-channel	t-channel	Combined
1	Jet energy scale	$^{-0.9}_{-1.73}\%$	$^{+1.5}_{-5.6}\%$	$^{+0.7}_{-4.3}\%$
2	ISR	$\pm 0.9\%$	$\pm 1.0\%$	$\pm 1.0\%$
3	FSR	$\pm 5.1\%$	$\pm 1.6\%$	$\pm 2.6\%$
4	PDF	$\pm 2.7\%$	$\pm 4.4\%$	$\pm 3.8\%$
5	Generator	$\pm 2\%$	$\pm 5\%$	$\pm 3\%$
6	Top quark mass	$^{-3.1}_{-0.9}\%$	$^{+0.6}_{-6.1}\%$	$^{-0.7}_{-4.4}\%$
7	$\epsilon_{evt} \oplus$ Luminosity	$\pm 9.8\%$	$\pm 9.8\%$	$\pm 9.8\%$

Table 6.1: Systematic normalization uncertainties ϵ_{ji} for s- and t-channel single top and both processes combined.

No.	Source	$t\bar{t}$	non-top
1	Jet energy scale	$^{-20.3}_{+24.6}\%$	$^{+10.1}_{-12.7}\%$
6	Top quark mass	$\pm 4.4\%$	N/A

Table 6.2: Systematic normalization uncertainties ϵ_{ji} for the $t\bar{t}$ and non-top background.

showering to represent $\pm 1\sigma$ variations [56]. To evaluate the uncertainty associated with the specific choice of parton distribution functions (PDF), we investigate several sensitive choices and selected the PDF that led to the largest deviation (MRST72) [19] from our default set of PDF (CTEQ5L) [18] to represent a $\pm 1\sigma$ variation. We estimate the uncertainty associated with the choice of the Monte Carlo generator using single top Monte Carlo samples generated with the TopREX program [57]. We take half the difference to the default sample to represent a $\pm 1\sigma$ variation.

For the backgrounds, most normalization uncertainties are absorbed into the uncertainty on the predicted number of background events Δ_j. Two major uncertainties are taken separately into account: the uncertainty on the jet energy scale and the top quark mass. The specific values are summarized in Table 6.2.

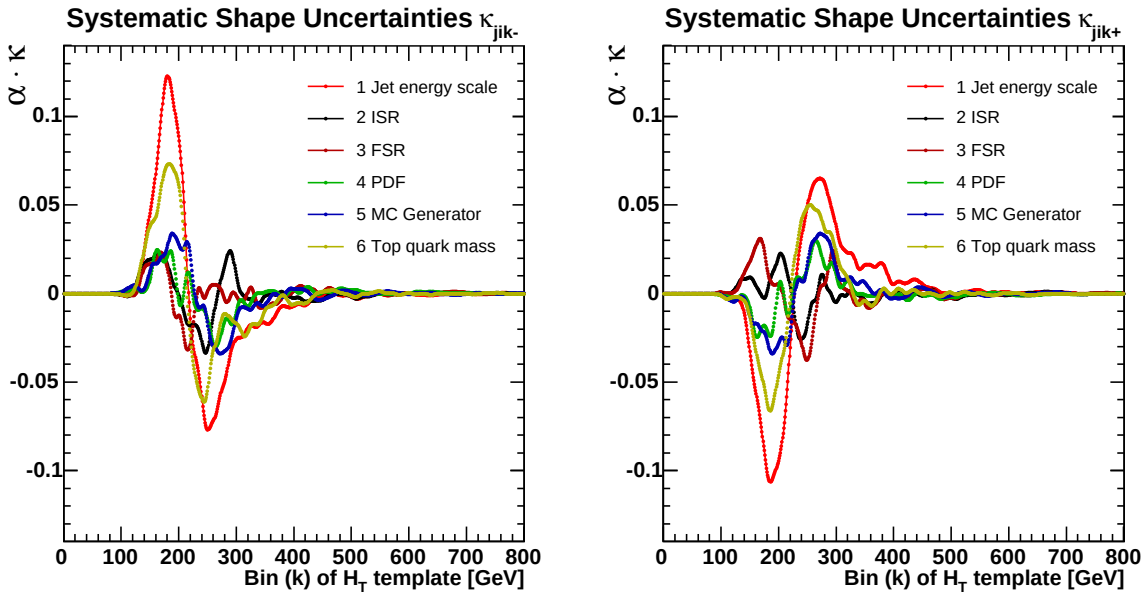

Figure 6.5: Absolute shift of the H_T template histograms ($\alpha \cdot \kappa$) in each bin due to systematic shape uncertainties. The graphs are normalized to the maximum bin content of the default (single top) H_T template.

6.5.2 Shape Uncertainties

The Monte Carlo samples used to determine the systematic normalization uncertainties are also used to produce shifted H_T templates (due to the systematic effects). By comparing the shifted templates to the default likelihood template, we can estimate the systematic shape uncertainty. For each systematic effect, the relative difference of the shifted template to the default template is calculated in each bin (i.e. 1 GeV steps). The values obtained correspond to $\kappa_{jik}+$ and $\kappa_{jik}-$ in the likelihood function (Equation 6.5). Since α_{jk} gives the content of the default H_T template in bin k, the absolute shape difference corresponds to $\alpha \cdot \kappa$. The $\alpha \cdot \kappa$ distributions are shown in Figure 6.5 for all systematic effects. The graphs are normalized to the maximum content of the default H_T template. The left plot shows the -1σ shape variation and the right plot shows the $+1\sigma$ variation. The uncertainty on the jet-energy scale and the top quark mass are the

dominating systematic effects and show shape variations of up to 15% of the maximum template hight. The graphs pass through zero at the maximum of the default single top template ($H_T = 213$ GeV), since this is where the absolute difference changes sign.

For the non-top background, we take an additional source of systematic error into account: the choice of the factorization scale of the W+jets background. The default Monte Carlo samples use a variable factorization scale $Q^2 = M_W^2 + \sum p_T^2$, and we also investigate a constant scale $Q^2 = M_W^2$. The shape uncertainty on the background templates are shown in Appendix B.

6.5.3 Marginalizing the Likelihood

The likelihood function depends on many parameters: the signal and background cross sections, the uncertainty on the background normalization and the parameters of the systematic uncertainties. Since we are only interested in the parameter β_1, which corresponds to the single top cross section normalization ($\beta_1 = \sigma_1/\sigma_{SM}$), we treat all other parameters in the likelihood as nuisance parameters and we can remove their dependence by integrating over them [6, 54]. The integration yields the marginalized likelihood which only depends on the single top parameter β_1. The marginalized Likelihood is defined as:

$$\mathcal{L}^*(\beta_1) = \int_0^{+\infty} \mathcal{L}(\beta_1, \beta_2, \beta_3; \delta_1, ..., \delta_7)\ d\beta_2 d\beta_3 d\delta_1 ... d\delta_7$$

The integration is performed using a Monte Carlo integration technique developed by Catalin Ciobanu [55]. For each MC integration point, a random number for the nuisance parameters β_j and δ_i is generated according to the Gaussian prior distributions $G(\beta_j, 1, \Delta_j)$ and $G(\delta_j, 0, 1)$.

In Bayesian statistics, all knowledge about β_1 is summarized by the posterior probability distribution function (p.d.f.), $p(\beta_1|data)$, which gives the degree of belief for β_1 to take on values in a certain region, given the data. The posterior p.d.f is obtained by

using Bayes' theorem:

$$p(\beta_1|data) = \frac{\mathcal{L}^*(data|\beta_1)\pi(\beta_1)}{\int \mathcal{L}^*(data|\beta_1')\pi(\beta_1')d\beta_1'}$$

where $\mathcal{L}^*(data|\beta_1)$ is the marginalized likelihood and $\pi(\beta_1)$ is the prior p.d.f. for β_1. The denominator simply normalizes the posterior p.d.f. to unity. We assume no knowledge about the single top production cross section, thus a flat prior, $\pi(\beta_1) = H(\beta_1)$, is used in this analysis.

6.5.4 Setting an Upper Limit on the Production Cross Section

In Section 6.4 we performed pseudo-experiments with fake datasets that we would expect from performing many CDF experiments. The statistical uncertainty on the single top parameter β_1 (middle plot on the top of Figure 6.4) was, on average, on the order of 170 %. Assuming the Standard Model is the correct description of Nature, we do not have the statistical power to measure a significant single top signal with this dataset which we would call evidence or observation of single top quark production. Instead, we can use the likelihood method to set an upper limit on the production cross section. If, however, Physics beyond the Standard Model would significantly alter the single top production rate, the data would show a significant deviation from the expectation[4].

To set an upper limit on the single top quark production cross section at the 95% Confidence Level, we integrate the posterior p.d.f. up to the limit β_1^{95} to cover 95% of the posterior p.d.f.

$$0.95 = \int_0^{\beta_1^{95}} p(\beta_1|data)d\beta_1$$

[4]I.e. the likelihood method applied to the data would return a value of β_1 significantly different from the expectation of 1.0.

6.5.5 *A Priori* Sensitivity

Before applying the likelihood method to data, we estimate *a priori* the sensitivity of the likelihood method by measuring what cross section limit we are expecting to be able to set in data. We apply the maximum likelihood method to pseudo-experiments which tests the real measurement. For each pseudo-experiment the *a priori* upper limit at 95

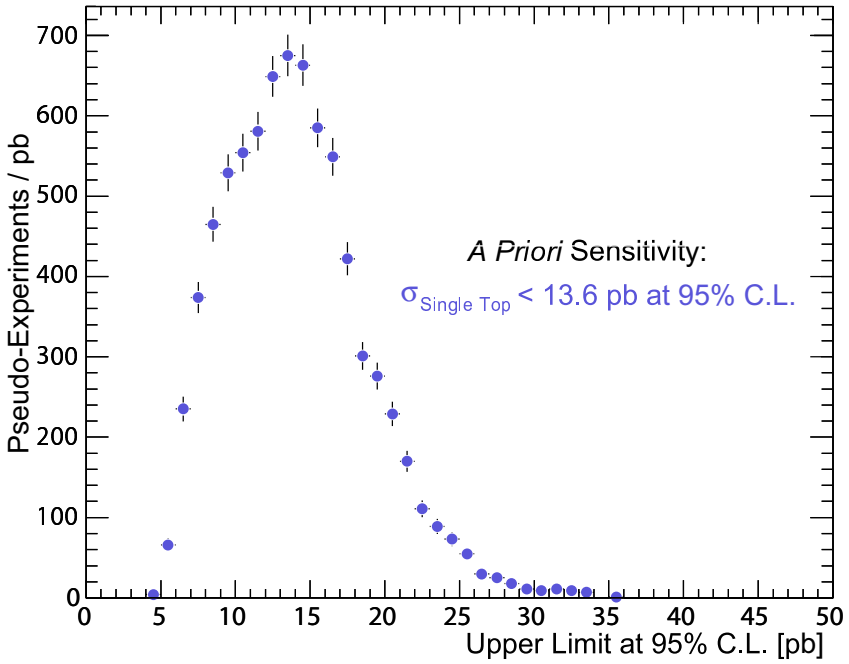

Figure 6.6: Distribution of *a-priori* upper limits at 95 % C.L. on the combined single top quark production cross section determined from pseudo-experiments.

% C.L. on the combined single top quark production cross section is calculated. Figure 6.6 shows the distribution obtained from 7000 pseudo-experiments. We take the median of this distribution as a measure of the *a-priori* sensitivity and find a value of 13.6 pb (12.4 pb statistical only), roughly 4.6 times larger than the Standard Model cross section prediction.

Chapter 7

Results from Data

We apply now the event selection summarized in Chapter 4 and the likelihood method described in Chapter 6 to data. Table 7.1 summarizes the predicted number of single top and background events. In total, we expect 38.1 ± 5.9 events to pass our event selection in approximately 162 pb^{-1} of CDF Run II data and we observe 42 events. This is in good agreement with the prediction, given the uncertainty. The event yield in data after applying (sequentially) all event selection criteria is summarized in Appendix C. We

	N events
s-channel ($\sigma_s = 0.88 \pm 0.11$ pb)	1.5 ± 0.2
t-channel ($\sigma_t = 1.98 \pm 0.26$ pb)	2.8 ± 0.5
$t\bar{t}$ ($\sigma_{t\bar{t}} = 6.7^{+0.71}_{-0.88}$ pb)	3.8 ± 0.9
non-top	30.0 ± 5.8
Sum	38.1 ± 5.9
Observed	**42**

Table 7.1: Predicted number of signal and background events after all event selection requirements in 162 ± 10 pb^{-1} of CDF data, compared with the observation in data.

compare the H_T distribution of the 42 data events with the sum of predicted single top

and background H_T shapes in Figure 7.1. Again, we find good agreement between data and prediction.

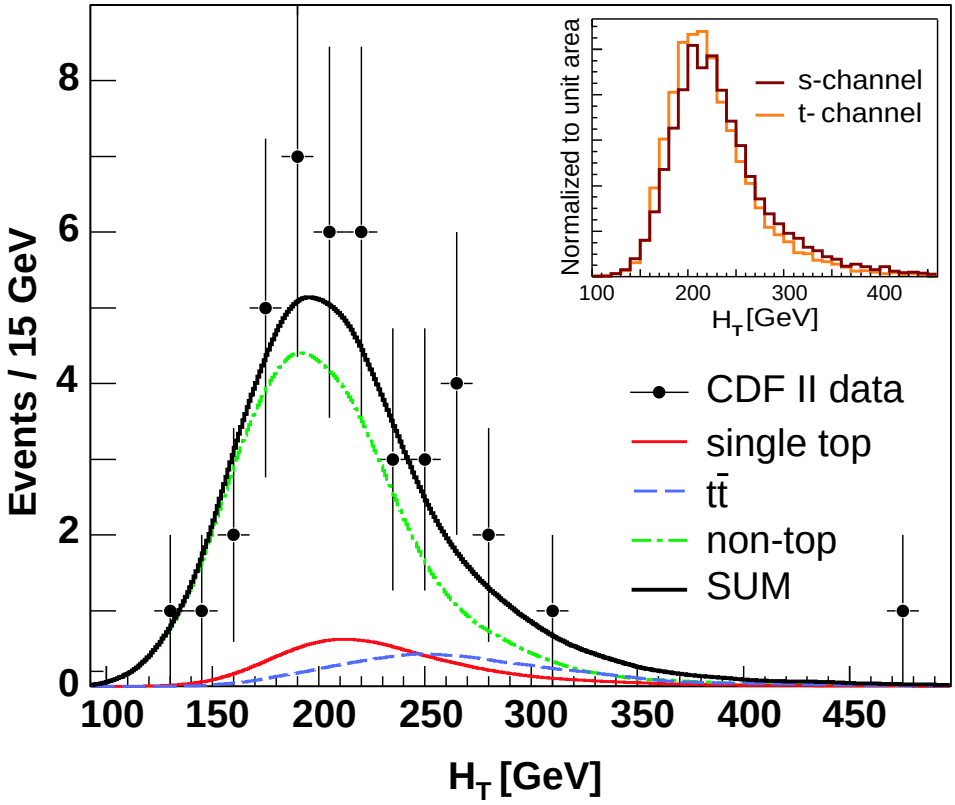

Figure 7.1: H_T distribution for data (42 events) compared with smoothed predictions for signal and background. The inset shows the H_T distribution for both contributing single top quark production channels.

One event contributes at high $H_T \simeq 475$ GeV with very little probability to be either single top or background. We show details about this special event in Section 7.2.

7.1 Upper Limit at 95% Confidence Level

Finally, we apply the likelihood method to the data in order to extract the most probable single top content in the data sample. The posterior probability density obtained by marginalizing the likelihood and multiplying with a flat *prior* is shown in Figure 7.2.

The most probable value (MPV) corresponds to the most likely combined single top

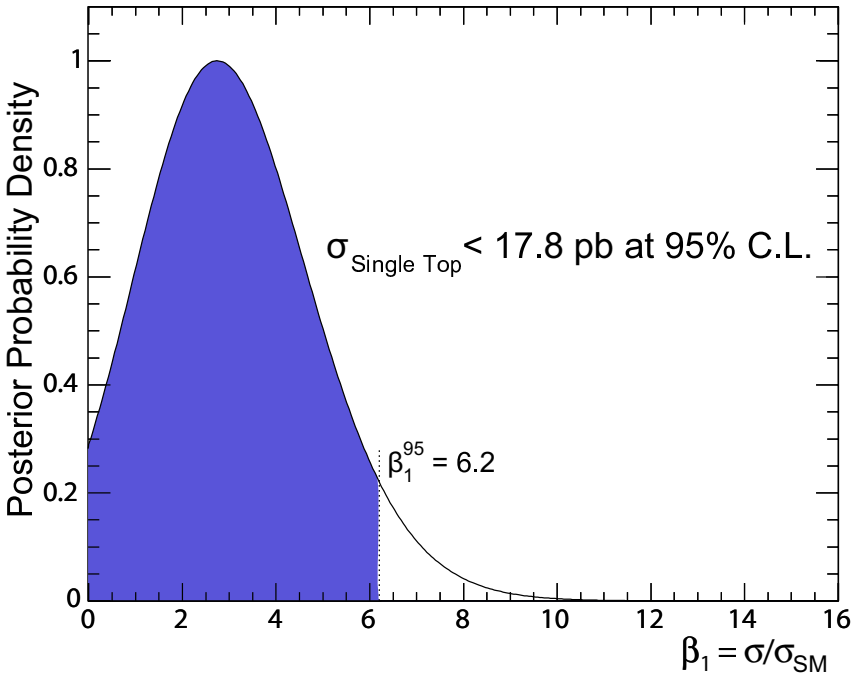

Figure 7.2: Posterior probability distribution function, $p(\beta_1)$, obtained by applying the likelihood method to data.

production cross section given the data. The MPV is obtained at $7.7^{+5.1}_{-4.9}$ pb. The uncertainty corresponds to the range of highest posterior probability density which covers 68.4% [6]. Since this uncertainty is rather large, we extract the upper limit on the production cross section at the 95% C.L. We integrate the posterior probability density to cover 95% of the area and find $\sigma_{single\ top} < 17.8$ pb at 95% C. L. [58].

7.2 Special Event at High H_T

One event in the data has very high $H_T \simeq 475$ GeV. This seems very unlikely, given the Standard Model prediction for single top, non-top and $t\bar{t}$. In this context, the observation of events with low probability is interesting, because it could indicate the presence of new physics beyond the Standard Model. In this Section, we will summarize the kinematic

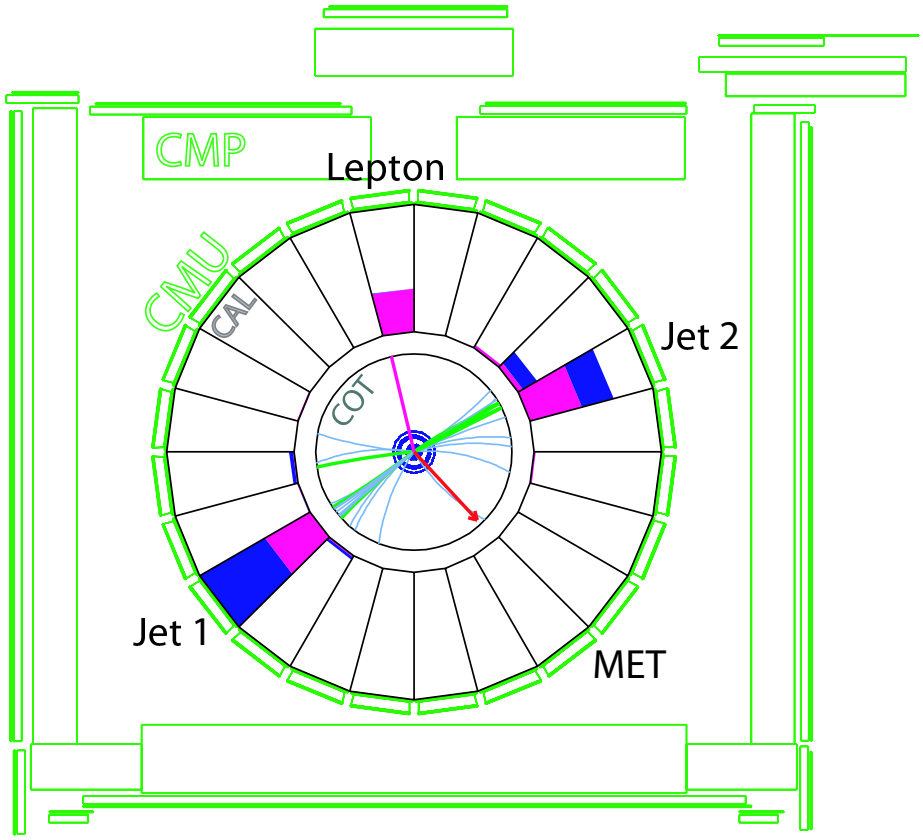

Figure 7.3: Front end view of the CDF detector for the highest H_T event.

properties of this event and calculate the probability that a Standard Model process is the origin of this event. We end this Section with the conclusion that in an ensemble of $\simeq 38$ events, there is a reasonably large probability that one of the Standard Model processes is the origin of this event.

In Figure 7.3, the event is shown in the CDF event display showing the tracking and calorimeter as well as the muon system. The lighter color in the calorimeter towers represents energy deposited in the EM calorimeter, the darker color represents energy deposited in the HAD calorimeter. The lepton (electron in this case) may be distinguished from the two energetic jets since it deposits only very little energy in the HAD calorimeter. The arrow points towards the direction of $\not\!\!E_T$. Figure 7.4 shows the transverse energy deposition in the calorimeter in a 'lego plot'. The two highest energy jets and the lepton are clearly visible. Both jets feature a significant displaced secondary vertex and

Object	E_T	η	ϕ
Lepton (e^-)	50.9 ± 1.5 GeV	0.24 ± 0.004	1.81 ± 0.0002
$\not\!\!E_T$	25.7 ± 11.0 GeV	N/A	5.61 ± 0.18
Jet 1	213.1 ± 6.5 GeV	0.45 ± 0.02	3.80 ± 0.03
Jet 2	185.1 ± 7.7 GeV	-0.13 ± 0.04	0.53 ± 0.05
H_T	474.7 ± 17.1 GeV		
$M_{b\bar{b}}$	411.3 ± 13.9 GeV/c^2		
$M_{l\nu b}$	172.9 ± 7.7 GeV/c^2		
$M_{l\nu\bar{b}}$	249.2 ± 2.9 GeV/c^2		
$M_{l\nu b\bar{b}}$	504.5 ± 11.6 GeV/c^2		

Table 7.2: Kinematic properties of the highest H_T event.

have been b-tagged by the SecVtx algorithm. Table 7.2 summarizes several kinematic quantities of the event. It should be noted that even though the event has very high H_T and a very high di-jet mass, the invariant mass of the lepton, neutrino and b-jet (b-jet with the highest $Q_{lepton} \cdot \eta_{b-jet}$ which is more likely the b-jet from the top quark decay) $M_{l\nu b}$=172.9 GeV/c^2 is very close to the top quark mass. The invariant mass of the entire final state, $M_{l\nu b\bar{b}}$=504.5 GeV, is very large. A possible non Standard Model candidate for this kind of signature would be a heavy W' boson, with $W' \to t\bar{b}$ [59].

In order to calculate the probability that any Standard Model process (single top, $t\bar{t}$ or non-top) produced the event, we can make use of the template distributions shown in Figure 7.1. The area underneath the sum of the template distributions from 450 GeV-∞ corresponds to the probability of observing an event greater 450 GeV. This probability amounts to about 0.44%. Given that our predicted number of events in data was 38.1, we can estimate,*a priori*, the probability of observing one event with $H_T \geq 450$ GeV with the CDF experiment, (i.e. $P_{exp}(\textit{one event with } H_T > 450) \simeq N \cdot P_{evt}(H_T > 450) = 38.1 \cdot 0.44 = 16.8\%$). We arrive at the same answer by performing pseudo-experiments and

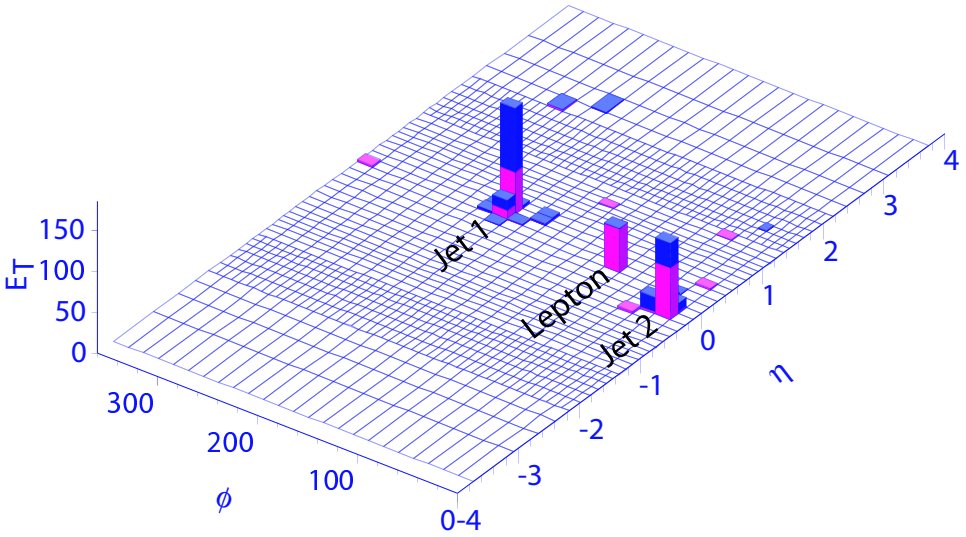

Figure 7.4: Lego plot of transverse energies in the CDF calorimeter for the highest H_T event.

counting the fraction of pseudo-experiments that have at least one event with $H_T > 450$. In 100 000 pseudo-experiments, we find 16 577 experiments with at least one event with $H_T > 450$ (16.8%); 1253 experiments had at least two events with $H_T > 450$ (1.5%). In summary, there is a reasonably large probability that this event originates from a Standard Model process. Statistically, we expect (on average) that about one in seven CDF experiments (with 162 pb^{-1} of data) will feature an event with $H_T > 450$ GeV; if we were to observe two events, this probability would only be one in 67. In neither case we would use this as evidence for new physics.

Chapter 8

Outlook:

Improving the Sensitivity of the Search for Single Top

This chapter describes a new analysis technique that makes optimal use of information in the data. Since single top quark production suffers from a large number of background processes, using more information about each event improves our ability to discriminate single top against the background. The implementation of the new analysis method is similar to a recently optimized measurement of the top quark mass in $t\bar{t}$ lepton+jets events (events where one W boson decays leptonically and the other W boson decays into quarks). Using this technique doubled the statistical sensitivity of the analysis [60]. The strategy is related to a method previously used for the measurement of the mass and the cross section of $t\bar{t}$ in dilepton events (events where both W bosons decay leptonically) [61, 62].

8.1 Introduction

The new method relies on a comparison of event probabilities for signal and background processes based on the Standard Model differential cross-section calculation.

The data for the analysis described in Chapter 6 and 7 was of the form of measured values of the kinematic variable H_T for each observed event. The shape of the H_T templates used in the likelihood method corresponds to the shape of the differential cross-section distributions $d\sigma/dH_T$ for signal and background. An improved discrimination between signal and background processes could be achieved by including the shapes of all differential cross sections in the analysis. This can be achieved by calculating the fully differential cross section on an event-by-event basis for the signal hypothesis, and the background hypothesis to quantify how likely the event is to be either signal or background. The differential cross-section is given by [6]:

$$d\sigma = \frac{(2\pi)^4 |M|^2}{4\sqrt{(q_1 \cdot q_2)^2 - m_{q_1}^2 m_{q_2}^2}} \, d\Phi_n(q_1 + q_2; p_1, .., p_n) \tag{8.1}$$

where $|M|$ is the Lorentz invariant matrix element; q_1, q_2 and m_{q_1}, m_{q_2} are the four momenta and masses of the incident particles; and $d\Phi_n$ is the n-body phase space given by [6]:

$$d\Phi_n(q_1 + q_2; p_1, .., p_n) = \delta^4(q_1 + q_2 - \sum_{i=1}^{n} p_i) \prod_{i=1}^{n} \frac{d^3 p_i}{(2\pi)^3 2E_i} \tag{8.2}$$

If the CDF detector would be 'ideal', and if we could measure all four momenta of the initial and final state particles very precisely, we could use this formula without modification and normalize it to the total cross section to define the event probability:

$$P_{evt} \sim \frac{d\sigma}{\sigma}$$

However, several effects have to be considered: (1) the initial state interaction is initiated by partons inside the proton and antiproton, (2) neutrinos in the final state are not identified directly, and (3) the resolution of the detector can not be ignored. To address the first point, the differential cross section is folded over the parton distribution functions.

To address the second and third points, we integrate over all particle momenta which we do not measure (e.g. p_z of the neutrino), or do not measure very well, due to resolution effects (e.g. jet energies). The integration reflects the fact that we want to sum over all possible particle variables (y) leading to the observed set of variables (x) measured with the CDF detector. The transfer between the particle variables (y) and the measured variables (x) is established with the transfer function, $W(y,x)$. After incorporating the effects mentioned above, the event probability takes the form:

$$P(x) = \frac{1}{\sigma}\int d\sigma(y) dq_1 dq_2 f(x_1) f(x_2) W(y,x) \tag{8.3}$$

where $d\sigma(y)$ is the differential cross section in terms of the particle variables; $f(x_i)$ are the PDFs, with x_i being the fraction of the proton momentum carried by the parton ($x_i = E_{q_i}/E_{beam}$); and $W(y,x)$ is the transfer function. Substituting Equation 8.1 and 8.2 into Equation 8.3, and considering a final state with four particles (n=4), the event probability becomes:

$$P(x) = \frac{1}{\sigma}\int 2\pi^4 |M|^2 \frac{f(x_1)}{|E_{q_1}|}\frac{f(x_2)}{|E_{q_2}|} W(y,x) d\Phi_4 dE_{q_1} dE_{q_2} \tag{8.4}$$

where the masses and transverse momenta of the initial partons are neglected (i.e. $\sqrt{(q_1 \cdot q_2)^2 - m_{q_1}^2 m_{q_2}^2} \simeq 2E_{q_1}E_{q_2}$). In Section 8.2, we will derive the transfer function and make certain assumptions on the mapping between particles and measured objects. In Section 8.3 we will apply the event probability of Equation 8.4 to single top events.

8.2 Transfer Function

The transfer function, $W(y,x)$, provides the probability of measuring the set of observable variables (x) that correspond to the set of production variables (y). The set (y) represents all final state particle momenta at the particle level, while the set (x) represents the measured momenta (of the corresponding object) with the CDF detector. In the case of well-measured objects, $W(y,x)$ is taken as a δ-function (i.e. the measured momenta

are used in the differential cross section calculation without any transfer). When the detector resolution cannot be ignored, $W(y,x)$ is taken as a Gaussian-type function. For unmeasured quantities, like the momenta of the neutrino, the transfer function is unity (the transverse momenta of the neutrino, however, can be inferred from energy and momentum conservation).

Lepton momenta are well-measured with the CDF detector and we will assume δ-functions for them (first factor of Equation 8.5). The jet angular resolution of the calorimeter is also good (on the order of $\sigma_{\Delta_R} \simeq 0.07$) and we assume δ-functions for the transfer function of the jet directions (second factor of Equation 8.5). The resolution of the measured jet energies, however, is not negligible and the transfer function is derived in Section 8.2.1. Using these assumptions, $W(y,x)$ takes the following form for the four particle final state we consider in the single top search (lepton, neutrino and two jets):

$$W(y,x) = \delta^3(\vec{p_l}^{\,y} - \vec{p_l}^{\,x}) \prod_{i=1}^{2} \delta^2(\Omega_i^y - \Omega_i^x) \prod_{j=1}^{2} W_{jet}(E_{parton_j}, E_{jet_j}) \tag{8.5}$$

where $\vec{p_l}^{\,y}$ and $\vec{p_l}^{\,x}$ are the produced and measured lepton momenta, Ω_i^y and Ω_i^x are the produced quark and measured jet angles, and E_{parton_j} and E_{jet_j} are the produced quark and measured jet energies.

8.2.1 Jet-Parton Transfer

The transfer between parton and jet energies is determined by the transfer function $W_{jet}(E_{parton}, E_{jet})$. The standard jet energy corrections introduced in Section 4.4.1 correct the energies of jets in a way that the means of the corrected jet energies and the original parton energies are equal. Such corrections, however, do not account for the shape of the difference in energies: the shape of the $\delta_E = (E_{parton} - E_{jet})$ distribution). This distribution is asymmetric and features a significant tail at positive δ_E, as shown in Figure 8.1. Consequently, standard jet corrections, which assume Gaussian resolution, often underestimate the original parton energy.

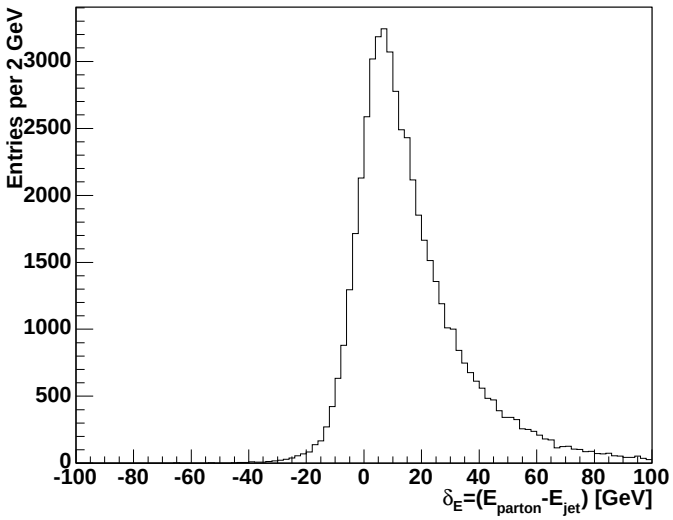

Figure 8.1: Distribution of $\delta_E = (E_{parton} - E_{jet})$ for matched jets to partons in s-channel Monte Carlo events (passed through full detector simulation).

We parameterize the δ_E distribution as a sum of two Gaussian functions: one to account for the sharp peak and one to account for the asymmetric tail:

$$W_{jet}(E_{parton}, E_{jet}) = \frac{1}{\sqrt{2\pi}(p_2 + p_3 p_5)}(exp\frac{-(\delta_E - p_1)^2}{2p_2^2} + p_3\ exp\frac{-(\delta_E - p_4)^2}{2p_5^2}) \qquad (8.6)$$

where the parameters p_i have a linear dependence on E_{parton}, i.e.

$$p_i = a_i + b_i E_{parton}$$

A total of 10 parameters $(a_1, b_1, .., a_5, b_5)$ are therefore required to specify $W_{jet}(E_{parton}, E_{jet})$.

Parameters for $W_{jet}(E_{parton}, E_{jet})$

We determine the parameters of the transfer function $W_{jet}(E_{parton}, E_{jet})$ using the s-channel Monte Carlo sample. We apply all event selection requirements outlined in Chapter 4, except for the $M_{l\nu b}$-window. We then select jets which were reconstructed in the same direction as the original particle (b or $\bar{b}$ quark for s-channel single top). We require the b quark to be within a cone of $\Delta R < 0.4$ around the reconstructed jet-axis

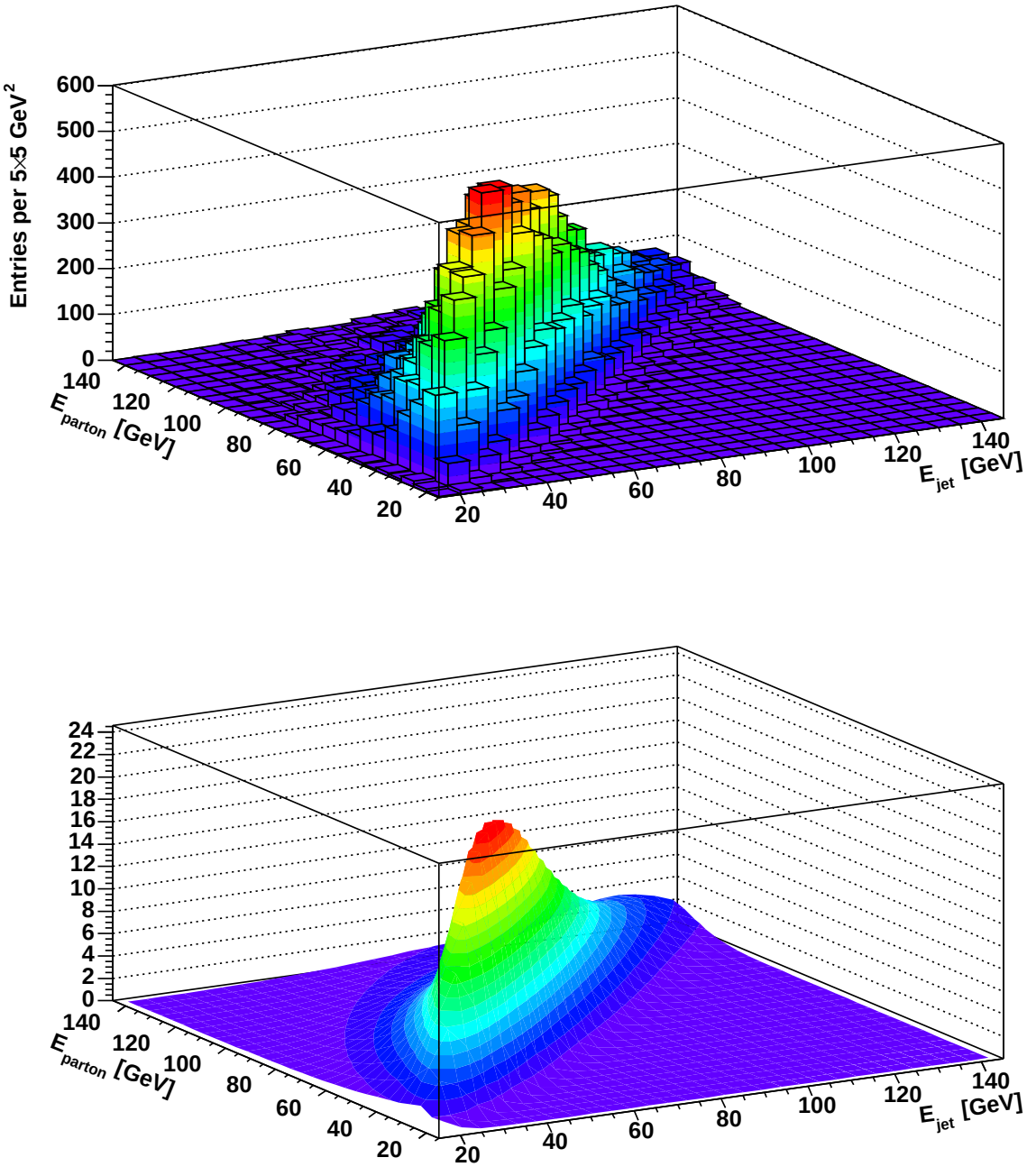

Figure 8.2: TOP: Lego plot of E_{parton} vs E_{jet} (passed through full GEANT detector simulation) for a sample of matched jets to partons in s-channel single top Monte Carlo events. BOTTOM: Functional form of E_{parton} vs E_{jet}, where E_{jet} is predicted using the transfer function $W_{jet}(E_{parton}, E_{jet})$ of Equation 8.6 and the particle density $n(E_{parton})$.

in order to be considered 'matched'. We correct the matched jet using jet-correction level 5 and write out the jet energy together with the energy of the original particle. The distribution of measured jet energies versus the original parton energy of the b quark is shown in the upper plot of Figure 8.2. The parameters of the transfer function are then derived by performing a maximum likelihood fit to these events.

If $\mathrm{n}(E_{jet}, E_{parton})dE_{jet}dE_{parton}$ is the number of jets with jet energies between E_{jet} and $E_{jet} + dE_{jet}$, and particle energies between E_{parton} and $E_{parton} + dE_{parton}$ in this sample, then:

$$n(E_{jet}, E_{parton})dE_{jet}dE_{parton} = n(E_{parton})dE_{parton}W_{jet}(E_{parton}, E_{jet})dE_{jet} \tag{8.7}$$

where $n(E_{parton})dE_{parton}$ is the number of particles with an energy between E_{parton} and $E_{parton} + dE_{parton}$. The parameters of $W_{jet}(E_{parton}, E_{jet})$ are determined using a method developed by Florencia Canelli such to maximize the agreement in Equation 8.7 [63]. The values obtained are summarized in Table 8.1.

$p_i = a_i + b_i E_{parton}$	a_i	b_i
p_1 [GeV]	-1.380	-0.069
p_2 [GeV]	1.955	0.079
p_3 [N/A]	0.498	0.000
p_4 [GeV]	5.702	-0.319
p_5 [GeV]	1.319	0.179

Table 8.1: Parameters for $W_{jet}(E_{parton}, E_{jet})$ for s-channel single top Monte Carlo events (jets matched to particles).

The parametrization is shown in Figure 8.2. The upper plot shows the two dimensional distribution of E_{parton} vs E_{jet} obtained from the Monte Carlo sample, while the bottom plot shows the prediction of this shape in a functional contour plot using the transfer function and the particle density $n(E_{parton})$. The performance of the parametrization is

best shown in Figure 8.3, which shows the $\delta E = (E_{parton} - E_{jet})$ distribution (histogram) compared to the prediction from the transfer function (solid line).

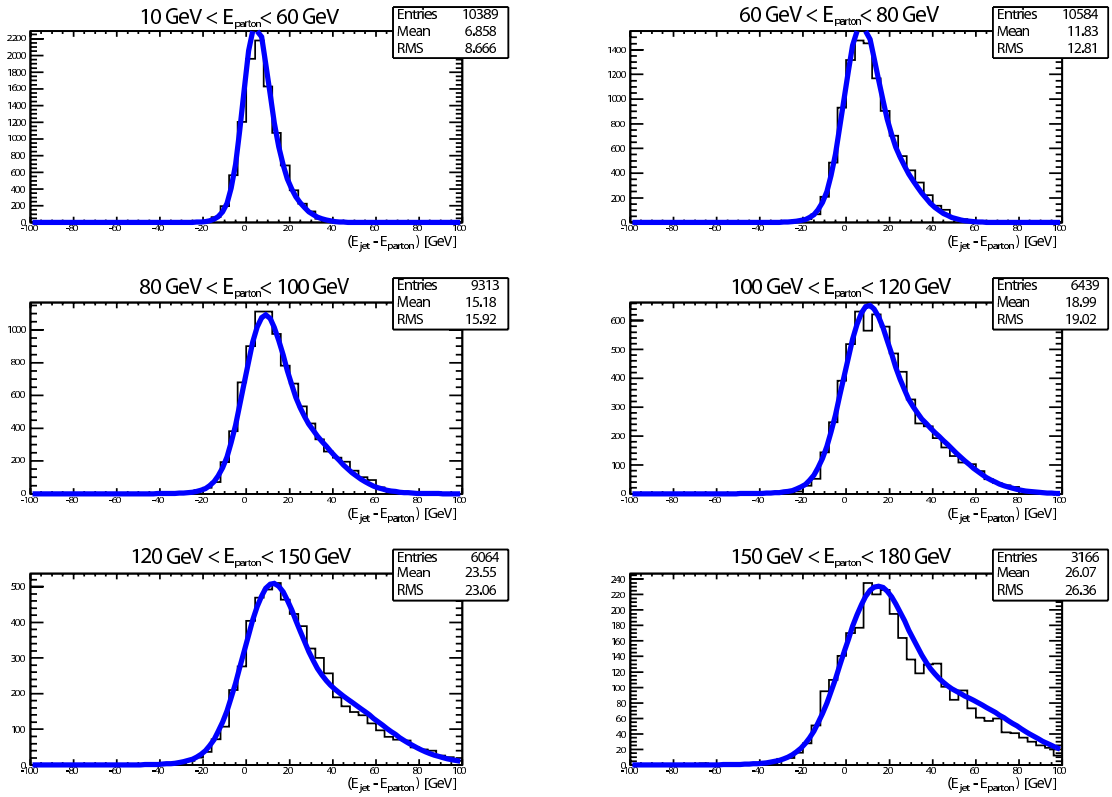

Figure 8.3: Distributions of $\delta E = (E_{parton} - E_{jet})$ for different ranges of parton energy of matched jets to partons. The histograms are (s-channel) single top Monte Carlo events after full GEANT detector simulation and jet (level 5) corrections. The solid line corresponds to the transfer function using the parameters of Table 8.1.

8.3 Event Probability

After specifying the transfer function, we can apply the general event probability of Equation 8.4 to the case of the single top analysis.

8.3.1 Matrix Element

We calculate the matrix element ($|M|$) for the event probability at leading order perturbation theory by using the HELAS (HELicity Amplitude Subroutines for Feynman Diagram Evaluations) package [64]. The correct subroutine calls for a given process are automatically generated by the MadGraph program [65]. Figure 8.4 shows the two diagrams we calculated with HELAS used in the Monte Carlo study described in Section 8.4.

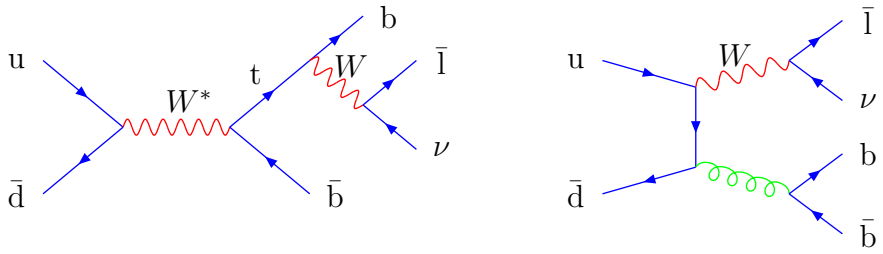

Figure 8.4: Leading order Feynman diagram for s-channel single top quark production and decay (left) and $Wb\bar{b}$ background (right).

8.3.2 Phase Space

The integration of the differential cross section has to be performed over 14 variables corresponding to the momentum vectors of the four final state particles (12 variables) and the longitudinal momenta of the initial state partons (2 variables). There are 11 δ-functions inside the integrals: four for total energy and momentum conservation (part of the phase space factor, see Equation 8.2) and seven for the transfer function (three for the lepton momentum vector and four for the jet angles, see Equation 8.5). The calculation of the event probability therefore involves a three dimensional integration. The integration is performed numerically over the absolute value of the quark momenta ($\rho_i = |\vec{p}_i|$) and the longitudinal momentum of the neutrino ($p_{\nu,z}$). Since the value of

the matrix element is negligible, except near the Breit-Wigner pole of the W boson, we change the integration variable $p_{\nu,z}$ to the W-mass. The phase space for single top events is derived in Appendix D and has been expressed as a function of the variables $(\rho_1, \Omega_1, \rho_2, \Omega_2, \vec{p}_l, m_W^2)$. The result is:

$$\begin{aligned} d\Phi_4 &= \delta(E_{q_1} + E_{q_2} - \sum_{i=1}^{4} E_i)\ \delta(p_{q_1,z} + p_{q_2,z} - \sum_{i=1}^{4} p_{i,z}) \\ &\times \frac{dm_W^2}{|2E_l\frac{p_{\nu,z}}{E_\nu} - 2p_{\nu,z}|} \frac{d^3\vec{p}_l}{(2\pi)^3 2E_l} \frac{1}{(2\pi)^3 2E_\nu} \prod_{i=1}^{2} \frac{\rho_i^2 d\rho_i d\Omega_i}{(2\pi)^3 2E_i} \end{aligned} \tag{8.8}$$

8.3.3 Event Probability for Single Top Events

Substituting the phase space factor (Equation 8.8) and the transfer function (Equation 8.5) into the expression for the event probability (Equation 8.4), we obtain:

$$\begin{aligned} P(x) = \frac{1}{\sigma} \int 2\pi^4 |M|^2 \frac{f(x_1)}{|E_{q_1}|} \frac{f(x_2)}{|E_{q_2}|} \delta^3(\vec{p}_l{}^y - \vec{p}_l{}^x) \prod_{i=1}^{2} \delta^2(\Omega_i^y - \Omega_i^x) \prod_{j=1}^{2} W_{jet}(E_{jet}, E_{parton}) \Phi_4 \\ \times \delta(E_{q_1} + E_{q_2} - \sum_{i=1}^{4} E_i) \delta(p_{q_1,z} + p_{q_2,z} - \sum_{i=1}^{4} p_{i,z}) d^3\vec{p}_l dm_W^2 dE_{q_1} dE_{q_2} \prod_{i=1}^{2} d\rho_i d\Omega_i \end{aligned} \tag{8.9}$$

where,

$$\Phi_4 = \frac{2\pi^4}{(2\pi)^9} \frac{1}{2E_l} \frac{1}{2E_\nu} \frac{\rho_1^2}{2E_1} \frac{\rho_2^2}{2E_2} \frac{1}{|2E_l\frac{p_{\nu,z}}{E_\nu} - 2p_{l,z}|}$$

The integration over E_{q_1} and E_{q_2} eliminates the two δ-functions in the second line of Equation 8.9. The integration over the lepton momenta and the quark solid angles eliminate the δ-functions in the first line of Equation 8.9 associated with $W(y, x)$. The final event probability takes the form:

$$P(x) = \frac{1}{\sigma} \int d\rho_1 d\rho_2 dm_W^2 \sum_{comb,\nu} |M|^2 \frac{f(q_1)}{|q_1|} \frac{f(q_2)}{|q_2|} \Phi_4 \prod_{i=1}^{2} W_{jet}(E_{parton,i}, E_{jet,i}) \tag{8.10}$$

Because we do not know which one of the two jets came from the top quark decay, we have to calculate the probability for both possible jet-parton assignments. The total probability is summed over both combinations. We also obtain two solutions for the $p_{\nu,z}$ for each integration step over m_W (according to Equation 4.3) and the probability is summed over both solutions.

In summary, the event probability makes use of all measured quantities[1] to specify each event. This should provide good discrimination between signal and background. It uses both possible jet combinations in the event so that the right jet-parton association is always included. The expression for the event probability of Equation 8.10 can be applied to the s-channel and t-channel single top process as well as to the major backgrounds in the analysis, namely $Wb\bar{b}$, $Wc\bar{c}$ and Wc. Only the matrix element has to be changed to represent the desired process. The event probability for the $t\bar{t}$ background, however, requires a new definition, because the process features six final state particles.

8.4 Study with Smeared Monte Carlo Events

In this section we study the discriminating power of the event probabilities in the search for single top. To simplify the analysis we only distinguish two processes: s-channel single top (representing the signal) and $Wb\bar{b}$ (representing all background processes). We generate 25,000 events for each process (at particle level with no detector simulation). We use the transfer function $W_{jet}(E_{jet}, E_{parton})$ as a 'fast jet simulation' to smear the energies of the partons (quarks). This is possible since $W_{jets}(E_{parton}, E_{jet})$ models the combined effects of radiation, hadronization, jet resolution and jet reconstruction. The smearing is performed by randomly generating E_{jet} according to the double Gaussian distribution of $W_{jet}(E_{parton}, E_{jet})$ given the particular value of E_{parton} in the event. Using 'smeared Monte Carlo events' has the advantage that we can easily produce large sample of signal and background events and we do not have to worry about detector effects which may bias the outcome of the study.

We apply similar kinematic event selection requirements to the smeared events as discussed in the event selection of the H_T analysis (except the $M_{l\nu b}$-window). Table 8.2 summarizes the selection requirements.

[1]The only exception is the unclustered energy, which refers to the energy deposited in the calorimeter from all sources except from leptons and jets.

Lepton:	$E_T > 20$ GeV	$\eta < 1.0$
Neutrino:	$E_T > 20$ GeV	N/A
Jets:	$E_T > 15$ GeV	$\eta < 2.8$

Table 8.2: Event selection requirements for simple study with smeared Monte Carlo events.

For each event that passes the event selection we compute the event probability for signal P_s and background P_b. $P_s(x)$ and $P_b(x)$ are both calculated according to Equation 8.10, the only difference between the two calculations is the expression for the matrix element. The values obtained on an event-by-event basis are visualized in a two dimensional scattered plot shown in Figure 8.5. Each event (point) in the two-dimensional plot has a signal probability and an associated background probability. The region with highest signal density (red) is clearly visible and is separated from the background (blue).

We define an event probability discriminant as EPD= P_s/P_b to better show the separation between signal and background. Figure 8.6 shows the distribution of the discriminant for signal and background events. The scale of the x-axis is arbitrary. We can now compare the separation of the EPD-distributions to, for example, the H_T-distributions for the smeared signal and background events. We calculate H_T according the definition of Equation 6.1 (without the normalization) except that here, we only sum over jets with $E_T > 15$ GeV. To quantify the improved statistical sensitivity of the analysis using the event probabilities, we apply the likelihood method introduced in Chapter 6 to the smeared Monte Carlo events and perform pseudo experiments. For simplicity, we do not include sources of systematic uncertainties into the likelihood and we use a similar expression to Equation 6.2 for the Likelihood function:

$$\mathcal{L}(\beta_1, \beta_2) = \frac{e^{-n} n^N}{N!} \prod_{k=1}^{N} \frac{\beta_1 F_1(V_i) + \beta_2 F_2(V_i)}{n} G(\beta_2 | 1, \Delta_2) \tag{8.11}$$

- $\beta_j = n_j / \mathrm{N_j^{pred}} = \sigma_j / \sigma_{SM_j}$: Free parameter for process j;
  j=1 for single top (s-channel), j=2 for background ($Wb\bar{b}$)

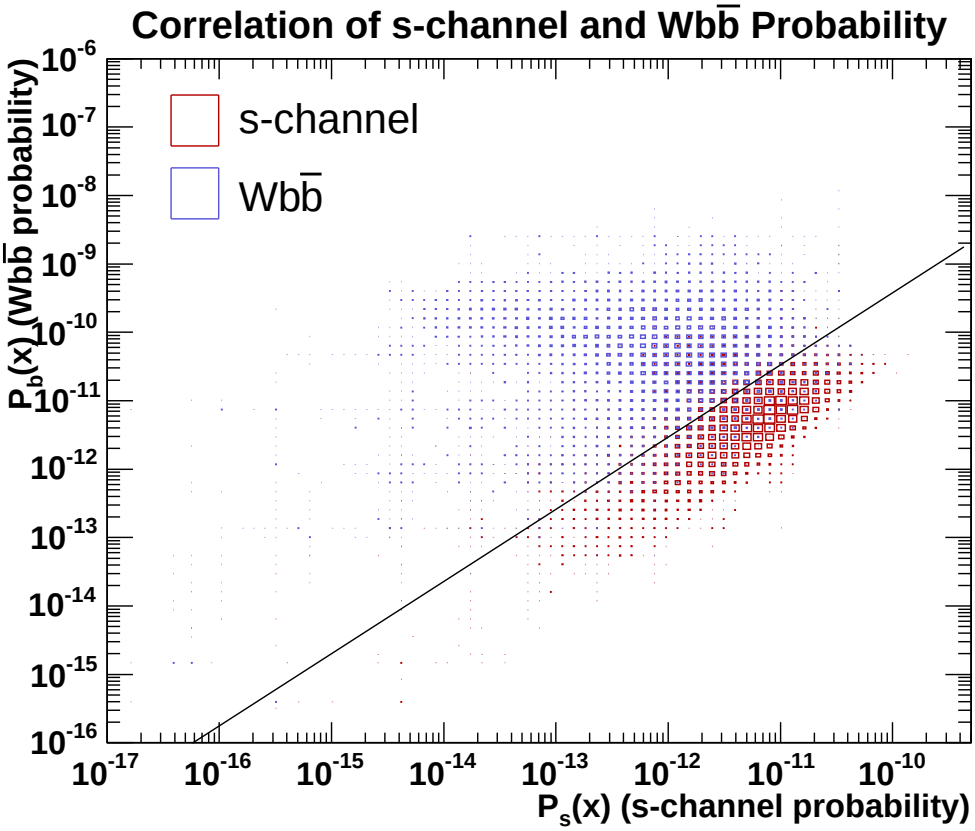

Figure 8.5: Correlation of s-channel event probability and $Wb\bar{b}$ probability for smeared Monte Carlo events. The sizes of the boxes are proportional to the density of points at each position.

- $\mathrm{N_j^{pred}}$: Predicted number of events for process j
- $n = \sum_{j=1}^{2} \beta_j N_j$: Most likely sum of signal and background Poisson means
- $F_j(V)$: Template for process j, normalized to the total number of events predicted for process j ($\int F_j(V)dV = \mathrm{N_j^{pred}}$)
- $G(\beta_2|1, \Delta_2) = \frac{1}{2\pi\Delta_2^2} e^{(\beta_2-1)^2/2\Delta_2^2}$: Gaussian penalty for the background parameter to deviate too much from the independent background prediction

We will assume a test dataset that is 6.2 times larger than what we had available for this thesis, the equivalent of 1000 pb^{-1} of data. In such a dataset, we expect $N_1 = 35$ single

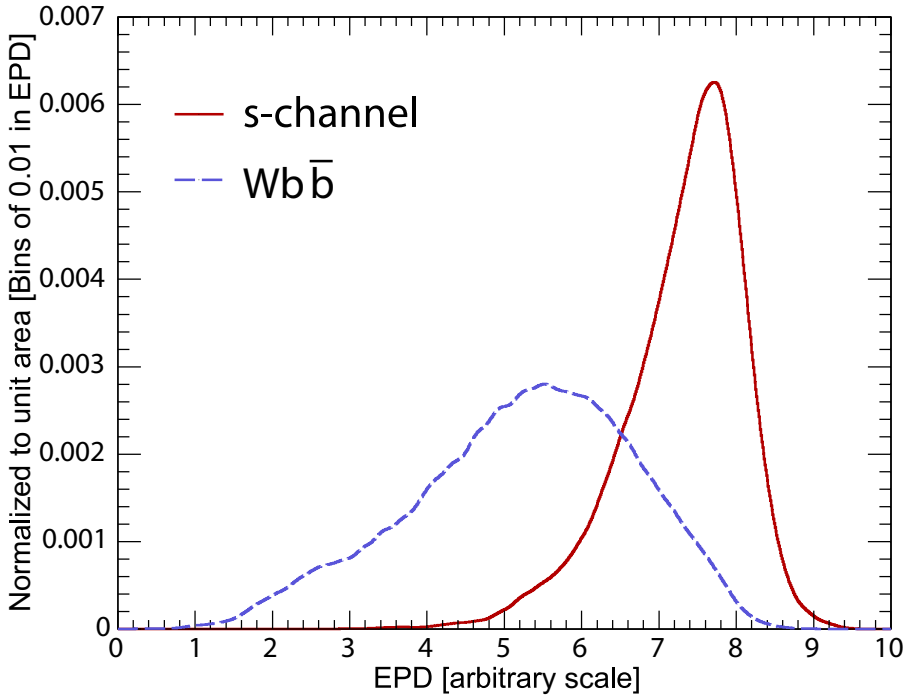

Figure 8.6: Event probability discriminant (EPD) distribution for transfer function smeared s-channel single top and $Wb\bar{b}$ background events. The distributions are normalized to unit area.

top events and $N_2 = 495$ background events to pass the event selection. We do not require the events to pass the $M_{l\nu b}$-window since the event probability is very sensitive to events reconstructed close to the top quark mass. The Breit-Wigner term for the top quark in the matrix element intrinsically de-weights events away from the top quark pole mass. We assume the background normalization to be known to $\Delta_2 = 20\%$. This information is used in the likelihood function in the form of the Gaussian constraint on the background parameter. The pseudo-experiments are performed as described in Section 6.4.1. For each pseudo-experiment, we include pseudo-data in the following forms: (1) measured values of H_T and (2) calculated values of the event probability ratios (EPD). The EPD and H_T distributions of Figure 8.6 and Figure 8.7 are used as templates in the likelihood fit (labeled $F(V)$ in Equation 8.11). All signal is represented by s-channel single top and all background will be represented by the Wbb background. The statistical uncertainty

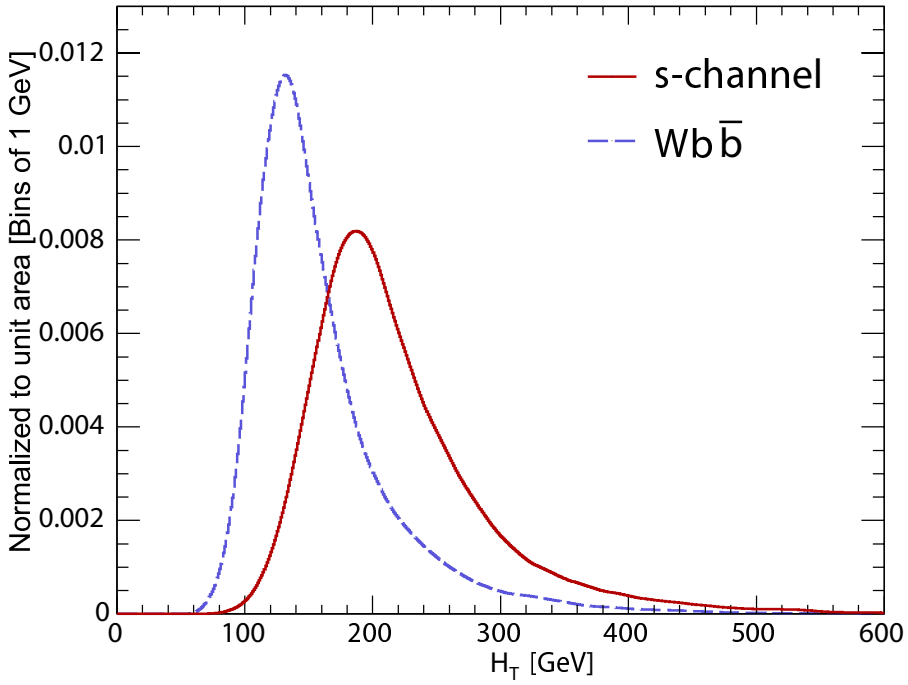

Figure 8.7: H_T distribution for transfer function smeared s-channel single top and $Wb\bar{b}$ background events. The distributions are normalized to unit area.

on the signal parameter, $\beta_1 = \sigma_1/\sigma_{SM}$, will allow us to quantify the improved sensitivity in many pseudo-experiments.

We perform a total of 10,000 pseudo-experiments for different integrated luminosities. Figure 8.8 shows the the statistical uncertainty on β_1 returned by the maximum likelihood fit as a function of the integrated luminosity. The upper contour shows the result for the likelihood fit to the H_T templates and the lower contour shows the result for the likelihood fit to the EPD templates. When using the EPD templates in the maximum likelihood fit, the statistical uncertainty is significantly lower (about a factor of 1.8) compared to the likelihood fit to the H_T templates.

In summary, the statistical uncertainty is reduced by about a factor of 1.8 using the event probability information in the likelihood method compared to the likelihood fit, which includes the H_T information only. Assuming Gaussian statistics, a reduced statistical uncertainty by a factor of 1.8 approximately triples the statistical sensitivity of the

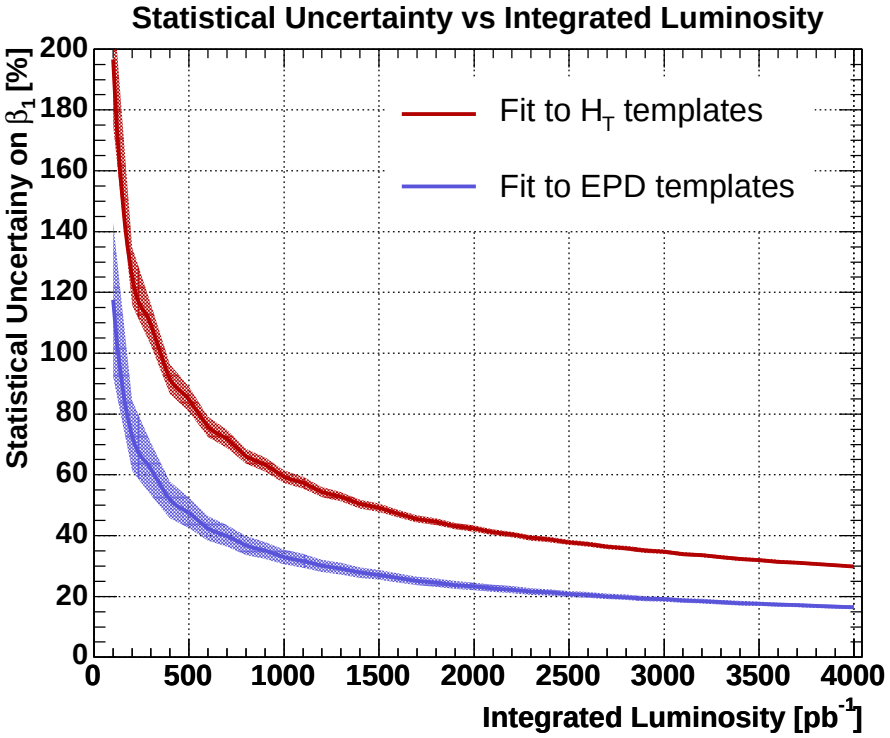

Figure 8.8: Statistical uncertainty on the maximum likelihood parameter $\beta_i = \sigma_1/\sigma_{SM}$, which corresponds to the statistical uncertainty on the single top cross-section as a function of integrated luminosity for likelihood fits to the H_T template distributions (top) and EPD template distributions (bottom).

analysis. This is, of course, an upper bound since no sources of systematic uncertainties were included and the events have not been passed through the full GEANT detector simulation. Instead the jet energies of the events were 'smeared' with the transfer function.

The next steps of the analysis include the derivation of the transfer function for both single top (s-channel and t-channel) and background processes ($Wb\bar{b}$, $Wc\bar{c}$, Wc, $Wq\bar{q}$ and $t\bar{t}$) separately. Then we will perform a study on how fully simulated Monte Carlo events, which are passed through the full GEANT detector simulation, will affect the performance of the event probability. We will compare the predicted event probability distribution with an independent dataset (e.g. un-tagged W+jets data) and estimate

systematic uncertainties. The calculation of the event probability can be performed for all signal and background processes according to Equation 8.10 (only the matrix element has to be changed to represent the desired process) except for $t\bar{t}$. The calculation of the $t\bar{t}$ event probability will require a separate derivation of the event probability since we have to account for two undetected final state particles[2].

[2]A lepton and a neutrino in case of the $t\bar{t}$ dilepton decay mode or two quarks in the case of the $t\bar{t}$ lepton+jets decay mode.

Chapter 9

Conclusions

Since the upgraded Tevatron Collider resumed operation in 2001, both the CDF and DØ Collaborations have collected their first sets of physics data. Over the next few years, the Tevatron at Fermilab will be the only facility where top quarks can be produced and analyzed.

In this thesis, we have performed the first search for electroweak single top quark production in 1.96 TeV proton-antiproton collisions using 162 pb^{-1} of CDF Run II data. We have selected candidate events which show evidence for a leptonic W decay and two energetic jets. We improved our signal to background ratio (S/B) in this sample from 1/200 to about 1/8 by further requiring that candidate events feature at least one b-tagged jet and have a reconstructed mass of the lepton, neutrino and b-jet of 140 $\text{GeV/c}^2 < M_{l\nu b} < 210$ GeV/c^2 close to the top quark mass. From Monte Carlo studies, we predict 1.5±0.2 s-channel single top events, 2.8±0.5 t-channel single top events and 33.8±5.8 background events to pass the event selection. This amounts to a total of 38.1±5.9 predicted events and we observe 42 events in the data.

To quantify the single top content in data, we employ a likelihood fit technique to the H_T distribution in data. The H_T distribution has the advantage that it looks very similar for both single top production channels and different for background processes.

The combination of both channels to one signal improves the sensitivity of the search. The most probable combined single top production cross section is obtained at $\sigma_{single\ top} = 7.7^{+5.1}_{-4.9}$ pb, which indicates that we find no significant evidence for single top quark production in this dataset. We therefore set an upper limit at the 95% confidence level on the combined single top quark production cross section of 17.8 pb, roughly six times the Standard Model prediction ($\sigma_{SM} = 2.9$ pb).

The Standard Model single top quark production cross section is directly proportional to the CKM matrix element $|V_{tb}|$. In this context, we can translate the result obtained for the most probable value (MPV) of the cross section and the 95% C.L. into results on $|V_{tb}|$. The Standard Model predicts a value of $|V_{tb}|$ close to unity ($|V_{tb}^{SM}| = 0.999$), thus:

$$\frac{\sigma_{MPV}}{\sigma_{SM}} = \frac{|V_{tb}|^2}{|V_{tb}^{SM}|^2} = \frac{|V_{tb}|^2}{0.998} \simeq |V_{tb}|^2$$

We obtain $|V_{tb}| = 1.6^{+0.5}_{-0.6}$ and $|V_{tb}| < 2.5$ at 95% C.L. At this point, this result does not strongly constrain $|V_{tb}|$.

To establish a single top signal with a reduced uncertainty on the cross section and $|V_{tb}|$, more data are needed. The Tevatron experiments will continue data taking until the year 2008. The full Run II dataset is expected to be at least 25 times the size we had available for this analysis.

In the meantime, we will work on an improved discrimination of the single top signal against background. This can be achieved by including more information to specify each event. The data for this analysis were of the form of measured values of the kinematic variable H_T for each observed event. The shape of the H_T templates for signal and background used in the likelihood method corresponds to the shape of the differential cross-section $d\sigma/dH_T$. An improved discrimination can be achieved by including the shapes of all differential cross sections in the analysis. This corresponds to calculating the fully differential cross section on an event-by-event basis for the signal hypothesis and the background hypothesis. This new analysis technique was introduced in Chapter 8 and a preliminary study has shown that this approach may triple the statistical sensitivity

of the analysis. We will further pursue this new analysis technique and hopefully find evidence for single top quark production in the next year or two. At that time, the CDF Collaboration is expecting to have accumulated a dataset in excess of 1000 pb^{-1}, with which we hope to measure the single top quark cross-section with a statistical precision of about 30%.

Appendix A

Lepton Identification Variables

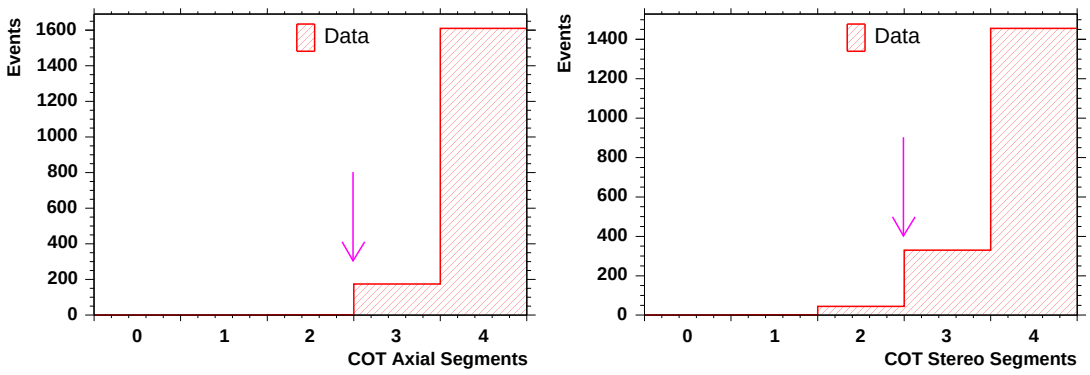

Figure A.1: Distributions of lepton selection requirements on the number of axial and stereo COT super-layers (see Table 4.1 and Table 4.2) from $Z \rightarrow l^+l^-$ candidate events in data. The arrows indicate the location of the selection cut applied on these variables [66].

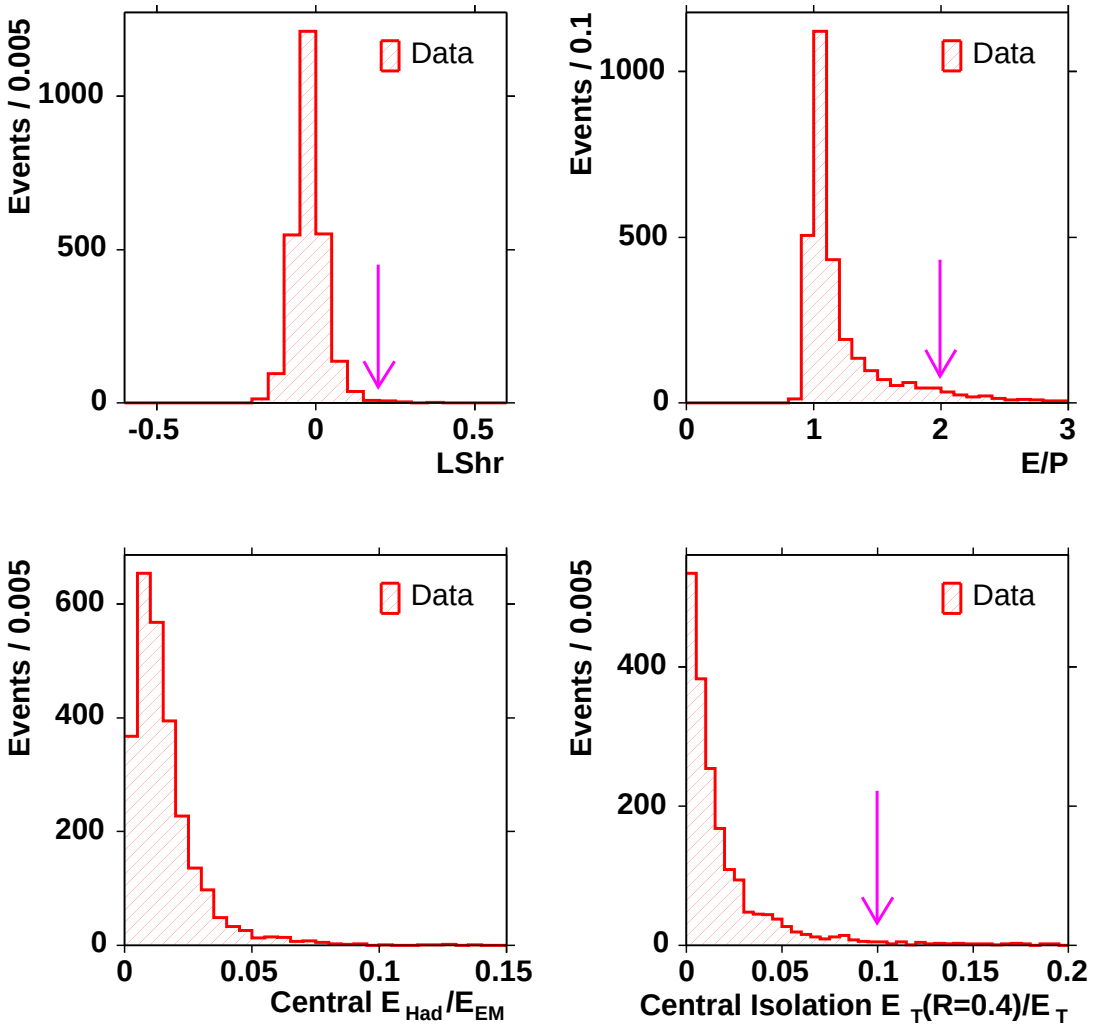

Figure A.2: Distributions of electron selection variables L_{shr}, E/p, E_{had}/E_{em} and $Isolation$ (see Table 4.1) from $Z \rightarrow e^+e^-$ candidate events in data. The arrows indicate the location of the selection cut applied on these variables. No arrow is shown on the E_{had}/E_{em} distribution since the selection requirement on this variable is dependent on the electron energy [66].

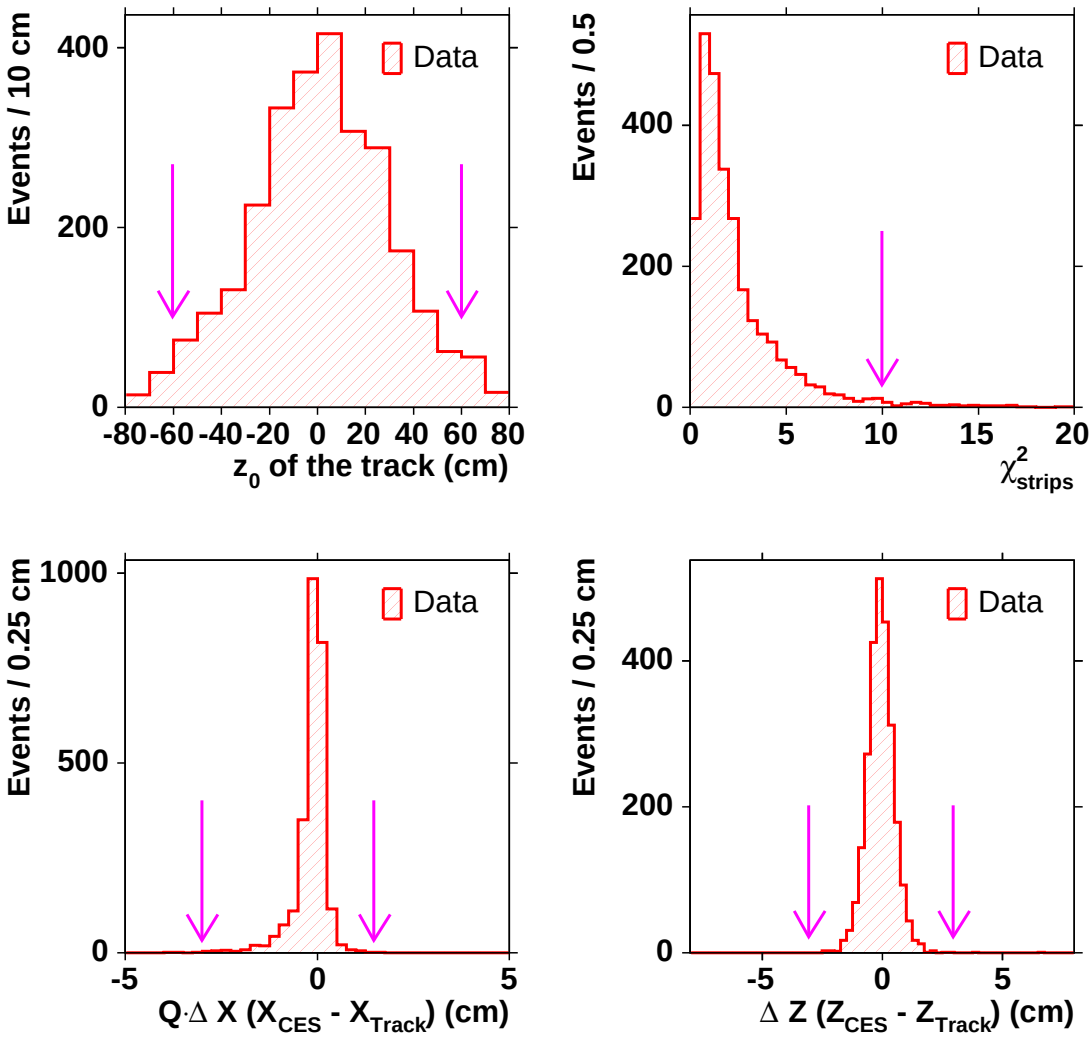

Figure A.3: Distributions of electron selection variables $|\Delta z_0|$, χ^2_{Strip}, $Q\cdot\Delta x$ and $|\Delta z|$ (see Table 4.1) from $Z \rightarrow e^+e^-$ candidate events in data. The arrows indicate the location of the selection cut applied on these variables [66].

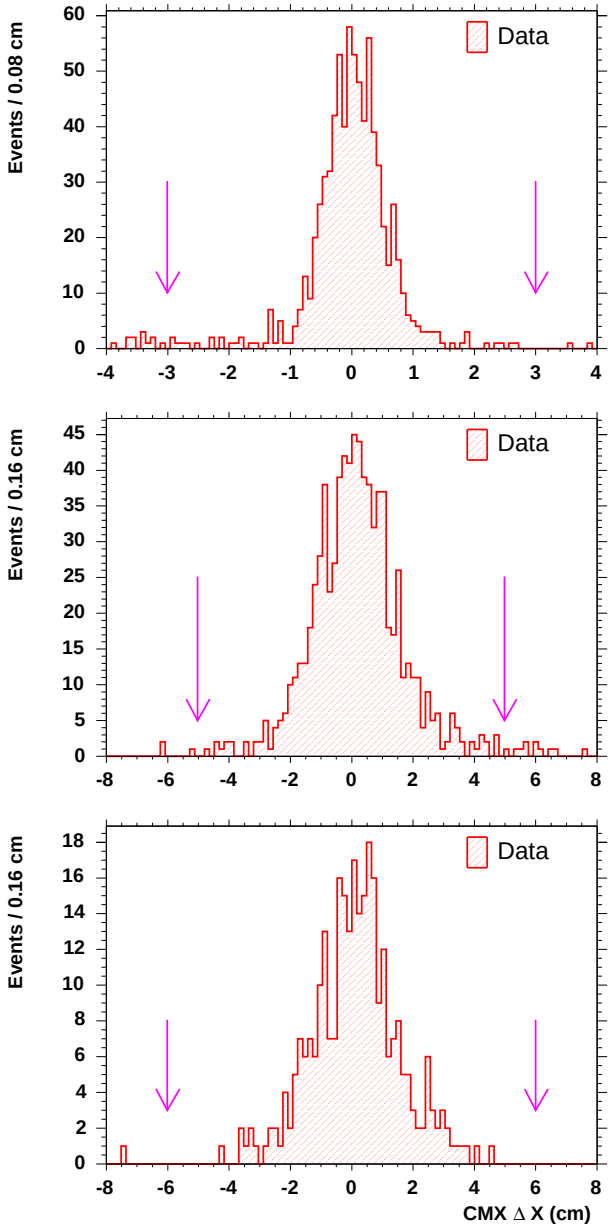

Figure A.4: Distributions of muon selection variables $|\Delta x|_{CMU}$, $|\Delta x|_{CMP}$ and $|\Delta x|_{CMX}$ (see Table 4.2) from $Z \rightarrow \mu^+\mu^-$ candidate events in data. The arrows indicate the location of the selection cut applied on these variables [66].

Appendix B

Shape Uncertainty for Background

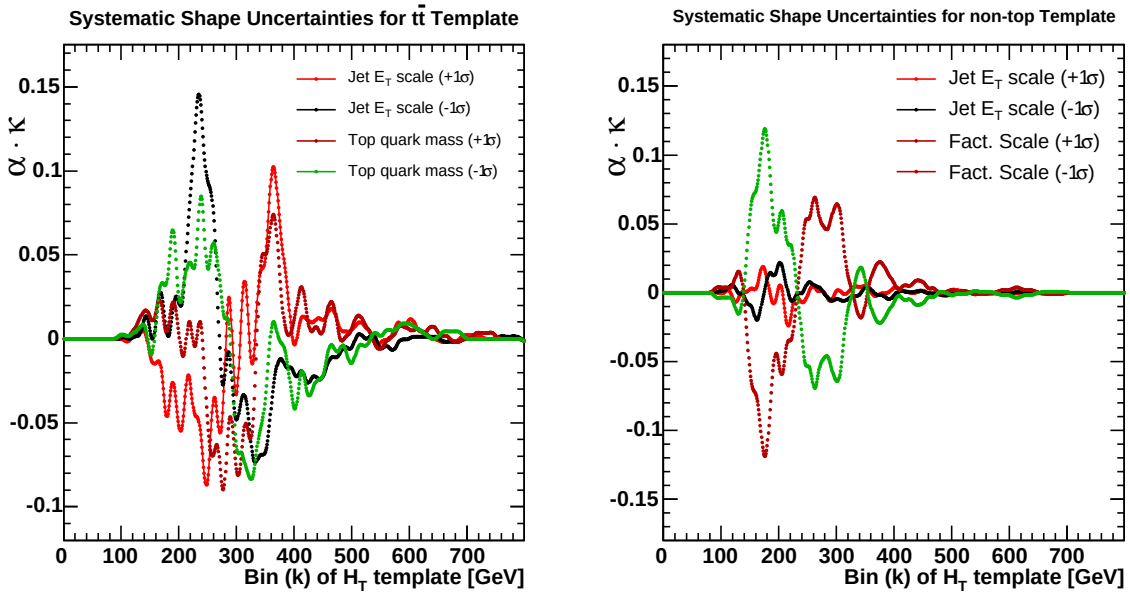

Figure B.1: Absolute shift of the H_T background template histograms ($\alpha \cdot \kappa$) in each bin due to systematic shape uncertainties. The graphs are normalized to the maximum bin content of the default background H_T template. The shape uncertainty due to the jet energy scale and the top quark mass were considered for the $t\bar{t}$ background template (left) and the shape uncertainty due to the jet energy scale and the factorization scale were considered for the non-top background template (right).

Appendix C

Event Yield in Data

Event selection	Events / 162 pb^{-1}
High p_T lepton trigger	915 588
Lepton Identification	415 636
Event Vetoes	268 419
Missing transverse energy $\not\!\!E_T$	165 483
W + 2 jets	2 908
W + 2 jets + btag	78
W + 2 jets + btag + $\text{M}_{l\nu b}$	42

Table C.1: Event yield in data after applying (sequentially) all event selection criteria outlined in Chapter 4.

Appendix D

Calculation of Phase Space for Single Top Events

For s-channel single top events, $qq' \to t\bar{b} \to b\bar{b}l\nu$, the phase space factor can be written as:

$$d\Phi_4(q_1+q_2;p_1,p_2,p_3,p_4) = \delta^4(q_1+q_2-\sum_{i=1}^{4} p_i)\prod_{i=1}^{4}\frac{d^3\vec{p}_i}{(2\pi)^3 2E_i} \tag{D.1}$$

where q_1 and q_2 are the four momenta of the initial quarks; p_1, p_2 are the four momenta of the b and $\bar{b}$ quark, respectively; and p_3, p_4 are the four momenta of the lepton and neutrino, respectively. It is convenient to change variables from momenta $(\vec{p}_1,\vec{p}_2,\vec{p}_3,\vec{p}_4)$ to $(\rho_1,\Omega_1,\rho_2,\Omega_2,\vec{p}_l,\vec{p}_{\nu,T},m_W)$ where $\rho_i = |\vec{p}_i|$ is the absolute momentum of the quarks, Ω_i are the quark solid angles, and m_W is the mass of the W boson. One way to perform the transformation is to use the recursive character of the phase space [6]:

$$\begin{aligned}\prod_{i=1}^{4}\frac{d^3\vec{p}_i}{(2\pi)^3 2E_i} &= \delta(p_W^2-m_W^2)dm_W^2\prod_{i=1}^{4}\frac{d^3\vec{p}_i}{(2\pi)^3 2E_i} \\ &= \frac{dm_W^2}{|\frac{\partial p_W^2}{\partial p_{\nu,z}}|}\frac{d^3\vec{p}_l}{(2\pi)^3 2E_l}\frac{d\vec{p}_{\nu,T}}{(2\pi)^3 2E_\nu}\prod_{i=1}^{2}\frac{\rho_i^2 d\rho_i d\Omega_i}{(2\pi)^3 2E_i}\end{aligned} \tag{D.2}$$

In the last step, the δ-function was integrated with respect to $p_{\nu,z}$ using:

$$\int f(x)\delta[g(x)]dx = \frac{f(a)}{|g'(a)|} \quad , at\ g(a)=0 \tag{D.3}$$

The partial derivative becomes (neglecting neutrino and lepton masses):

$$\begin{aligned}\frac{\partial p_W^2}{\partial p_{\nu,z}} &= \frac{\partial (p_l + p_\nu)^2}{\partial p_{\nu,z}} \\ &= \frac{\partial}{\partial p_{\nu,z}}(m_l^2 + m_\nu^2 + 2E_l E_\nu - 2p_{l,z}p_{\nu,z} - 2\vec{p}_{l,T}\vec{p}_{\nu,T}) \\ &= 2E_l\frac{p_{\nu,z}}{E_\nu} - 2p_{\nu,z} \end{aligned} \tag{D.4}$$

Finally, we substitute Equation D.2 into Equation D.1 and integrate two δ-functions with respect to the transverse momentum of the neutrino $\vec{p}_{\nu,T}$. The remaining two δ-functions are integrated with respect to the initial quark's longitudinal momentum and energy in the event probability. The expression for the phase space for single top events is:

$$\begin{aligned} d\Phi_4 &= \delta(E_{q_1} + E_{q_2} - \sum_{i=1}^{4} E_i)\ \delta(p_{q_1,z} + p_{q_2,z} - \sum_{i=1}^{4} p_{i,z}) \\ &\quad \times \frac{dm_W^2}{|2E_l\frac{p_{\nu,z}}{E_\nu} - 2p_{\nu,z}|}\frac{d^3\vec{p}_l}{(2\pi)^3 2E_l}\frac{1}{(2\pi)^3 2E_\nu}\prod_{i=1}^{2}\frac{\rho_i^2 d\rho_i d\Omega_i}{(2\pi)^3 2E_i} \end{aligned} \tag{D.5}$$

Appendix E

Particle Matching

In this section, the transverse energy/momentum and angular resolution is plotted for the final state particles in the single top search. We 'match' fully reconstructed objects from the detector simulation with the initial Monte Carlo particle. A particle is labeled 'matched' to the reconstructed object when it is identified within a cone of $\Delta R < 0.4$ of the reconstructed object (jet, lepton, MET).

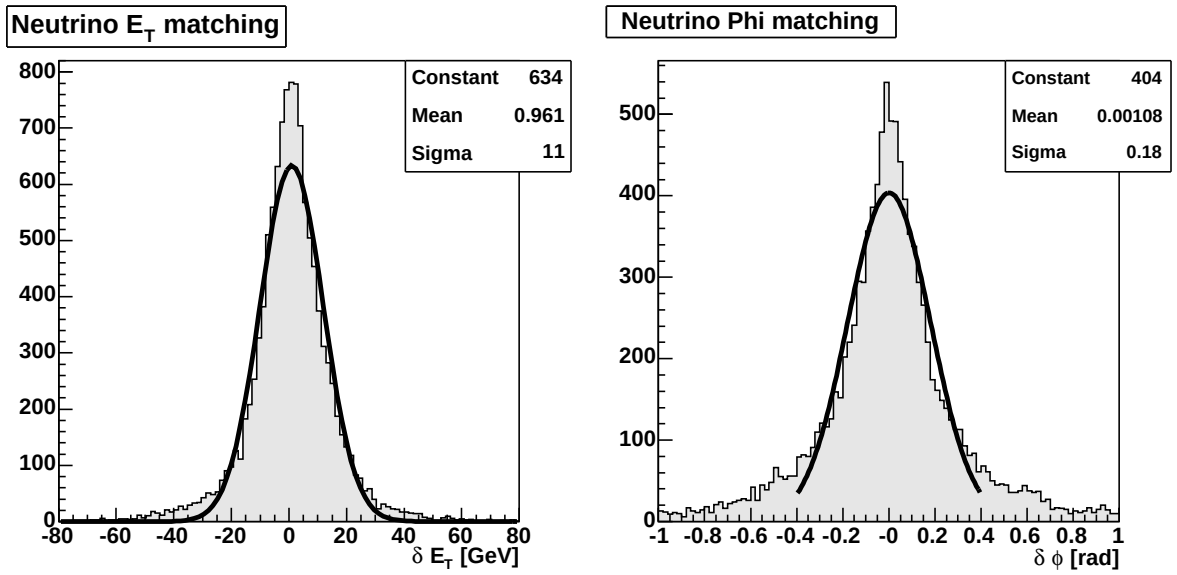

Figure E.1: Transverse energy (left) and angular resolution $\delta\phi$ (right) for the neutrino from fully simulated and reconstructed (s-channel) single top events.

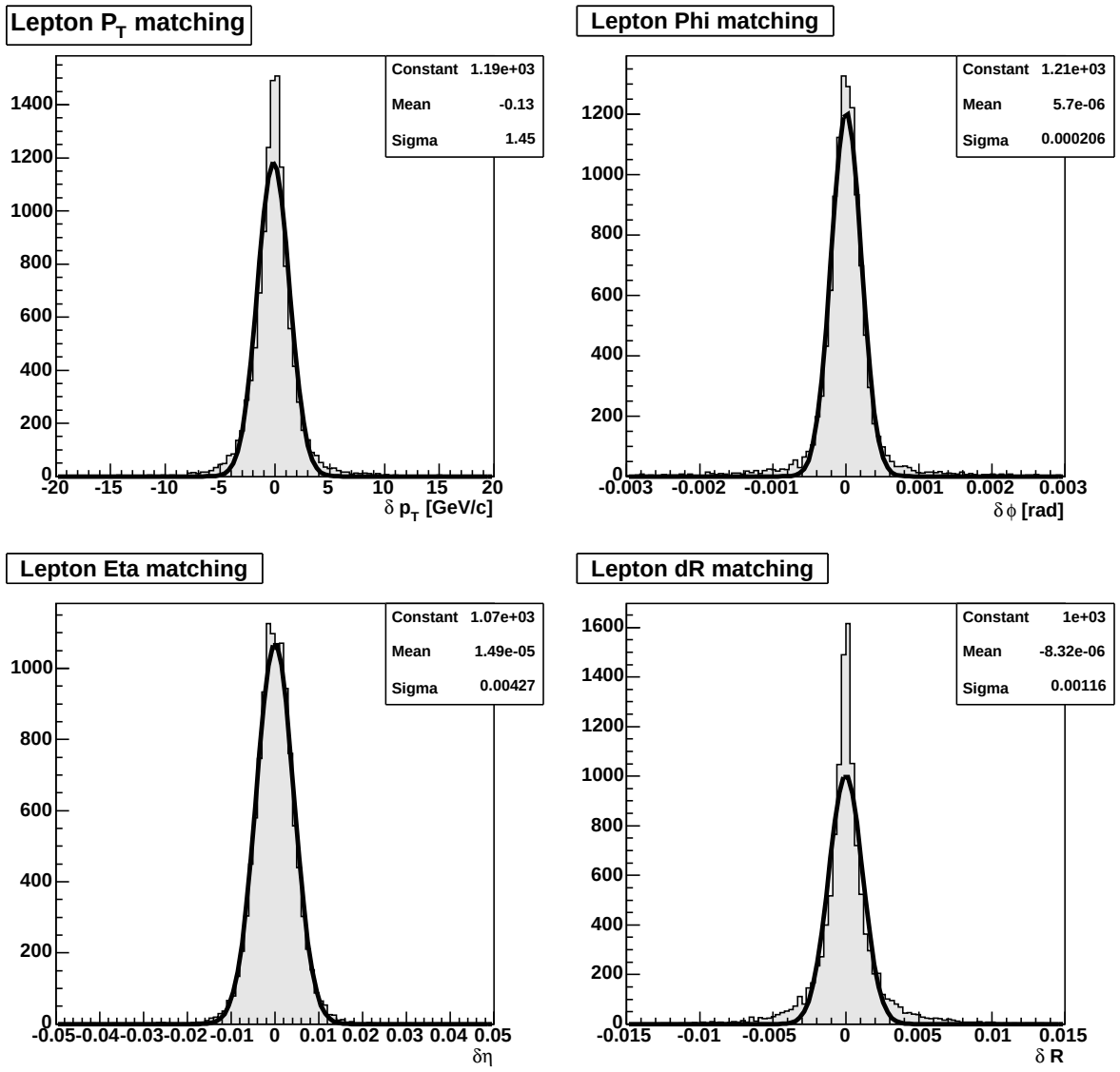

Figure E.2: Transverse momentum (top left) and angular resolution $\delta\phi$ (top right), $\delta\eta$ (bottom left) and $\delta R = \sqrt{\Delta\phi^2 + \Delta\eta^2}$ (bottom right) for the lepton from fully simulated and reconstructed (s-channel) single top events.

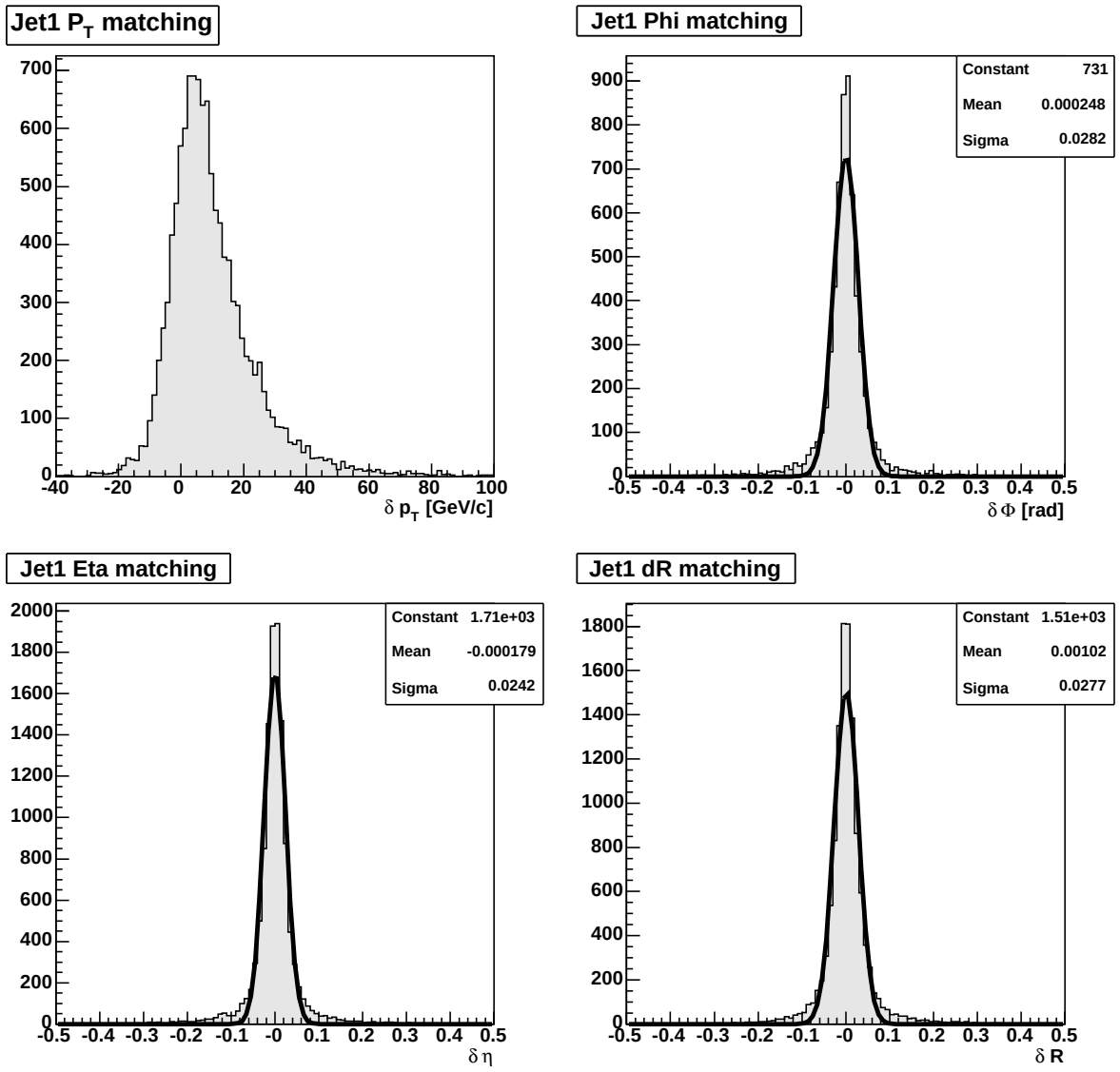

Figure E.3: Transverse momentum (top left) and angular resolution $\delta\phi$ (top right), $\delta\eta$ (bottom left) and $\delta R = \sqrt{\Delta\phi^2 + \Delta\eta^2}$ (bottom right) for the leading jet from fully simulated and reconstructed (s-channel) single top events.

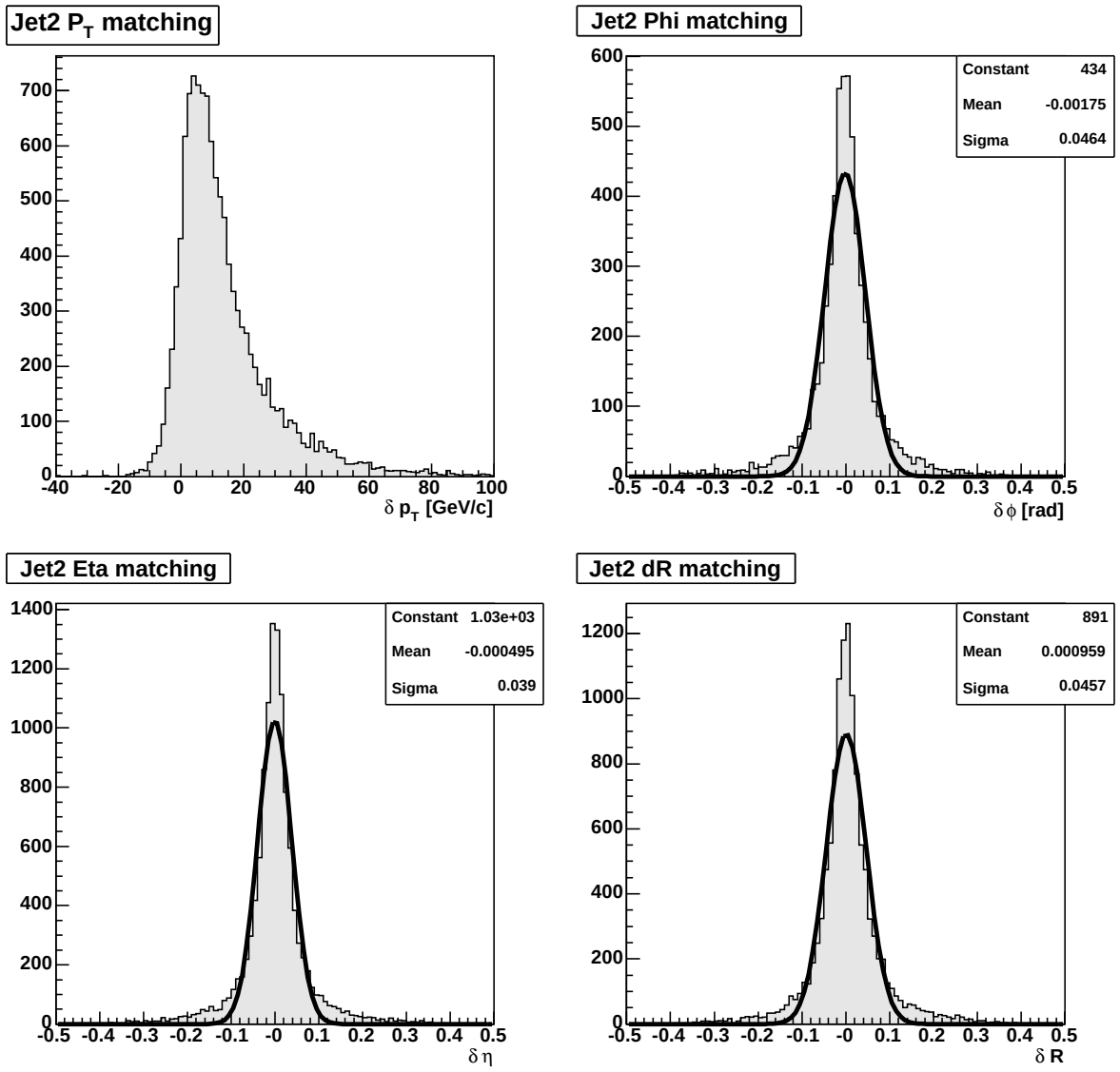

Figure E.4: Transverse momentum (top left) and angular resolution $\delta\phi$ (top right), $\delta\eta$ (bottom left) and $\delta R = \sqrt{\Delta\phi^2 + \Delta\eta^2}$ (bottom right) for the second leading jet from fully simulated and reconstructed (s-channel) single top events.

Bibliography

[1] CDF Collaboration, F. Abe *et al.*, Phys. Rev. Lett. **74**, 2626 (1995)

[2] DØ Collaboration, S. Abachi *et al.*, Phys. Rev. Lett. **74**, 2632 (1995)

[3] G. Altarelli, *Status of the Standard Model and Beyond*, 38th Rencontres de Moriond, hep-ph/030605 (2003)

[4] M. E. Peskin, D. V. Schroeder, *An Introduction to Quantum Field Theory*, Addison-Wesley (1995)

[5] F. Halzen, A. Martin, *Quarks and Leptons*, John Wiley & Sons (1984)

[6] Particle Data Group, *The Review of Particle Physics*, http://pdg.lbl.gov (2004)

[7] The Super-Kamiokande Collaboration, *Evidence for oscillation of atmospheric neutrinos*, Nucl. Rev. Lett. **81**, 1562-1567 (1998)

[8] G. Kane, *Modern Elementary Particle Physics*, Addison-Wesley (1993)

[9] R. P. Feynman, *QED, The Strange Theory of Light and Matter*, Princeton (1985)

[10] S. Weinberg, Phys. Rev. Lett. **19**, 1264 (1967);
J. Goldstone, A. Salam, S. Weinberg, *Broken Symmetries*, Phys. Rev. Lett. **127**, 965-970 (1962);
S. Glashow, Nucl. Phys. **22**, 579 (1961)

[11] P. Higgs, *Broken Symmetries and the Masses of Gauge Bosons*, Phys. Rev. Lett. **13**, 508-509 (1964)

[12] A. Sirlin, *Thirty Years of Precision Electroweak Physics*, J. Phys. **G29**, 213-224 (2003)

[13] R. K. Ellis, W. J. Stirling, B. R. Webber *QCD and Collider Physics*, Monographs on Particle Physics, Nuclear Physics and Cosmology (1996)

[14] D. Gross, F. Wilczek, *Asymptotically Free Gauge Theories*, Phys. Rev. Lett. **30**, 1343 (1973)

[15] I. Bigi *et al.*, *Production and Decay of Ultraheavy Quarks*, Phys. Lett. **B181**, 157 (1986)

[16] S. Willenbrock, *Studying the Top Quark*, Rev. Mod. Phys. **72**, 1141-1148 (2000)

[17] M. R. Whalley *HEPDATA, The Durham HEP Databases*, http://durpdg.dur.ac.uk/hepdata/pdf3.html

[18] H. L. *et al.*, Phys. Rev. D **55**, 1280, hep-ph/9606399 (1997);
H. L. *et al.*, Eur. Phys. J. **C 12**, 375, hep-ph/9903282 (2000)

[19] A. D. Martin, R. G. Roberts, W. J. Stirling and R.S. Thorne, *Parton distributions: a new global analysis*, Eur. Phys. J. C **14**, 133, hep-ph/9803445 (2000)

[20] G. D. Mahlon, *Spin Polarization in Single Top Events*, hep-ph/9811219 (1998)

[21] S. Cortese and R. Petronzio, Phys. Lett. B **253**, 494 (1991); M.C. Smith and S. Willenbrock, Phys. Rev. D **54**, 6696 (1996);
A.P. Heinson, A.S. Belyaev and E.E. Boos, Phys. Rev. D **56**, 3114 (1997);
S. Mrenna and C.-P. Yuan, Phys. Lett. B **416**, 200 (1998)

[22] S. Willenbrock and D.A. Dicus, Phys. Rev. D **34**, 155 (1986);
S. Dawson and S. Willenbrock, Nucl. Phys. B **284**, 449 (1987);
C.-P. Yuan, Phys. Rev. D **41**, 42 (1990);
F. Anselmo, B. van Eijk and G. Bordes, Phys. Rev. D **45**, 2312 (1992);
D. Carlson and C.-P. Yuan, Phys. Lett. B **306**, 386 (1993);
G. Bordes and B. van Eijk, Nucl. Phys. B **435**, 23 (1995);
T. Stelzer, Z. Sullivan and S. Willenbrock, Phys. Rev. D **56**, 5919 (1997);
T. Stelzer, Z. Sullivan and S. Willenbrock, Phys. Rev. D **58**, 094021 (1998);
Q.-H. Cao, C.-P. Yuan, hep-ph/0408180 (2004)

[23] T. Affolder *et al.*, Phys. Rev. Lett. **86** 3233 (2001).

[24] C. Caso *et al.*, Euro. Phys. J. C **3**, 1 (1998).

[25] G.L. Kane, G.A. Ladinsky and C.P. Yuan, Phys. Rev. D **45**, 124 (1992);
D. Carlson, E. Malkawi and C.-P. Yuan, Phys. Lett. B **337**, 145 (1994);
T.G. Rizzo, Phys. Rev. D **53**, 6218 (1996);
E. Malkawi and T. Tait, Phys. Rev. D **54**, 5758 (1996);
M. Hosch, K. Whisnant and B.-L. Young, Phys. Rev. D **56**, 5725 (1997);
T. Tait and C.-P. Yuan, Phys. Rev. D **55**, 7300 (1997);
E. Boos, L. Dudko and T. Ohl, Eur. Phys. J. C **11**, 473 (1999);
T. Tait and C.-P. Yuan, Phys. Rev. D **63**, 014018 (2001);
D. Espriu and J. Manzano, Phys. Rev. D **65**, 073005 (2002);
E.H. Simmons, Phys. Rev. D **55**, 5494 (1997);
P. Baringer, P. Jain, D.W. McKay and L.L. Smith, Phys. Rev. D **56**, 2914 (1997);
C.X. Yue and G.R. Lu, Chin. Phys. Lett. **15**, 631 (1998);
T. Han, M. Hosch, K. Whisnant, B.-L. Young, X. Zhang, Phys. Rev. D **58**, 073008 (1998)

[26] CDF Collaboration, D. Acosta *et al.*, Phys. Rev. D **65**, 091120 (2002)

[27] DØ Collaboration, V. Abazov *et al.*, Phys. Lett. B **517**, 282 (2001);
Phys. Rev. D **63**, 031101 (2000)

[28] B.W. Harris *et. al.*, Phys. Rev. D **66**, 054024 (2002);
Z. Sullivan, *Understanding single-top-quark production and jets at hadron colliders*, hep-ph/0408049 (2004)

[29] T. Stelzer and W.F. Long, Phys. Commun. **81**, 337 (1994);
F. Maltoni, T. Stelzer, hep-ph/0208156,
http://madgraph.hep.uiuc.edu/ (2002)

[30] T. Söstrand *et. al.*, Comp. Phys. Commun. **135**, 238 (2001)

[31] C. Ciobanu, T. Junk, T. Müller, P. Savard, B. Stelzer, W. Wagner, T. Walter, *MadEvent Signal Samples used in the Run II Single Top Search*, CDF Note 7020 (2004)

[32] E. E. Boos, L.V. Dudko, and V.I. Savrin, CMS NOTE 2000/065

[33] Fermi National Accelerator Laboratory, Tevatron Department,
http://www-bdnew.fnal.gov/tevatron/

[34] D. Mohl, G. Petrucci, L. Thorndahl and S. Van Der Meer, *Physics and Technique of Stochastic Cooling*, Phys. Rept. **58**, 73 (1980)

[35] *The CDF II Detector Technical Design Report*, FERMILAB-Pub-96/390E (1996);
http://www-cdf.fnal.gov/

[36] CDF Collaboration, D. Acosta *et. al.*, *The CDF Cherenkov Luminosity Monitor*, Nucl. Instrum. Meth. A **461**, 540-544, (2001)

[37] V. Barger, R. Phillips, *Collider Physics*, Addison-Wesley, New York (1987)

[38] http://hepwww.rl.ac.uk/theory/seymour/herwig/

[39] S. Jadach, *et. al.*, CERN-TH-6793 (1992)

[40] Application Software Group, Computing and Network Division, CERN, http://wwwasd.web.cern.ch/wwwasd/geant/

[41] A. Bhatti, A. Gibson, B. Heinemann, G. Latino, *Central Calorimeter Scale For Jets in CDF Run II*, CDF Note 6930 (2004)

[42] CDF Collaboration, D. Acosta et al., *Measurement of the $t\bar{t}$ Production Cross Section in $p\bar{p}$ collisions at $\sqrt{s} = 1.96$ TeV using Lepton + Jets Events with Secondary Vertex b-tagging*, Phys. Rev. D **71**, 052003 (2004)

[43] C. Ciobanu, T. Junk, T. Müller, P. Savard, B. Stelzer, W. Wagner, T. Walter, *Non-Top Background Estimate for Single Top in 162 pb^{-1}*, CDF Note 7062 (2004)

[44] W.K. Sakumoto and A. Hocker, *Event $|Z_{vtx}| \leq 60$ cm Cut Efficiency for Run II*, CDF Note 6331 (2004)

[45] D. Amidei et al., *Measurement of the $p\bar{p} \to t\bar{t}$ cross section in the ℓ+jets SECVTX tagged sample*, CDF Note 6329 (2004)

[46] Y.-K. Kim, J. Nielsen, L. Tompkins, G. Veramendi, *Trigger Efficiencies for High P_T Electrons*, CDF Note 6234, Version 3.1 (2004)

[47] M. Coca, E. Halkiadakis, S. Lockwitz, *Central Electron Identification Efficiencies for the 200 pb^{-1} Run II Dataset*, CDF Note 6580 (2004)

[48] V. Martin and L. Cerrito, *Muon Cuts and Efficiencies for 4.11 Analyses*, CDF Note 6825 (2004).

[49] R. Bonciani, S. Catani, M. L. Mangano and P. Nason, Nucl. Phys. B **529** 87-102 (1998);

M. Cacciari, S. Frixione, M. L. Mangano, P. Nason and G. Ridolfi, hep-ph/0303085 (2003)

[50] J.M. Campbell and R.K. Ellis, *Update on vector boson pair production at hadron colliders*, Phys. Rev. D **60**, 113006 (1999)

[51] F. Caravaglios *et. al.*, Nucl. Phys. B **539**, 215 (1999); M. L. Mangano *et. al.*, Nucl. Phys. B **632**, 343 (2002); M. L. Mangano *et. al.*, JHEP 0307:001 (2003);

[52] S. K. Wolinski, *Search for Single-Top-Quark Production in $p\bar{p}$ Collisions at $\sqrt{s}$ 1.8 TeV*, Ph.D thesis, The University of Michigan (2002)

[53] F. James, *MINUIT, Function Minimization and Error Analysis Reference Manual*, CERN Program Library Long Writeup, D506 (1994)

[54] L. Demortier, *Bayesian treatments of Systematic Uncertainties*, Proceedings of Advanced Statistical Techniques in Particle Physics, Grey College, Durham, 18 - 22 March 2002,
http://www.ippp.dur.ac.uk/Workshops/02/statistics/proceedings.shtml

[55] C. Ciobanu, T. Junk, T. Müller, P. Savard, B. Stelzer, W. Wagner, T. Walter, *Likelihood Function for Single Top Search with 162 pb^{-1}*, CDF Note 7106 (2004)

[56] Y.-K. Kim, U.-K. Yang, *Initial state gluon radiation studies on Drell-Yan data for top-pair production in hadron collider*, CDF Note 6804 (2003)

[57] S. R. Slabospitsky and L. Sonnenschein, Comput. Phys. Commun. **148** 87-102, hep-ph/0201292 (2002)

[58] CDF Collaboration, D. Acosta *et al.*, *Search for electroweak single-top-quark production in $p\bar{p}$ collisions at $\sqrt{s}$=1.96 TeV*, Phys. Rev. D **71**, 012005 (2005)

[59] CDF Collaboration, D. Acosta *et al.*, *Search for a W' Boson Decaying to a Top and Bottom Quark Pair in 1.8 TeV $p\bar{p}$ Collisions*, accepted by Phys. Rev. Lett., hep-ex/0209030 (2002)

[60] V. M. Abazov *et al.*, *A precision measurement of the mass of the top quark*, Nature **429**, 638 - 642 (2004)

[61] R. H. Dalitz and G. R. Goldstein, *Test of analysis method for top-antitop production and decay events*, Proc. R. Soc. Lond. A **445**, 2803-2834 (1999)

[62] K. Kondo *et al.*, *Dynamical likelihood method for reconstruction of events with missing momentum. 3: Analysis of a CDF high p_T $e\mu$ event as $t\bar{t}$ production*, J. Phys. Soc. Jpn **62**, 1177-1182 (1993)

[63] M.F. Canelli, *Helicity of the W Boson in Single-Lepton $t\bar{t}$ events*, Ph.D thesis, The University of Rochester (2003)

[64] E. Murayama, I. Watanabe and K. Hagiwara, *HELAS: HELicity Amplitude Subroutines for Feynman Diagram Evaluations*, KEK Report 91-11 (1992)

[65] T. Stelzer and W. F. Long, *HELLAS: Automatic Generation of Tree Level Helicity Amplitudes*, Phys. Commun. **81**, 357-371 (1994)

[66] CDF Collaboration, D. Acosta *et al.*, *First Measurements of Inclusive W and Z Cross Sections from Run II of the Tevatron Collider*, submitted to Phys. Rev. D. (2005)